Die approbierte Originalversion dieser Dissertation ist an der Hauptbibliothek der Technischen Universität Wien aufgestellt (http://www.ub.tuwien.ac.at).

The approved original version of this thesis is available at the main library of the Vienna University of Technology (http://www.ub.tuwien.ac.at/englweb/).

TECHNISCHE UNIVERSITÄT WIEN

VIENNA UNIVERSITY OF TECHNOLOGY

Dissertation

"Charge-exchange processes in collisions of slow ions with atoms and molecules"

ausgeführt zum Zwecke der Erlangung des akademischen Grades eines Doktors der Naturwissenschaften unter der Leitung von

ao. Univ-Prof. Dr. Friedrich Aumayr

E134

Institut für Allgemeine Physik

eingereicht an der Technischen Universität Wien

Fakultät für Physik

von

Sylvicley Figueira da Silva, MSc.

Matrikelnummer 0327610

Sandwirtgasse 21/16

1060 Wien

Wien, im März 2007

Abstract

Impact of slow multiply charged ions (MCI) on atoms, molecules and surfaces is of considerable interest in various fields of modern research as, e.g., thermonuclear fusion plasmas, astrophysical and ionospheric processes, and surface analytics and nanotechnology. To improve the understanding and permit the control of magnetically confined fusion plasmas, it is necessary to learn more about the relevance of multicharged impurity ions residing in these plasmas.

In the present work, a compact experimental setup has been constructed and utilized for measuring absolute cross sections for single (SEC) and double electron capture (DEC) in collisions of slow singly and multiply charged ions with gaseous atoms and molecules. Our technique combines collection of slow product ions with primary ion beam attenuation and stopping in a differentially pumped target gas chamber, where the pressure is measured by an absolutely calibrated capacitance manometer. The primary ions are obtained from a 14.5 GHz all-permanent magnet electron cyclotron resonance (ECR) ion source with extraction geometry optimized for low ion beam energy.

Reliability of the new experimental setup has been checked by proof-of-principle measurements in comparison with well established resonant SEC cross section for impact of slow singly charged noble gas ions on their atoms (He, Ne, Ar).

SEC and DEC cross sections have been investigated for impact of slow doubly charged ions on their own atoms (He, Ne, Ar), where resonant DEC is clearly the dominant reaction. Moreover, SEC and DEC for He^{2+} collisions with Ne have been studied, where at low impact energy SEC is expected to proceed via a single channel only. Additionally, collisions of He^{2+} with simple diatomic molecules (O_2, H_2 and D_2) have been carried out, for which again SEC and DEC have been measured. A theoretical analysis based on Landau-Zener (LZ) theory and the extended over barrier model (EOBM) showed good agreement with results from this work, thereby providing additional insight in the physics behind these processes.

The present experimental and theoretical results are compared to values available in the literature and the results are discussed.

Kurzfassung

Die Interaktion von mehrfach geladenen Ionen mit Atomen, Molekülen und Oberflächen ist von immenser Bedeutung in vielen Bereichen moderner, physikalischer Forschung, wie zum Beispiel bei der Untersuchung von Fusionsplasmen, in astrophysikalischen und ionosphärischen Prozessen, aber auch in der Oberflächenanalyse und allgemein in der Nanotechnologie. Um ein grundlegendes Verständnis und folglich die Kontrolle von Fusionsplasmen unter magnetischem Einschluss zu gewährleisten, ist eine profunde Untersuchung des Einflusses von hoch geladenen Fremdionen in ebendiesen Plasmen von unbedingter Notwendigkeit.

In der hier vorliegenden Arbeit wird ein kompakter experimenteller Aufbau vorgestellt, der die Messung von absoluten Wirkungsquerschnitten für ein- (SEC) und zwei-Elektroneneinfang (DEC) bei Stoßen von langsamen, ein- oder zweifach geladenen Ionen mit Gasatomen und –molekülen ermöglicht. Unsere Methode vereint dabei die Messung langsamer Produkt-ionen mit der Messung der Primärstrahlabschwächung und der selektiven Messung umgeladenen Projektil-ionem in einer differentiell gepumpten Reaktionskammer, in der der Druck mit Hilfe eines absolut geeichten Kapazitäts-Manometers gemessen und konstant gehalten wird. Die Primärionen werden in einer 14.5 GHz Permanentmagnet Elektronen–Zyklotron–Resonanz–Ionenquelle (EZR) produziert, deren Extraktionssystem für geringe Ionenstrahlenergien optimiert ist.

Die Anwendbarkeit und Verlässlichkeit der vorgestellten Methode wurde durch Vergleichsmessungen mit bereits wohl untersuchten SEC Wirkungsquerschnitten für die Wechselwirkung langsamer einfach geladener Edelgas–Ionen (He, Ne, Ar) mit ihren jeweiligen Atomen überprüft und demonstriert.

SEC und DEC Wirkungsquerschnitte für Stöße langsamer zweifach geladener Ionen mit Edelgasen des gleichen Elements (He, Ne, Ar) wurden vermessen. In diesen Stoßsystemen ist DEC der klar dominierende Prozess. Weiters wurden der Wirkungsquerschnitt für SEC und der DEC bei der Interaktion von He^{2+} Ionen mit Neon untersucht, da hierbei erwartet werden kann, dass bei geringen Stoßtenergien der SEC-Ladungsaustausch in nur einem einzigen Kanal erfolgt. Zusätzlich wurden SEC und DEC Messungen für Stöße von He^{2+} mit zweiatomigen Molekülen (O_2, H_2 und D_2) durchgeführt. Eine theoretische Analyse basierend auf der Landau-Zener-Methode (LZ) sowie auf einem erweiterten „Over - Barrier“ Modell (EOBM) erbrachte eine weitgehend zufriedenstellende Übereinstimmung mit den experimentelle Ergebnissen und dadurch eine tiefere Einsicht in die vorliegenden Prozesse.

Sofern vorhanden wurden die erhaltenen experimentellen und theoretischen Werte mit bereits existierenden Daten aus der Literatur verglichen. Die Messergebnisse selbst, sowie die Ergebnisse des Vergleichs werden in der vorliegenden Arbeit diskutiert.

Contents

1. Introduction 6

1.1. Collisions of multiply charged ions with atoms and molecules 6
1.2. Single- and double electron capture processes 7
1.3. The role of charge exchange processes in fusion- and astrophysical plasmas 8
1.4. Aim and outline of this work 10
1.5. Publications 11

2. Theoretical aspects 12

2.1. Introduction 12
2.2. The Schrödinger Equation 13
2.3. The Born-Oppenheimer approximation 13
2.3.1. The Non-Crossing Rule 16
2.4. Landau-Zener theory 18
2.5. Classical over-barrier model (OBM) 21
2.5.2. The extended Over-barrier model (EOBM) 23

3. Experimental setup 28

3.1. Introduction 28
3.2. Ion source and beam transport 28
3.3. Studies on Atomic and Molecular collisions by Beam Attenuation (SAMBA) 31
3.3.1. Electrostatic lenses 31
3.3.2. Collision chamber 34
3.3.3. Vacuum system, gas injection and pressure measurement 37
3.3.4. Electrical connections 39
3.3.5. Data acquisition 40

4. Experimental Procedure 47

4.1. Definition of the primary ion beam impact energy 47
4.2. Determination of the target thickness 48
4.3. Determination of cross sections 49
4.3.1. Attenuation method 49
4.3.2. Retarding field measurements (Beam stopping mode) 51
4.3.3. Collection of slow particles 52
4.3.3.1. Measurement of slow ions 52
4.3.3.2. Measurement of slow electrons 54
4.4. Data acquisition and cross section evaluation 58

5. Results and Discussion 60

5.1. Experimental error sources 60
5.2. Resonant single electron capture 60
5.2.1. Discussion of resonant charge-transfer 63
5.3. SEC and DEC for symmetric systems 65
5.3.1. Ar^{2+} on Ar 66
5.3.2. Ne^{2+} on Ne 70
5.3.3. He^{2+} on He 73
5.4. Charge-exchange in He^{2+} – Ne collisions 76
5.5. Electron capture for doubly charged ions colliding with molecules 80
5.5.1. He^{2+} - O_2 collisions 81
5.5.2. He^{2+} – H_2 and He^{2+} – D_2 collisions 83

6. Conclusion and outlook 89

7. List of acronyms 92

8. Appendix 93

A. Technical drawings 93
B. Geometry file (SIMION) 97
C. Generated potential array (SIMION) 102

9. Acknowledgments 103

10. Bibliography 104

1. Introduction

1.1. Collisions of multiply charged ions with atoms and molecules

In future burning deuterium-tritium (D-T) fusion plasmas the resulting He ash will be the most important impurity species. Accurate knowledge of cross sections for charge-transfer collisions involving doubly ionized helium (He^{2+}, i.e., α particles), and molecules present in the colder outer region of the plasma is of critical importance for plasma modelling as well as for helium ash removal from the divertor region of fusion devices [1]. Helium is also the second most abundant element in the universe and part of the solar wind. Interactions of He^{2+} with molecules like H_2, O_2 and CO have recently gained a lot of interest due to the observation of soft x-ray emission from comets which have been interpreted as being due to charge exchange between multiply charged ions of the solar wind and cometary atmosphere [2, 3]. Moreover, such processes are of relevance for many applied fields including ion implantation, thin film manufacturing and biological studies.

The possibility to produce multi-charged ions has led to a significant improvement in the understanding of processes occurring in ion-atom collisions. Electron transfer processes are especially important in collisions between multi-charged ions and neutral atoms or molecules. After more than twenty years of dedicated research, one-electron charge transfer from neutral atoms or molecules to multi-charged ions is quite well understood. In contrast to this, the knowledge of processes in which more electrons are involved is still limited, although it is realized that multiple electron capture processes are important channels in highly charged ion collisions [4].

1.2. Single- and double electron capture processes

In collisions between ions and atoms or molecules several processes like target ionization, target excitation or charge exchange can take place depending on the impact energy. The charge-exchange (or electron-capture) process involves the transfer of charge (*i.e.* one or more electrons) from an atom or molecule to an atomic or ionic projectile during an inelastic collision. From a theoretical point of view, collisions are classified according to their relative velocity v [5]. It is convenient to distinguish three different regimes, *i.e.* the high velocity region ($v >> v_0$), the intermediate velocity region ($v \approx v_0$) and the low velocity region ($v << v_0$), where v_0 is the "classical" orbiting velocity of the electron to be captured in the target atom or molecule (*e.g.* in the case of atomic hydrogen $v_0 = 2.18 \cdot 10^6$ m/s).

At low and intermediate collision energies electron capture is the dominant process in ion – atom/molecule collisions, much more likely than direct ionization [6-8]. Electron capture can be described by the following equation:

$$\begin{aligned} A^{q+} + B &\rightarrow (AB)^{q+} \\ &\rightarrow A^{(q-s)+}(nl) + B^{s+} + \Delta E \\ &\rightarrow A^{(q-s)+}(n'l') + B^{s+} + \Delta E + hv, \end{aligned} \tag{1.1}$$

here, A^{q+} denotes the projectile ion, B the target atom or molecule, ΔE the inelastic reaction energy defect and hv represents an emitted photon. When the (multiply charged) projectile ion A^{q+} approaches the target B, first a transient quasi-molecular ion is formed $(AB)^{q+}$. During the interaction a certain number s (s = 1,2,…) of electrons can be transferred to the projectile, the occurrence of this process is known as *charge exchange* or *electron transfer*. In the case of single electron capture (s = 1, "SEC") only one electron is transferred; s = 2 denotes double electron capture ("DEC") and s > 2 denotes multiple electron transfer. Usually, the projectile ion, and sometimes the electron deficient target B^{s+} too, end up in an excited state. The excited state subsequently decays via photon emission. The lifetimes of the excited states are typically in the order of nanoseconds, which is longer than the collision times (few *fs*). The de-excitation therefore occurs long after the target and the projectile have separated again. It is an essential characteristic of low energy collisions that the captured electrons can only be found in states around a certain binding energy, very often highly above the ground state. As the highly excited states are deexited, characteristic photons are emitted as line radiation, leaving behind a "fingerprint" of the inelastic collision [9].

1.3. The role of charge exchange processes in fusion- and astrophysical plasmas

Nuclear fusion is the process by which two light nuclei join together to form a heavier nucleus, and it is usually accompanied by the release of a large amount of energy. Due to the Coulombic repulsion of the positively charged nuclei, it takes considerable high energy to force nuclei to fuse, even those of the least massive element, hydrogen. However the fusion of lighter nuclei, which create a heavier nucleus and also free neutrons, will generally release more energy than the necessary to overcome the Coulomb barrier — an exothermic process that can produce self-sustaining reactions.

Because the binding energy that holds a nucleus together is far greater than the energy that holds electrons to a nucleus, the energy released in most nuclear reactions is much larger than that for chemical reactions. For example, energy gained by the combination of an electron with a proton (forming a neutral hydrogen atom) is 13.6 electron volts -- less than one-millionth of the 17 MeV released in fusion of the two hydrogen isotopes, deuterium and tritium, a reaction shown in Figure 1.1. This reaction is considered the most promising one for producing fusion power [10]. As a consequence it generates a helium nucleus (α particles) and a neutron as end products.

The technological development of fusion as a possible power source is, however, a task of extreme complexity and difficulty. The research has developed mainly along two different confinement principles, those of magnetic and inertial plasma confinement.

One point of particular concern is the edge region of magnetically confined fusion plasmas, *i.e.* the region where the hot plasma particles strike the wall. There, the helium ash produced by the fusion events needs to be exhausted, and the power load must be limited preventing the wall to melt and contaminating the plasma. The high temperatures needed for fusion imply the presence of multiply charged ions of impurity species in the plasma. Photon emission after electron capture can give information on the constituents of the plasma, *i.e.* it can be used as a diagnostics tool, either in a passive or active way [10-19]. This allows one to obtain for instance edge-plasma density profiles, impurity concentrations and temperature profiles if the relevant charge exchange cross sections are known. An important issue is the monitoring of the fusion born α particles and measuring or modelling their slowing-down, transport and charge state distribution. These tasks also require accurate knowledge of electron capture cross sections involving α particles [1, 20].

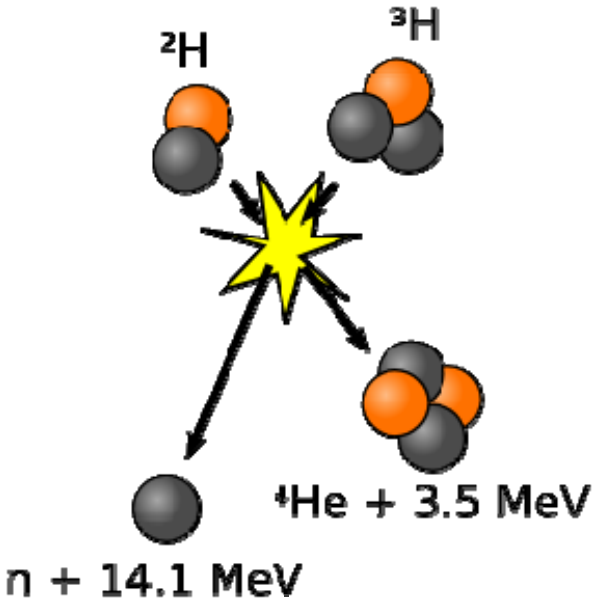

Figure 1.1 – The deuterium-tritium (D-T) fusion reaction. A neutron with 14.1 MeV and a helium nucleus with 3.5 MeV energy are shown as end products [21].

Electron capture processes are not only important in man-made plasmas but also are significantly present in astrophysical plasmas. Recently [2, 3], a large effort has been dedicated to understand the interaction between highly charged ionic constituents of the solar wind and atomic or molecular particles of cometary atmospheres, leading to the emission of soft X-ray. Soon after the first surprising observation of this X-ray emission from comets [22], it was realized that it is caused by electron transfer reactions between highly charged solar wind ions and neutrals cometary gas molecules [23]. The X-ray line emission can thus be linked to properties of both, the solar wind and the comet, e. g. solar wind velocity and cometary atmosphere constituents [24, 25].

Electron capture and ionization processes are also found in (heavy particle) radiation damage of human tissue. Within the track of the primary radiation, secondary particles such as slow electrons and ions are formed. It is the interaction of these secondaries with biologically relevant structures such as DNA, which may cause major biological damage [26-31]. Multiply charged ions as primary particles and their interaction with molecules are therefore of importance in radiotherapy or radiation exposure of astronauts.

1.4. Aim and outline of this work

This thesis is focussed on experimental studies of single and double electron capture processes between slow ions and simple atoms or molecules. Special emphasis is given to fusion relevant alpha particles collisions with atom and molecules present in the edge fusion plasmas.

To this purpose a novel experimental technique has been developed. The experimental results described in this thesis are obtained by a combination of three experimental techniques. The first one is ion beam attenuation, which may be regarded as the established technique for total charge exchange cross section measurement. The second technique, collects the slow particle (*i.e.* the ions and electrons) produced during the collision. In contrast to recoil-ion momentum spectroscopy (RIMS) [32], however, only the total charge of the recoiling target ions is measured. The third technique, applied for doubly charged ions projectiles, relies on a precise measurement of single electron capture events only. As a result absolute cross sections for single and double electron capture, respectively, as well as electron production are determined simultaneously.

In this thesis an extensive study of SEC and DEC processes in collisions of ions with atoms and molecules is presented. The investigated collision energies range from a few eV/amu up to 2 keV/amu and therefore cover the pure electron capture regime well into the transition to ionization dominated interactions. The experimental data are presented in comparison to results of state-of-the-art theoretical calculations as well as more simple theoretical models.

The present thesis is organized in the following way. In chapter 2 a short survey on various theoretical models, including Landau-Zener and the classical over-barrier model, is given. The experimental setup is described in chapter 3. Chapter 4 contains a detailed explanation of the experimental procedures used to determine the cross sections. Results are presented and discussed in chapter 5. Finally, general conclusions and an outlook are given in chapter 6.

1.5. Publications

Parts of this PhD thesis have already been published or are currently submitted for publication. The publications produced in the course of this thesis are listed below:

1 – S. Figueira da Silva, G. Kowarik, F. Aumayr, and HP. Winter
Single and double electron capture by slow He^{2+} from atoms and molecules
J. Phys. Conf. Ser. (2007), in press.

2 – S. Figueira da Silva, HP. Winter and F. Aumayr
Single and double electron capture cross sections for slow He^{2+} impact on O_2 , H_2 and D_2
Accepted for publication in Physical Review A.

3 – S. Figueira da Silva, A. Golczewski and F. Aumayr
Single and double electron capture in symmetric rare gas ion-atom collisions
In preparation for publication in Journal of Physics B.

4 – N. Schupfer, D. D. Tskhakaya sr, R. Khanal, S. Kuhn, F. Aumayr, S. Figueira da Silva and HP Winter
Effect of particles-induced electron emission (PIEE) on the plasma sheath voltage
Plasma Physics and Controlled Fusion, **48** 1093 (2006).

2. Theoretical aspects

2.1. Introduction

In charge exchange processes at least 3 bodies are involved, therefore an analytic solution for the quantum mechanical problem describing the processes usually cannot be found. In the most sophisticated theoretical approaches numeric method are used. In order to reduce the computational time, the motion of the nuclei is usually described classically, only the electrons are treated quantum mechanically. The performance of the different models is largely dependent on the choice of the level in which the electronic wave functions are computed. On the other hand, although mixed quantum-classical approaches are usually less accurate than the full quantum approach, they are very good at describing the overall features of the charge exchange processes with less computational effort.

In this chapter we will present a short review of basic quantum theory approach to the subject[1], followed by the Born-Oppenheimer approximation, which leads to the non-crossing rules for adiabatic potential curves. The Landau-Zener theory is then described in order to calculated transition probabilities between two adiabatic curves. Since the applicability of the Landau-Zener theory is limited (e.g. only exothermic channels can be considered, for doubly charged projectile ions only single electron capture can be calculated), we briefly introduce the (extended) over-the-barrier model, which is based on an intuitive classical picture including some quantum mechanical features. For simplicity, atomic units are used in this chapter unless otherwise stated.

[1] For a more complete review of quantum chemistry and molecular theory, refer to the many excellent works available on the subject [33-35].

2.2. The Schrödinger Equation

A full quantum-mechanical non-relativistic treatment of collisions between ionic and atomic particles leading to charge transfer and ionization processes, relies on solving the time-dependent Schrödinger equation for a given initial state [36]:

$$i\frac{\partial\Psi(t)}{\partial t} = H\Psi(t), \qquad \Psi(t_0) = \Psi_0 \tag{2.1}$$

where the Hamiltonian $H = T + V$ takes into account the kinetic (T) and potential energies (V) of all particles. The probability of finding the system after the collision in a state *f,* represented by the wave function $\psi_f(t)$, can be determined from the projection of the total wave function $\Psi(t)$ onto this state, i.e.

$$c_f = \lim_{t\to\infty}\left\langle \psi_f(t)\middle|\Psi(t)\right\rangle, \tag{2.2}$$

for time t long after the collision at which the particles do not interact anymore. The probability is then given by $|c_f|^2$. However, such an *ab initio* approach is complicated, even for the most simple one-electron systems, therefore the use of approximation methods are usually applied.

2.3. The Born-Oppenheimer approximation

If we consider an N-electron diatomic system with nuclei of masses M_A and M_B, nuclear separation $\vec{R}$ and a set of electronic coordinates $\vec{r} = \{\vec{r}_i\}_N$, the Hamiltonian operator is [34]:

$$\hat{H} = \hat{T}_n + \hat{T}_e + \hat{V}(r,R), \tag{2.3}$$

here

$$\hat{T}_n = -\frac{1}{2}\left[\frac{1}{M_A}\nabla_A^2 + \frac{1}{M_B}\nabla_B^2\right]. \tag{2.4}$$

In the centre-of-mass coordinate system

$$\hat{T}_n = -\frac{1}{2\mu}\nabla_R^2 \qquad \frac{1}{\mu} = \frac{1}{M_A} + \frac{1}{M_B}, \tag{2.5}$$

and the electronic kinetic energy operator, $\hat{T}_e$, takes the form (m_e = 1 a.u. in atomic unit)

$$\hat{T}_e = -\frac{1}{2}\sum_{i=1}^{N}\nabla_i^2 . \tag{2.6}$$

Moreover, the corresponding total wave-function must satisfy the time-independent Schrödinger equation

$$\hat{H}\Psi(\vec{r},\vec{R}) = E\Psi(\vec{r},\vec{R}), \tag{2.7}$$

$\Psi(\vec{r},\vec{R})$ can be write as a product of nuclear and electronic wave functions

$$\Psi\left(\vec{r},\vec{R}\right) = \sum_i F_i(\vec{R})\phi_i(\vec{r}\mid\vec{R}), \tag{2.8}$$

Here the $\phi_i(\vec{r}\mid\vec{R})$ are many-electron wavefunctions and the $F_i(\vec{R})$ are the wavefunctions for nuclear motion in electronic state, *i*. For a fixed internuclear distance ($\vec{R}$), equation (2.7) becomes:

$$\left(\hat{T}_e + \hat{V}(\vec{r},\vec{R})\right)\phi_i(\vec{r}\mid\vec{R}) = U_i(\vec{R})\phi_i(\vec{r}\mid\vec{R}). \tag{2.9}$$

Now, the eigenvalues, $U_i(\vec{R})$, and the eigenfunctions, $\phi_i(\vec{r}\mid\vec{R})$, depend upon the *fixed* internuclear coordinate $\vec{R}$. This leads to

$$\begin{gathered}\left[\hat{T}_n + U_i(\vec{R}) - E\right]F_j(\vec{R}) - \frac{1}{2\mu}\sum_i C_{ij}(\vec{R})F_i(\vec{R}) = 0 \\ C_{ij}(\vec{R}) = 2A_{ij}(\vec{R})\nabla_{\vec{R}} + B_{ij}(\vec{R})\end{gathered}, \tag{2.10}$$

where C_{ij} represents the coupling of different electronic states via the nuclear motion. Neglecting this electronic-nuclear coupling contained within the C_{ij} amounts to adopting both the Born-Oppenheimer and adiabatic approximations simultaneously, because the wavefunction is now restricted to one electronic state with the form determined solely by the electronic Schrödinger equation. Within this approximation equation (2.10) reduces to

$$\left[\hat{T}_n + U_j(\vec{R})\right]F_j(\vec{R}) = EF_j(\vec{R}). \tag{2.11}$$

This Schrödinger equation for the nuclei no longer consists of a set of coupled equations and can in principle be solved for each particular state *j*. The corresponding molecular wavefunction (2.8) is reduced to the simple product

$$\Psi_j\left(\vec{r},\vec{R}\right) = F_j(\vec{R})\phi_j(\vec{r}\mid\vec{R}). \tag{2.12}$$

Each $F_j(\vec{R})$ describes the behaviour of the nuclei moving in the potential field defined by the single electronic state $\phi_j(\vec{r}\mid\vec{R})$. The $\phi_j(\vec{r}\mid\vec{R})$ are known as adiabatic electronic functions and the corresponding eigenvalues $U_j(\vec{R})$ are known as adiabatic electronic potentials.

The Born-Oppenheimer and adiabatic approximations cannot be considered valid when two adiabatic states become nearly degenerate as the nuclear-electronic coupling term, C_{ij}, now becomes significant [37]. One class of systems for which such degeneracy of states is

important is the charge-transfer reactions. This is illustrated by considering the collision of two atomic systems $A + B$ that have an overall charge of 2+. Some of the adiabatic potentials will have an electron distribution of the form $(A^{+}+B^{+})$, while others will be of the $(A^{2+}+B)$ form. The $(A^{+}+B^{+})$ potentials will be totally repulsive due to the Coulombic repulsion, whereas those for the $(A^{2+}+B)$ distributions will be essentially flat, except for a large repulsive wall at small internuclear separations and perhaps a small potential well due to induced charges [38]. For systems with a suitably placed repulsive $(A^{+}+B^{+})$ potential below a neutral $(A^{2+}+B)$ potential, there will be a point, R_c, as the internuclear separation (R) decreases, at which the two potentials will approach the same energy value. Such a situation is illustrated in Figure 2.1.

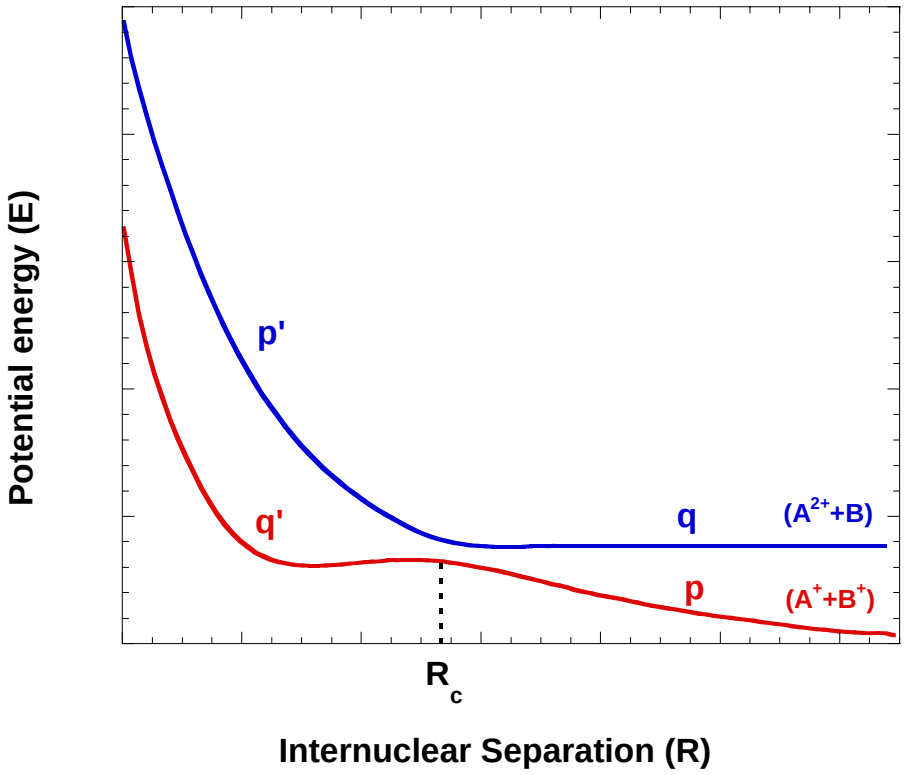

Figure 2.1 – An avoided crossing of adiabatic potential energy curves.

A collision between A^{2+} and B will initially follow the higher, flat potential and will cross the point R_c where the system's energy is now very close to that of an $(A^{+}+B^{+})$ potential. If, by some process, the system could "jump" nonradiatively to the nearby potential *and* the system ended the collision with this new electronic configuration, there would have been an effective transfer of an electron from B to A. Thus, the behaviour of the potentials at the point R_c is central to the overall rate of a possible charge-transfer reaction. As illustrated in Figure 2.1,

the adiabatic (A^{2+}+B) and (A^{+}+B^{+}) potentials will not actually cross one another no matter how close in energy they become. This is termed the *non-crossing* rule [35].

2.3.1. The Non-Crossing Rule

Within the Born-Oppenheimer and adiabatic approximations it is a general rule that, for a diatomic system, the energies of two purely electronic wavefunctions of the same symmetry can at no time become degenerate [35]. As a direct consequence, potential energy curves for the electronic states of a diatomic system plotted as a function of the nuclear separation, R, cannot cross one another. This sort of 'interaction' between two potential energy curves is termed an *avoided crossing* [37]. The potential energy curves of the two electronic states have a projected intersection at R_c; however, an energy gap effectively blocks the path of the potentials due to the non-crossing rule. For a system originally having an electronic configuration (A^{2+}+B) to remain in this configuration it would have to bridge this energy gap as it passes R_c. Failure to do so would result in it being converted to an (A^{+} + B^{+}) configuration and following the p' path in Figure 2.1.

In order to understand this behaviour, let us consider two orthonormal adiabatic (*i.e.* within the Born-Oppenheimer and adiabatic approximations) electronic states of the diatomic system, labelled $\phi_1(\mathbf{r}|R)$ and $\phi_2(\mathbf{r}|R)$. $U_1(R)$ and $U_2(R)$ denote the corresponding energies of these states, respectively. At a nuclear separation R_c the energies of these states, $U_1(R_c)$ and $U_2(R_c)$, are nearly degenerate and are also eigenvalues of the Hamiltonian, $\hat{H}_c$ at the nuclear separation R_c.

$$\hat{H}_c\phi_1(r \mid R_c) = U_1(R_c)\phi_1(r \mid R_c) \text{ and } \hat{H}_c\phi_2(r \mid R_c) = U_2(R_c)\phi_2(r \mid R_c). \tag{2.13}$$

Now, we must ask whether it is possible to make a small change δR such that U_1 and U_2 become equal. The perturbed Hamiltonian at R+δR can be written

$$\hat{H} = \hat{H}_c + \hat{V} \quad \text{with} \quad \hat{V} = \delta R \frac{\partial \hat{H}_c}{\partial R}, \tag{2.14}$$

where $\hat{V}$ is a small correction to $\hat{H}_c$.

Since δR is a very small displacement, the eigenfunctions, ψ, at R+δR can be written as a linear combination of the zeroth-order eigenfunctions, *i.e.*

$$\psi = c_1\phi_1 + c_2\phi_2. \tag{2.15}$$

Substituting equation (2.15) into

$$(\hat{H}_c + \hat{V})\psi = E\psi, \tag{2.16}$$

gives

$$c_1(U_1 - E + V)\phi_1 + c_2(U_2 - E + V)\phi_2 = 0\,. \tag{2.17}$$

Multiplying this by ϕ_1^* and repeating this procedure for ϕ_2^* gives the fellow pair of equations [39]:

$$c_1(U_1 - E + V_{11}) + c_2 V_{12} = 0 \tag{2.18}$$

and

$$c_1 V_{21} + c_2(U_2 - E + V_{22}) = 0\,, \tag{2.19}$$

here $V_{ij} = \langle\phi_i|\hat{V}|\phi_j\rangle$. $\hat{V}$ is Hermitian, so that V_{11} and V_{22} are real, and $V_{12} = V_{21}^*$. Equations (2.18) and (2.19) are homogeneous and have a non-trivial solution if and only if

$$\begin{vmatrix} U_1 - E + V_{11} & V_{12} \\ V_{21} & U_2 - E + V_{22} \end{vmatrix} = 0\,. \tag{2.20}$$

Expanding the determinant leads to the expression

$$E = \frac{1}{2}(U_1 + U_2 + V_{11} + V_{22}) \pm \sqrt{\frac{1}{4}(U_1 - U_2 + V_{11} - V_{22})^2 + |V_{12}|^2}\,, \tag{2.21}$$

which gives the first order energy eigenvalues at R+δR. For the states to be degenerate at this point (i.e. $U_1 = U_2$) it is required that

$$\sqrt{\frac{1}{4}(U_1 - U_2 + V_{11} - V_{22})^2 + |V_{12}|^2} = 0\,. \tag{2.22}$$

The left hand side of the equation is the square root of the sum of two squares, so the only way to satisfy the degeneracy condition is to insist that both

$$(U_1 - U_2 + V_{11} - V_{22}) = 0 \tag{2.23}$$

and

$$V_{12} = 0\,, \tag{2.24}$$

are simultaneously satisfied. However, there is only one arbitrary parameter δR. The only way in which this condition can be met is if the off-diagonal matrix element, V_{12}, is zero near the avoided crossing [37]. This will be the case if $\phi_1(\boldsymbol{r}|R)$ and $\phi_2(\boldsymbol{r}|R)$ are of different symmetries. This leads to the conclusion that only potential curves that correspond to electronic states transforming as different irreducible representations of the molecular point group may cross one another within the Born-Oppenheimer and adiabatic approximations [39]. It is the energy changes caused by the interaction of two near degenerate states of the same symmetry that produce the apparent repulsion seen between the potentials. If a collision process involving an avoided crossing of this kind is treated purely within the Born-Oppenheimer and adiabatic approximations, then only adiabatic processes would be described (*i.e.* those that remain on

the same adiabatic potential curve at all times during the collision). In reality, there is often a non-zero probability that a system will switch nonradiatively between two near-degenerate potential curves as it passes through an avoided crossing. A process involving such a transition is referred to as being nonadiabatic. In order to describe charge-transfer processes, we must calculate the probabilities of these nonadiabatic transitions. The simplest approach is the Landau-Zener approximation [40, 41]. This model has been specifically developed to deal with potential curve crossings at finite internuclear distance R_c. Such crossing occurs in collisions involving multiply charged ions because of the different nature of initial and final potential curves, e.g., an attractive polarization potential between ions and neutral atoms in the initial channel and a strong repulsive Coulomb potential between the two ions in the final electron capture channel. An extension of the Landau-Zener theory has been proposed by Tully and Preston [42] known as trajectory-surface-hopping method. The method allows transition not only in the vicinity of the avoid crossing but in all course of the collisions, therefore a precise knowledge of the potentials curves involved is required. More sophisticated approaches as the fully-quantal close-coupled scattering formalism [43] are also available.

2.4. Landau-Zener theory

The Landau-Zener model [40, 41] represents perhaps the simplest means of describing nonadiabatic transitions at the crossing of potential energy surfaces. Although its limitations are well known, the model continues to be used for a rough estimate of cross sections associated with various collision processes [44]. Here a brief description of the model as it is applied to charge-exchange processes of multiply charged ions will be given.

Let us consider a charge-exchange process, as described in equation (1.1), as:

$$A^{q+} + B \rightarrow A^{(q-1)+} + B^{+}. \tag{2.25}$$

At large internuclear distance R, the potential energy curves for the initial and final configurations are given by [45]

$$H_i(R) \cong \Delta E - \frac{q^2 e^2 \alpha(A)}{2R^4} \tag{2.26}$$

$$H_f(R) \cong \frac{(q-1)e^2}{R} - \frac{(q-1)^2 e^2 \alpha(A^+)}{2R^4} - \frac{e^2 \alpha\left(B^{(q-1)+}\right)}{2R^4}. \tag{2.27}$$

Here spherically symmetric states are assumed and consequently the terms $1/R^3$ in the potential are neglected. ΔE is the defect energy and α denotes the polarizability of the atom or ion being considered. If $\Delta E > 0$, the two curves cross at $R = R_c$ where R_c satisfies

$$\frac{(q-1)e^2}{R_c} = \Delta E - \frac{q^2 e^2 \alpha(A)}{2R_c^4} + \frac{(q-1)^2 e^2 \alpha(A^+)}{2R_c^4} + \frac{e^2 \alpha\left(B^{(q-1)+}\right)}{2R_c^4}. \tag{2.28}$$

In the Landau-Zener model one assumes that the transition (electron transfer in our case) is limited to a narrow region around the crossing point R_c [45]. One further assumes that in this narrow region the potential energy separations varies linearly with the internuclear distance,

$$H_i - H_f \cong \xi \cdot (R - R_c), \tag{2.29}$$

and the coupling matrix element H_{if}, which corresponds to the energy separation between the adiabatic state- representative curves at the avoided crossing, is constant. The constant ξ can be obtained for our case of charge transfer using equations (2.26) and (2.27), and can be most simply determined if polarization attraction is neglected [45]:

$$\xi = \left| \frac{d}{dR}(H_i - H_f) \right|_{R_c} \doteq \frac{q-1}{{R_c}^2}. \tag{2.30}$$

For the potential curves of the two quasimolecular states, single-electron capture can be described as a transition at the respective avoided crossing with interatomic distance R_c [45]:

$$R_c(a_0) = \frac{27,21(q-1)}{\Delta E / eV}. \tag{2.31}$$

The Landau-Zener transition probability as the system passes by the crossing point twice in a collision process is given by

$$P = 2\exp(-p)\left[1 - \exp(-p)\right], \tag{2.32}$$

here

$$p = \frac{2\pi H_{12}^2}{\hbar v \xi \left[1 - \left(\frac{b}{R_c}\right)^2\right]^{1/2}}, \tag{2.33}$$

b is the impact parameter, and v is the velocity of the ion at the crossing point. The integration of the probability P with respect to the impact parameter b yields the expression for the Landau-Zener cross section,

$$\sigma_{LZ} = 4\pi {R_c}^2 I(\eta) \tag{2.34}$$

where

$$I(\eta) = \int_1^\infty e^{(-\eta x)}(1 - e^{(-\eta x)}) x^{-3} dx, \quad \text{with} \quad \eta(v) = \frac{2\pi {H_{12}}^2}{\hbar v \xi}. \tag{2.35}$$

The application of the LZ-formula requires primarily appropriate values for the transition matrix element H_{12}. The latter can be obtained for the specific collision partners either by

calculation of the adiabatic energy curves or from perturbation theory. In first approximation, it can be estimated according to the empirical relation suggested by Olson [46]:

$$H_{if} = \tfrac{1}{4}\varepsilon_i\varepsilon_f(\varepsilon_i+\varepsilon_f)R_c \exp\left[-0.43(\varepsilon_i+\varepsilon_f)R_c\right]. \qquad (2.36)$$

All quantities in equation (2.36) should be expressed in atomic units, and ε_i and ε_f are determined by $\varepsilon_i = \sqrt{2I_i}$ and $\varepsilon_f = \sqrt{2I_f}$, where I_i and I_f are the effective ionization potentials of the electron before and after the transfer, respectively. In fact, the effective ionization I_i and I_f are those that define the defect energy, i.e. $\Delta E = I_f - I_i$. The empirical value shown in equation (2.36) is claimed by the authors to be correct within a factor of 2, therefore small adjustments can be made.

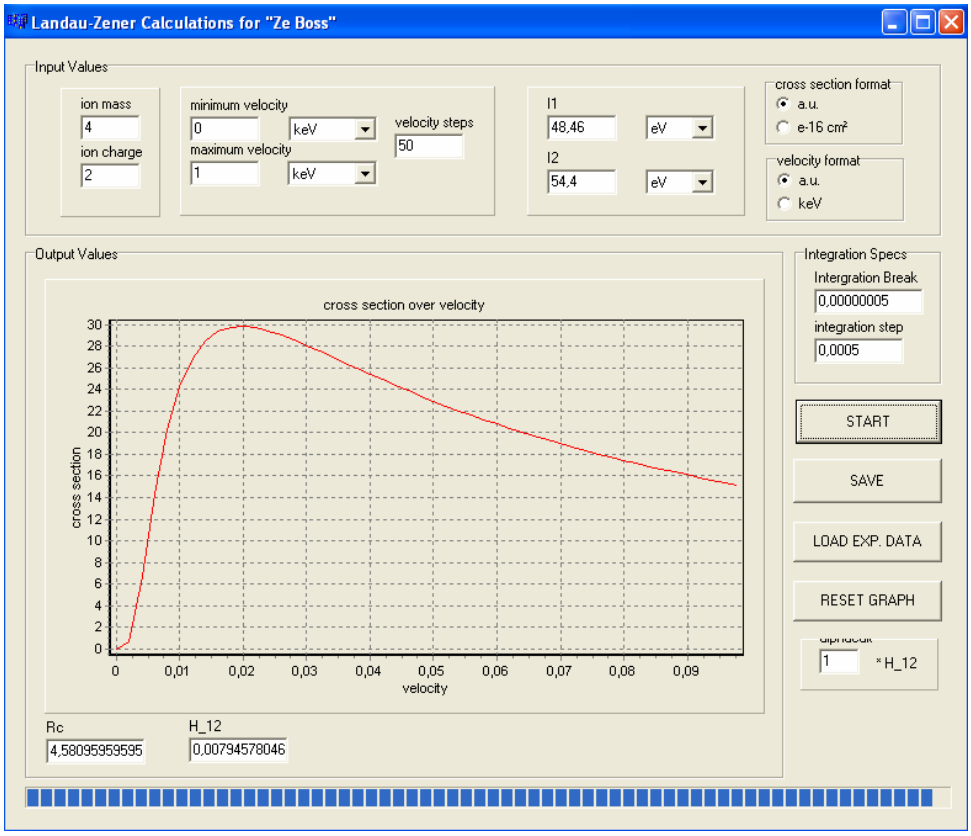

Figure 2.2 – Screenshot of the C++ based program used to calculate the Landau-Zener cross sections [47]. The SEC cross section for the system He^{2+}+Ne ($2s^2\ 2p^6\ ^1S$) → He^+ (1s) + Ne^{+*} ($2s2p^6\ ^2S$). I_1 = 48.46 eV is the energy necessary to capture one electron from Ne ($2s^2\ 2p^6\ ^1S$) plus the energy necessary to excite a second electron to the state Ne^{+*} ($2s2p^6\ ^2S$), while I_2 = 54.4 eV is the potential energy released by the projectile He^{2+} during the capture of one electron into ground state of He^+. In the bottom, the calculated crossing distance (R_c) and the coupling matrix element (H_{12}) are shown.

In this work, the Landau-Zener type calculations have been carried out by means of a C++ based code [47]. Figure 2.2 shows the screenshot of the developed program. The inputs are the projectile mass, projectile initial charge, and the ionization potentials. The program allows one to choose the impact velocity range as well as the unit for the output values. It is also possible to compare directly the experimental data, adjust the coupling matrix element and to save the calculated cross sections as a function of impact velocity.

2.5. Classical over-barrier model (OBM)

The principles of the classical over-the-barrier model were introduced by Bohr and Lindhard [48], and were further developed by Ryufuku et al. [49] and Bárány et al. [50]. Niehaus [51] and Ostrovsky [52] have extended the initially static model involving the effects of the relative velocity of the target and the projectile. More recently, Sattin [53, 54] has proposed some improvements to the OB model as to treat the barrier-crossing process by the electron within a simplified quantum mechanical formulation.

Despite of its simplicity, the model describes the overall features of electron capture processes rather well. It is based on the picture that the electron with a certain binding energy moves in the potential of the target core, superimposed onto the one for the projectile. For simplicity let's consider that only the most loosely bound electron is involved in the process. The ionic cores are regarded as hydrogen-like, i.e. the inner electrons are assumed to provide perfect screening. The most loosely bound electron, based on the classical consideration, will be bound to the target until the potential barrier between the target and the projectile drops below the binding energy level of the electron. The model partially treats the electron quantum mechanically. The Coulomb field of the approaching projectile induces a Stark shift of the electron's binding energy (in first order approximation):

$$I_b(R) = I_b - q / R, \tag{2.37}$$

where $I_b(R)$ is the binding energy at internuclear separation R , I_b is the binding energy at infinite internuclear separation, and q is the charge of the projectile. The potential experienced by the electron at distance r of its parental nucleus is:

$$V(r) = -\frac{q}{|R-r|} - \frac{1}{|r|}. \tag{2.38}$$

From this the potential barrier height between the target core and the projectile can be deduced:

$$V_{barr} = -\frac{\left(\sqrt{q}+1\right)^2}{R}. \tag{2.39}$$

As the projectile approaches the target this barrier drops. At a certain internuclear distance the barrier becomes lower than the binding energy of the electron. From that point on, the electron can move across the barrier, and it will belong to the projectile as well as to the target forming a quasi-molecular state (see Figure 2.3). When the target and projectile are separated again the electron will be bounded either to the projectile or to the target. Based on the model, electron capture is only possible if the closest approach is smaller than the critical distance (R_{crit}) at which the electron starts to become quasi-molecular. Assuming straight-line trajectories the closest approach of the projectile is equal to its impact parameter. Therefore the cross section of the process is:

$$\sigma = \pi R_{crit}^2, \tag{2.40}$$

where it is assumed that the probability of capture is 1 whenever the projectile approaches the target with smaller impact parameter than R_{crit}. The critical distance can be obtained by the condition that the electron binding energy I_b(R) is equal to the barrier height:

$$R_{crit} = \frac{2\sqrt{q}+1}{-I_b}. \tag{2.41}$$

Since recapture by the target is not accounted, this most simple version of the over-the-barrier model tends to overestimate the experimental cross sections. Another important question is which states the captured electron will occupy. This is mainly determined by the binding energy. The electron becomes quasi molecular with the binding energy $I_b(R_{crit})$. On the way out, at R_{crit}, the capture occurs and at this energy level the electron is resonantly transferred into a level of the projectile. One assumes that the quasi-continuum approximation is valid, i.e. the available states fill densely the energy diagram. The captured electron, however feels the Stark effect of the now ionized target. The asymptotic energy of the occupied state (with index *f* for final) therefore will be changed by $1/R_{crit}$:

$$I_f = I_b - \frac{q-1}{R_{crit}}. \tag{2.42}$$

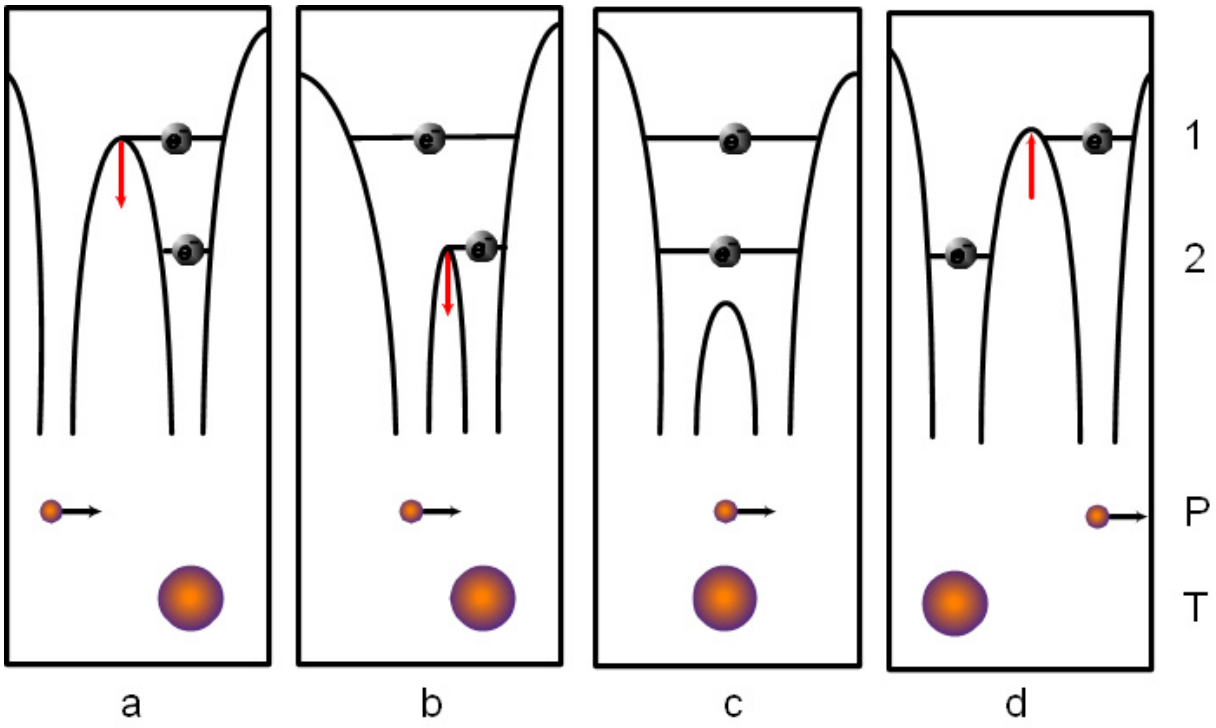

Figure 2.3 – Pictorial representation of the classical over the barrier model. a) Way in – the projectile is shown at the distance where the first electron is almost quasi-molecular. b) Way in – the potential barrier reaches the binding energy of the second electron, while the first electrons is quasi-molecular. c) The closest approach, in this representation both electrons can move freely between the nuclei. d) Way out – The most loosely bound electron is captured by the projectile and the second one is recaptured by the target.

So far, only one-electron processes were considered. In the extended version many-electron processes are also included, and therefore predictions for two- or more-electron capture are also possible. The basic model predicts that the cross sections are velocity independent. The distributions of the captured electrons between the different states, however, are very much dependent on the collision energy. With the dynamic version of the model this can be explained and the relative populations of the states can be given.

2.5.2. The extended Over-barrier model (EOBM)

In this section, we will mainly follow the EOBM version proposed by Sattin [53, 54]. We consider the standard scattering experiment described in equation (2.25) and label **T**, **P**, and **e** respectively the target, the projectile ion, and the electron. The system **T**+**e** is the initial neutral atom. Let **r** be the electron's position vector relative to target nucleous and **R,** the distance between the target and projectile nucleus. Let us further consider the plane $\mathcal{P}$

containing all the three particles and use cylindrical polar coordinates $(\rho, z, \phi \equiv 0)$ to describe the position of the electron within this plane. We can assign the z axis to the direction along the internuclear axis. The two nuclei are considered as approaching at a velocity which is small compared to the orbital electron velocity. The total energy of the electron is:

$$E = \frac{p^2}{2} + U = \frac{p^2}{2} - \frac{Z_t}{\sqrt{\rho^2 + z^2}} - \frac{Z_p}{\sqrt{\rho^2 + (R-z)^2}}. \tag{2.43}$$

Z_p and Z_t are the effective charge of the projectile and of the target as seen by the electron, respectively. In the model a hydrogen-like approximation for both the target and the projectile is used, therefore an effective charge $Z_t = 1$ is assigned to the target and an effective quantum number n is used to label the binding energy of the electron:

$$E_n = Z_t^2 / 2n^2 = 1/2n^2 . \tag{2.44}$$

On the plane $\mathcal{P}$ we can draw a section of equipotential surface which represents the limit of the region classically allowed to the electron:

$$U(z, \rho, R) = -E_n - \frac{Z_p}{R}. \tag{2.45}$$

When $R \to \infty$, this region is divided into two disconnected circles centred around each of the two nuclei. Initial conditions determine which of the two regions actually the electron lives in. As R diminishes there can be eventually an instant where the two regions become connected (see Figure 2.4). Figure 2.5 shows a representation of a section of the equipotential surface. It is the opening of the equipotential curve between **P** and **T** that leads to a leakage of electrons from one nucleus to another, and therefore to charge exchange.

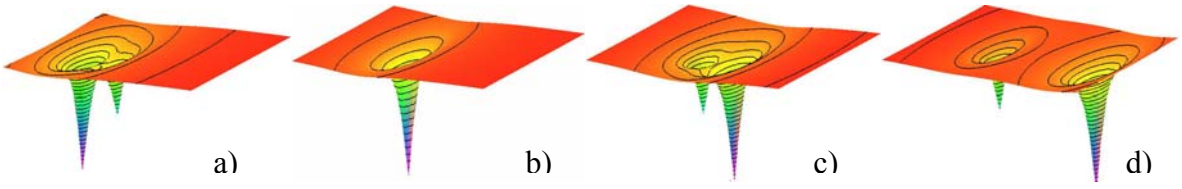

Figure 2.4 – Example of two-centre Coulombic potential as calculated by EOB model. a) Way in – the projectile (deeper well) is shown at the right side and is moving toward the target (shallower well) direction. b) The closest approach. c) Way out – the target and the projectile are separating to each other and the potential barrier is increasing. d) Way out – the target and the projectile are very well separated.

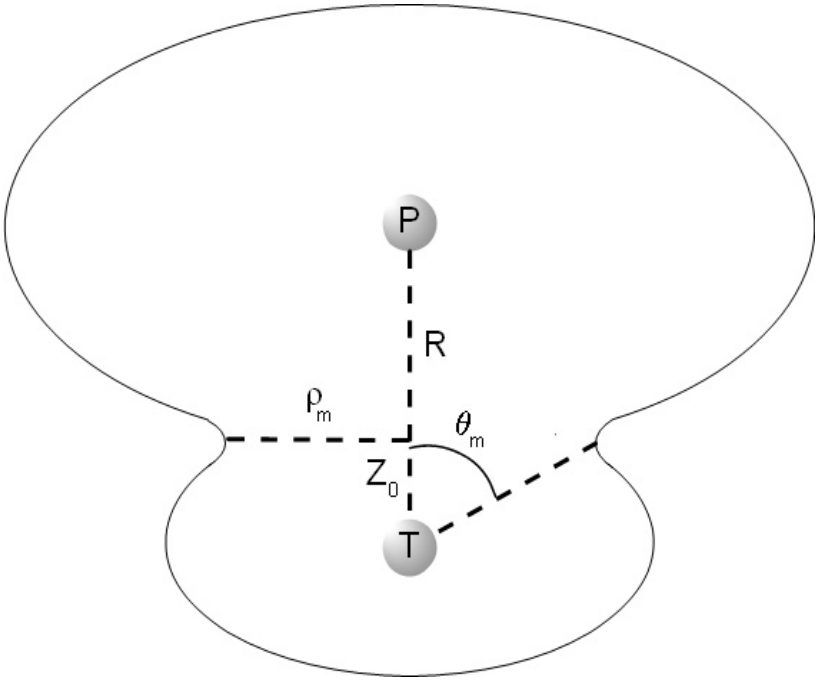

Figure 2.5 – Representation of a section of the equipotential surface $U = E$, i.e., it is border of the region classically accessible to the electron. R is the internuclear distance. The parameter ρ_m is the radius of the opening that joins the potential wells, θ_m the opening angle from **T** and z_0 is the position of the potential's saddle point.

Solving the equation (2.45) for R by imposing a vanishing width of the opening $(\rho_m = 0)$ and also by imposing that there is a unique solution for z in the range $0 < z < R$ one obtains [54]:

$$R_m = \frac{\alpha\sqrt{Z_p}+1}{E_n} \tag{2.46}$$

where α is a parameter that adjusts the value of the R_m [54]. In the region of opening, the potential U has a saddle structure along the internuclear axis with its maximum at

$$z = z_0 = R\frac{1}{\sqrt{Z_p}+1}. \tag{2.47}$$

Charge loss occurs when the electron is able to cross this potential barrier. Let N_Ω be the fraction of the trajectories that lead to electron loss at the time t. N_Ω is a function of the solid opening angle Ω, whose projection on the plane is the $\pm\theta_m$ angle. The quantity we are interested in is *W(t)*: the probability for the electron to be still bound to the target, at time t. Its rate of change is given by [52]

$$dW(t) = -N_\Omega dt\frac{f_T}{T_{em}}W(t). \tag{2.48}$$

In this expression, $dt\, f_T / T_{em}$ is the fraction of electrons that cross any surface perpendicular to their motion (and enter the loss region) within time interval *dt*. T_{em} is the unperturbed period of the electron motion along its orbit, and f_T, a corrective term that accounts for the perturbation: in absence of the projectile it would be $f_T = 1$. The unperturbed period is obtained by $T_{em} = 2\pi n^3$. The leakage probability is given by [53]

$$\begin{aligned} P_l &= P(+\infty) = 1 - W(+\infty) = \int_{-\infty}^{+\infty} dW(t) \\ &= 1 - \exp\left(-\frac{f_T}{T_{em}} \int_{-t_m}^{+t_m} N_\Omega dt \right). \end{aligned} \tag{2.49}$$

In order to integrate equation (2.49) we need to know the collision trajectory, then an unperturbed straight line with impact parameter b can be assumed,

$$R = \sqrt{b^2 + (vt)^2} \tag{2.50}$$

The fraction of the trajectories that lead to electron loss at the time *t* is given by (for more details see [53, 54]):

$$N_\Omega(t) = \frac{1}{2} \frac{\sqrt{Z_p}}{\left(\sqrt{Z_p} + 1\right)^2} \left[\left(\sqrt{Z_p} + 1\right)^2 - Z_p - \frac{E_n R(t)}{Z_t} \right]. \tag{2.51}$$

The limits of the time integration in equation (2.49) are defined by the R_m distance:

$$t_m = \frac{1}{v} \sqrt{R_m^2 - b^2}, \tag{2.52}$$

The SEC and DEC classical probabilities are given by [55]:

$$\begin{aligned} P_{SEC} &= 2P_l(1 - P_l) \\ P_{DEC} &= P_l^2 \end{aligned} \tag{2.53}$$

The cross section can be finally obtained after integrating over the impact parameter, the integration extends till the maximum b allowed: $b_m = R_m$

$$\sigma_{SEC,DEC} = 2\pi \int_0^{b_{\max}} b P_{SEC,DEC}(b) db. \tag{2.54}$$

In order to compute the SEC and DEC cross sections a C++ code has been written [56]. Figure 2.6 shows the screenshot of the developed programme. The inputs are the projectile mass, projectile initial charge, target mass and the electron binding energy. The program allows one to choose the impact velocity range as well as the unit of the output values. It is also possible to compare directly the experimental data, adjust the parameters α and f_T. It also saves the calculated cross sections as a function of impact velocity.

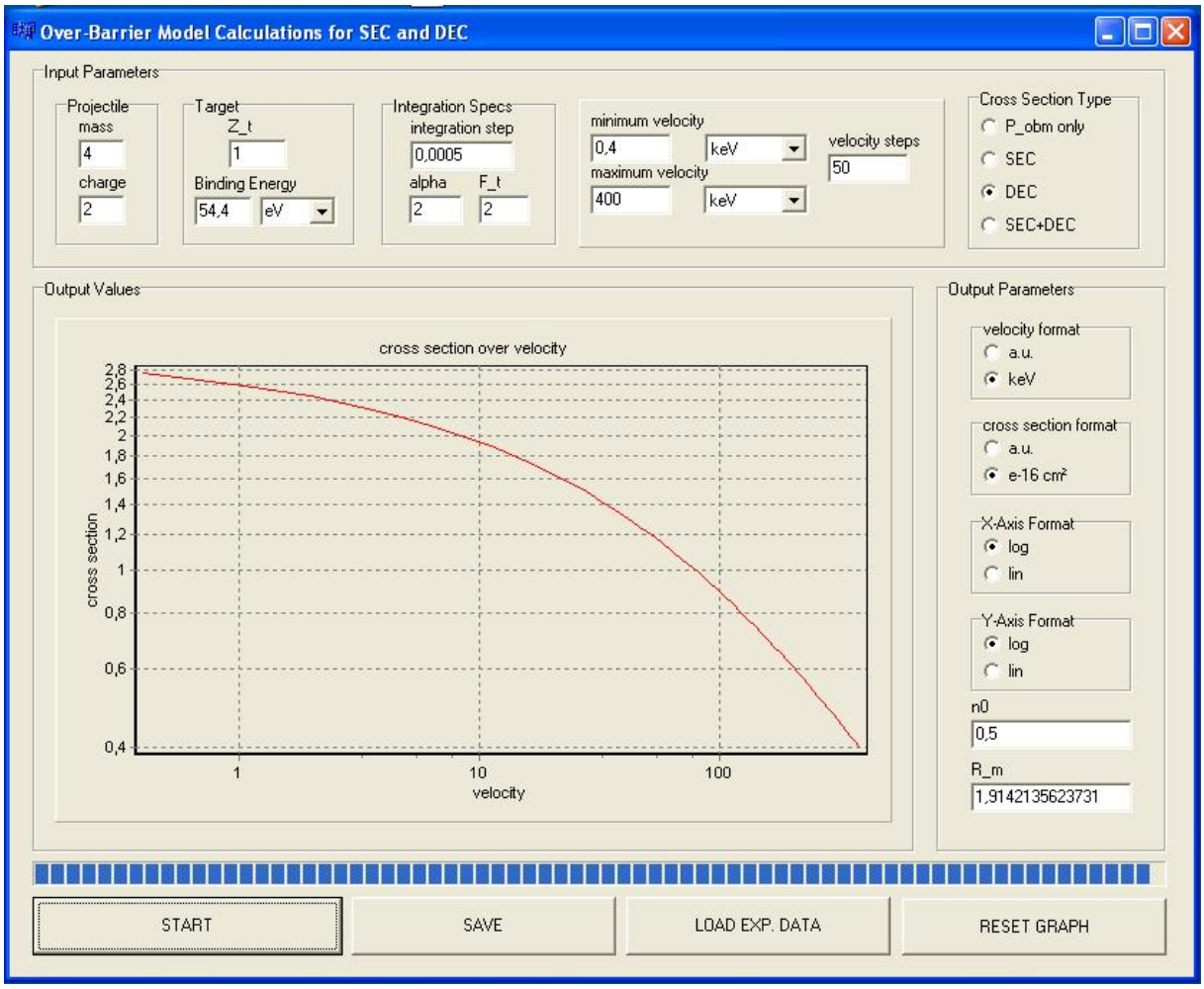

Figure 2.6 – Screenshot of the C++ based program used to calculate the EOBM cross sections. As an example, values for DEC for He^{2+} – He collisions are shown.

3. Experimental setup

3.1. Introduction

The aim of this thesis is to obtain detailed information on electron capture and ionization processes in collisions of ions with atoms and molecules, by measuring the cross sections dependencies on impact energy. For this purpose we have constructed a novel experimental setup which combines different techniques in order to measure absolute cross sections for single (SEC) and double electron capture (DEC) in collisions of slow singly and multiply charged ions with gaseous atoms and molecules.

In this chapter an overview of the experimental setup will be given. The ion beam production is discussed, starting with a brief and general description of the Electron Cyclotron Resonance Ion Source (ECRIS), followed by a description of the charge exchange apparatus "SAMBA" (Studies on Atomic and Molecular collisions by Beam Attenuation). This description also includes the electrostatic lenses properties, pressure measurement and electrical connections. Finally, the data acquisition system is presented.

3.2. Ion source and beam transport

The projectile ion beam is generated by means of a compact home-built 14.5 GHz ECR ion source named "SOPHIE" (**SO**urce for **P**roduction of **H**ighly charged **I**ons using **E**CR) which was developed in co-operation between the Vienna University of Technology and the Justus-Liebig University in Gießen [57, 58].

An ECRIS is basically a magnetic bottle which confines a dual-temperature plasma, containing hot electrons and cold ions. Multiply charged ions are produced by means of sequential electron impact ionization.

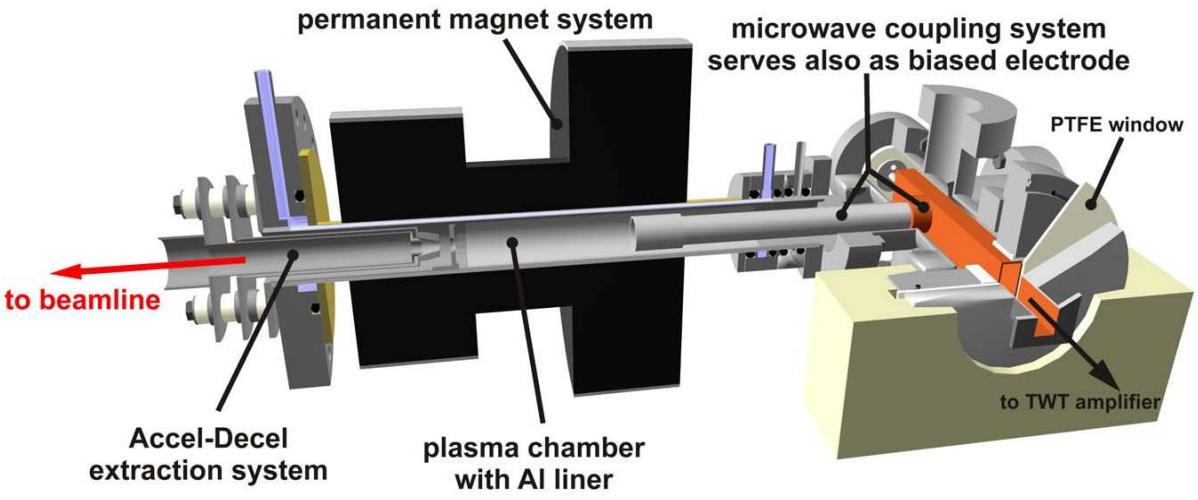

Figure 3.1 - Cutaway view of the 14.5 GHz all permanent magnet ECRIS "SOPHIE" (total length app. 50 cm) [57].

In an ECRIS plasma electrons gyrate around magnetic field lines according to their cyclotron frequency $\omega_c = eB/m_e$. By applying microwave radiation the electrons gain energy in magnetic field regions where their cyclotron frequency ω_c equals the microwave frequency. A review and historical overview on ECRIS can be found in [59].

A schematic view of the ion source "SOPHIE" is shown in Figure 3.1. The magnetic field configuration is provided by four permanent magnet rings and a Halbach-type hexapole and has a so-called minimum-B configuration, in which the plasma is confined. The plasma heating is done by injection of microwaves with a total power of up to 350 W in the frequency range of 12.75 to 14.5 GHz which is transmitted from the microwave system at ground potential through a Poly Tetra Fluoro Ethylene (PTFE) window into the water cooled 25 mm diameter plasma chamber. After the PTFE window, there is an insulated waveguide coupling system which allows the transition of a rectangular to a circular waveguide and which can also be used as a biased electrode. An aluminium liner at the confinement region enhances the production of highly charged ions. The plasma chamber is pumped by a small turbo-molecular pump at ground potential through an insulating break. Two gas inlet valves, connected via an insulating break, permit operation in the gas-mixing mode. The triode "Accel-Decel" extraction system permits ion acceleration voltages between 1 and 10 kV.

The ion source is fully controlled by a LabVIEW-based [60] programme called "CODIAN" developed at the Hahn-Meitner Institute in Berlin [61].

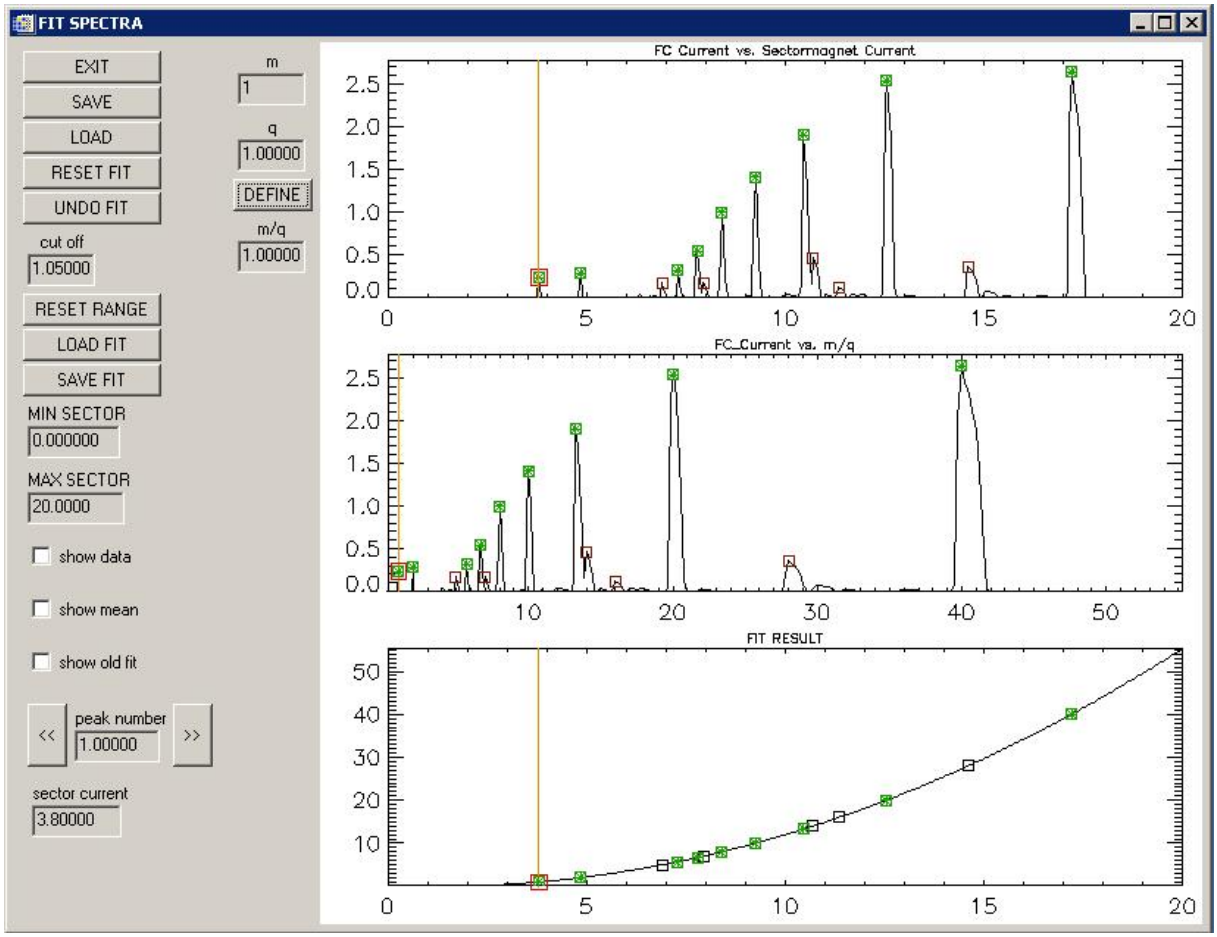

Figure 3.2 - Screenshot of the IDL-program used to calibrate mass-over–charge spectra acquired with CODIAN [57].

The extracted ion beam is focused by a magnetic quadrupole system and then mass-to-charge-analyzed by a 60° sector magnet and guided to the specific beam line. The mass-over-charge spectra are acquired by "CODIAN" as a function of the separation-magnet current. Due to the remanence of the separation magnet currents for achieving a specific mass-over-charge ratio, it is necessary to calibrate the acquired charge-state spectra according to well identified mass-over-charge peaks. For this purpose an IDL program has been utilized [57]. After loading the raw data, the spectrum is plotted and two or more peaks must be identified by the user in order to obtain the mass-over-charge fit for the whole spectrum. The program calculates a calibration curve for the spectrum using a least-square fit routine (see Figure 3.2).

Before travelling to the charge-exchange apparatus, the desired ion beam is steered horizontally and vertically by a first set of deflection plates and collimated by an aperture with 2.5 mm diameter. This aperture is mounted electrically insulated such that the ion beam current on it can be monitored. A second set of deflection plates can be used to guide the ion beam into a set of 4 cylindrical electrostatic lenses for focusing and deceleration. Typical

beam-line vacuum is $<10^{-7}$ mbar, which is low enough to prevent significant losses due to charge changing collisions with background gas. A schematic view of the entire experiment setup is shown in Figure 3.3.

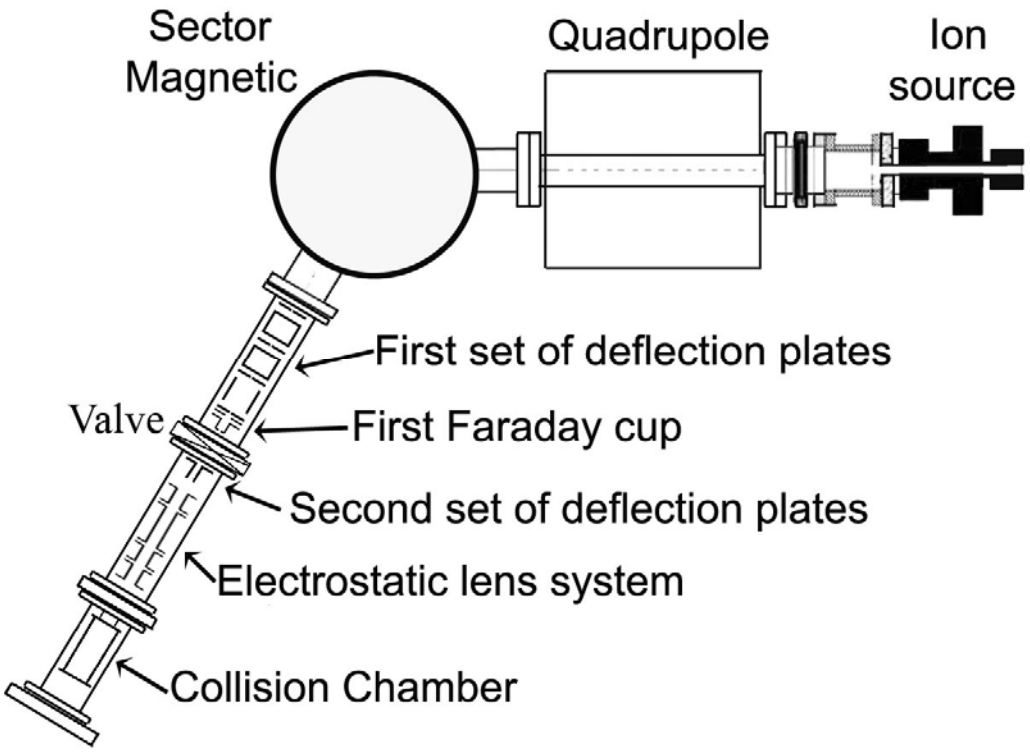

Figure 3.3 – Schematic view of the experimental setup at TU-Wien. Only the beam line used in this work is shown.

3.3. Studies on Atomic and Molecular collisions by Beam Attenuation (SAMBA)

3.3.1. Electrostatic lenses

In order to assure that the ion beam is collimated when it enters the collision chamber even in cases when the ions are decelerated, a set of electrostatic lenses is placed before the collision chamber. By means of SIMION ion trajectory simulations [62] optimal geometry and field shapes for spatial focussing have been calculated. SIMION makes use of potential arrays that define the geometry and potentials of electrodes on which the Laplace equation is solved. The developed geometry file and generated potential arrays are given in the appendix of this thesis. It turned out that for our setup one needs four lens elements before the collision region.

The constructed electrostatic lenses setup is shown schematically in Figure 3.4. This figure also includes a representation of the potentials applied to the system. The setup consists of lens elements L1, L2, L3 and L4 which have 3.3 cm, 8.4 cm, 5.8 cm and 4.0 cm length, respectively. The charge-exchange apparatus is connected to the last electrostatic lens (L4) which defines the final collision energy and has a 3 mm diameter collimator aperture. The lenses radius is 20.5 mm and the gap between the elements is about 1.0 mm. The total length of the lens system including the gas cell is 40.4 cm.

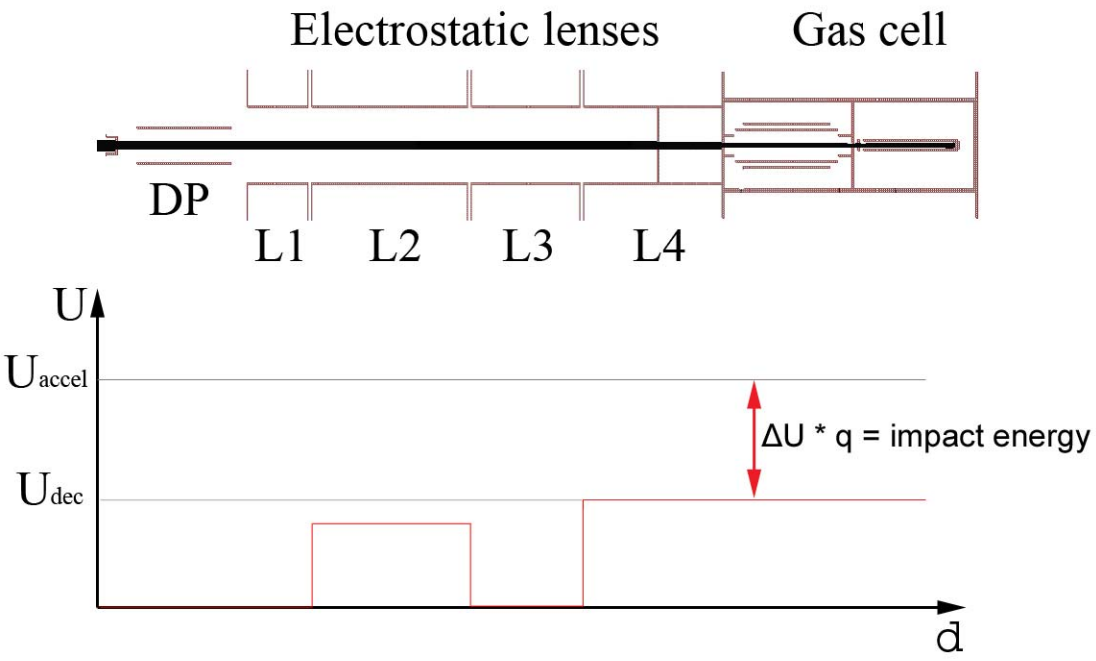

Figure 3.4 – Schematic view of the electrostatic lenses and the charge exchange apparatus with a representative potential applied to the system. The deflection plate system (DP) is placed before the electrostatic lenses, subsequent are the lens elements L1, L2, L3 and L4 and finally the gas cell. Two potentials are applied to the system: a deceleration potential voltage (U_{dec}) at the gas cell and the last lens element (L4), and a focusing potential at L2 (U_{L2}) (see text).

In Figure 3.5 a cross section view of the electrostatic lens geometry is shown, including a potential-view calculated by SIMION [62]. A He^{2+} ion beam is travelling through the system with a kinetic energy of 2 keV and an initial opening angle of 3°. No focusing voltage is applied to the system, i.e. the entire system is at ground potential. Figure 3.6 shows the same setup where a deceleration voltage (U_{dec}) of 900 V is applied to the gas cell while all others elements are kept at ground potential. It is possible to see that, for a such high deceleration voltage, a strong focusing is created by lens element L4. This focus effect, however, increases the ion beam diameter at the collision chamber entrance and therefore

reduces the ion beam intensity in the collision region. In order to correct this effect, an additional electrostatic voltage must be applied to element L2. Figure 3.7 shows the simulation where two voltages are applied. A positive voltage (U_{L2}) of 800 V is applied to the lens element *L2*, while the collision chamber is at deceleration voltage U_{dec} = 900V. The others lens elements are on ground potential (U_{L1} = U_{L3} = 0 V). These simulations were carried out for several ion species and kinetic energies and, as a general conclusion it was found that applying a voltage of $U_{L2} = U_{dec} - 100$ to the lens element *L2* is usually sufficient to reach a collimated and intense enough ion beam profile in the collision region. These SIMION calculations have been successfully verified in our experimental investigations.

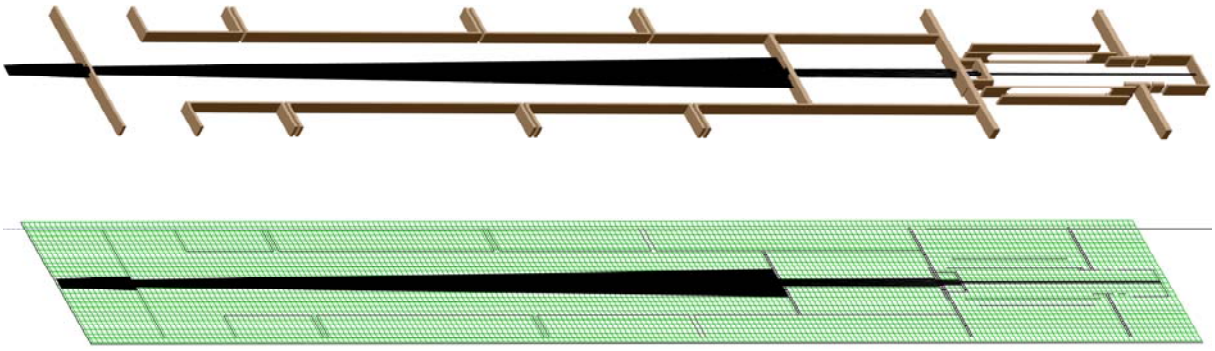

Figure 3.5 – A SIMION simulation of the electrostatic lenses system and collision chamber. A He^{2+} ion beam with 2 keV and an initial opening angle of 3° passes through the centre of the system which has a cylindrical symmetry. In the bottom the potential-view is shown. In this simulation no voltage is applied to the system.

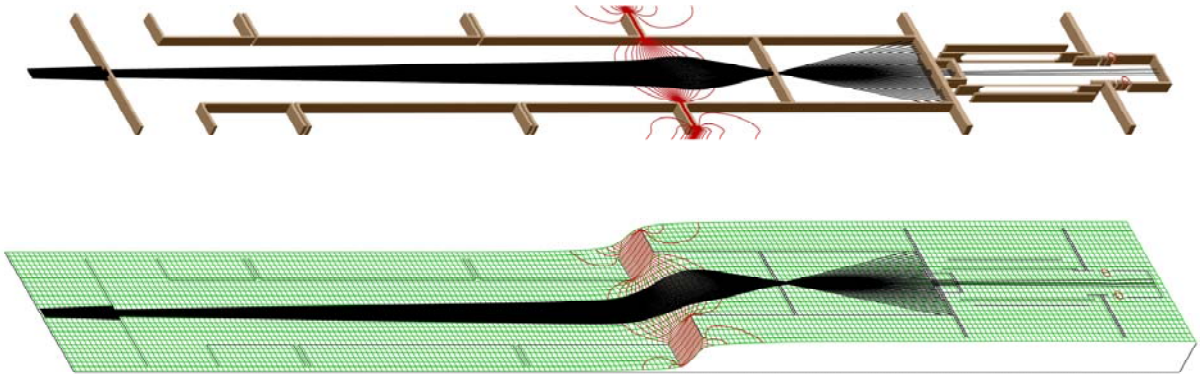

Figure 3.6 – A SIMION simulation of the electrostatic lenses system and collision chamber. A He^{2+} ion beam with 2 keV and an initial opening angle of 3° passes through the centre of the system, now a deceleration voltage (U_{dec} = 900 V) is applied to the charge exchange apparatus which is connected to lens L4, all other component are kept at ground potential. In the bottom the potential-view is shown.

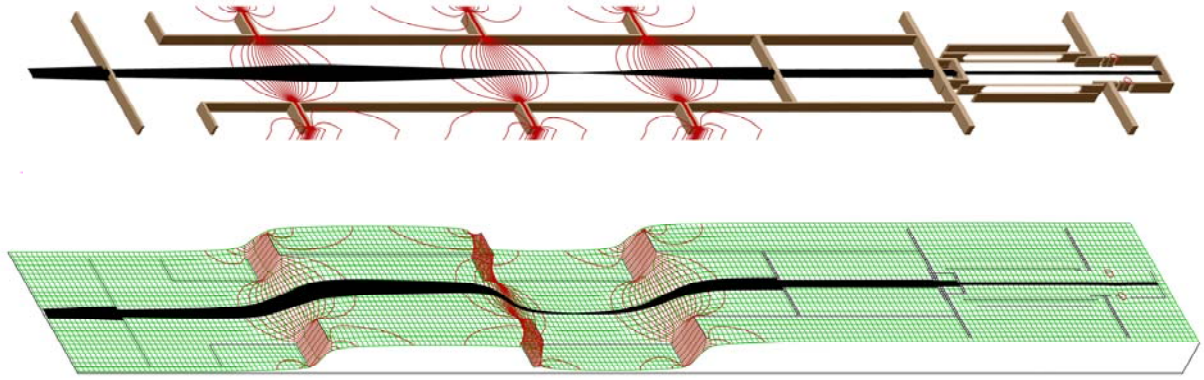

Figure 3.7 – A SIMION simulation of the electrostatic lenses system and collision chamber. A He^{2+} ion beam with 2 keV and an initial opening angle of 3° passes through the centre of the system. Two voltages are applied to the system: a deceleration voltage (U_{dec} = 900 V) to the charge exchange apparatus and a voltage of 800 V to the lens element L2, all other component are kept at ground potential. In the bottom the potential-view is shown.

3.3.2. Collision chamber

The collision chamber constructed during this thesis is shown schematically in Figure 3.8. – Figure 3.10. All components described here are made of stainless steel, unless otherwise explicitly mentioned. An insulated aperture (A_1) with a 2.5 mm diameter slit is fixed at the chamber entrance and serves for monitoring the incoming ion beam current (Figure 3.8 element 1). Inside the chamber is a first Faraday cup (FC_1) which is fixed by an insulator Teflon ring (Figure 3.8 elements 3 and 4, also shown in the zoom-in). FC_1 has a 1 mm aperture for normalizing the ion current measured in the second Faraday cup (FC_2) to the incoming ion current.

The collision region is covered by a meshed cylinder and a slow particle collector (Figure 3.8 elements 6 and 7, respectively). The meshed cylinder and the collector are aligned by two Teflon insulator holders with six holes each (Figure 3.8 element 5). These holes permit the target gas to flow into the collision region. The meshed cylinder consists of a cylindrical supporting structure with 6 slits, each with an area of 195 mm^2 around which a 0.1 mm molybdenum wire is coiled, with each turn separated by 2 mm, resulting in a 98% transparency of the mesh. Figure 3.9 shows the meshed cylinder built as depicted in the

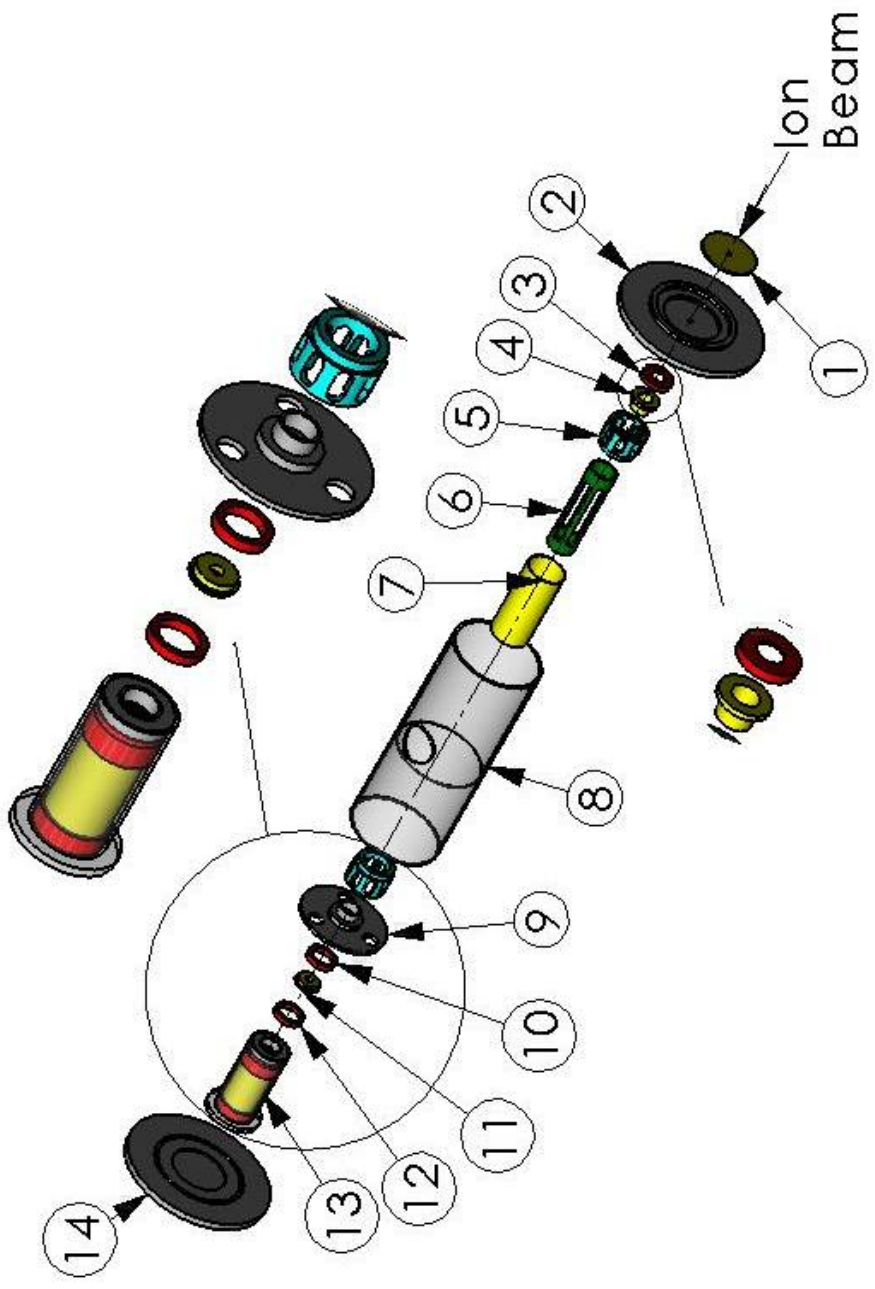

Figure 3.8 – Exploded view of the collision chamber apparatus used for electron-capture cross-section measurements. ① First isolated plate (A_1) with 2.5 mm diameter slit. ② Gas chamber entrance with 2 mm diameter slit. ③ Insulator ring for the first Faraday cup. ④ First Faraday cup (FC_1) for incoming current normalization. ⑤ Insulator holder for meshed cylinder and slow particles collector. ⑥ Meshed cylinder. ⑦ Slow particle collector. ⑧ Gas chamber external cylinder with aperture for target gas inlet. ⑨ Flange for aligning the system with 10 mm diameter slit. ⑩ Insulator ring. ⑪ Isolated ring with 10 mm diameter aperture for retarding of doubly charged ions. ⑫ Insulator ring. ⑬ Faraday cup (FC_2) for ion attenuation measurement. ⑭ End flange of gas chamber.

SIMION programme. The main purposes of the meshed cylinder are to keep a uniform electric field in the collision region, to define the final impact energy and to allow slow charged particles (recoiling ions and electrons from the target gas) to reach the collector.

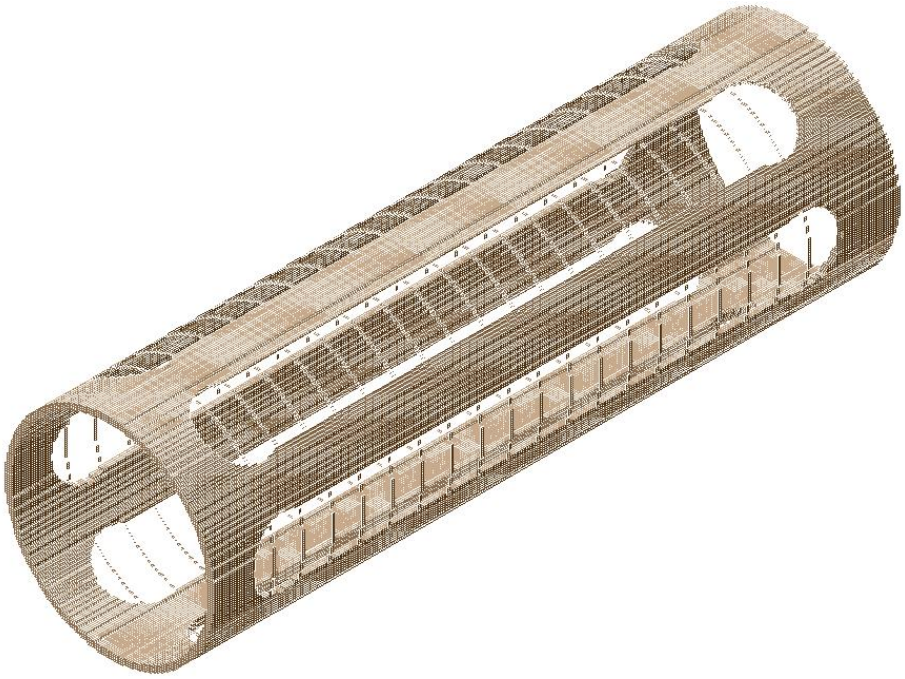

Figure 3.9 – Detailed view of the meshed cylinder (element 6 in Figure 3.8).

Behind the collision region a biased aperture A_2 (Figure 3.8 element 11) can be used for discriminating singly charged ions produced by SEC from doubly charged ions. The procedure is called "beam stopping mode" and will become clear in the next sections. With a 10 mm diameter aperture, A_2 accepts a mean scattering angle of ± 8° and it can also be used to check the ion beam-opening angle. Subsequent to A_2 a suppressor ring is biased negatively in order to keep secondary electrons in FC_2 where the attenuated ion current is measured.

Figure 3.10 shows the assembled charge exchange apparatus. The detailed dimension for each component is shown in the appendix of this thesis. The entire gas chamber has 13 cm total length and all components are placed inside an external cylinder which has an aperture for target gas inlet, see Figure 3.8 element 8. The gas chamber is divided internally by a flange which is used to align the system. This flange has a set of holes in order to assure a uniform gas pressure in the gas chamber, see Figure 3.8 element 9. The system is closed by an end flange which holds the FC_2. All electrical connections are guided through this flange (Figure 3.8 element 14).

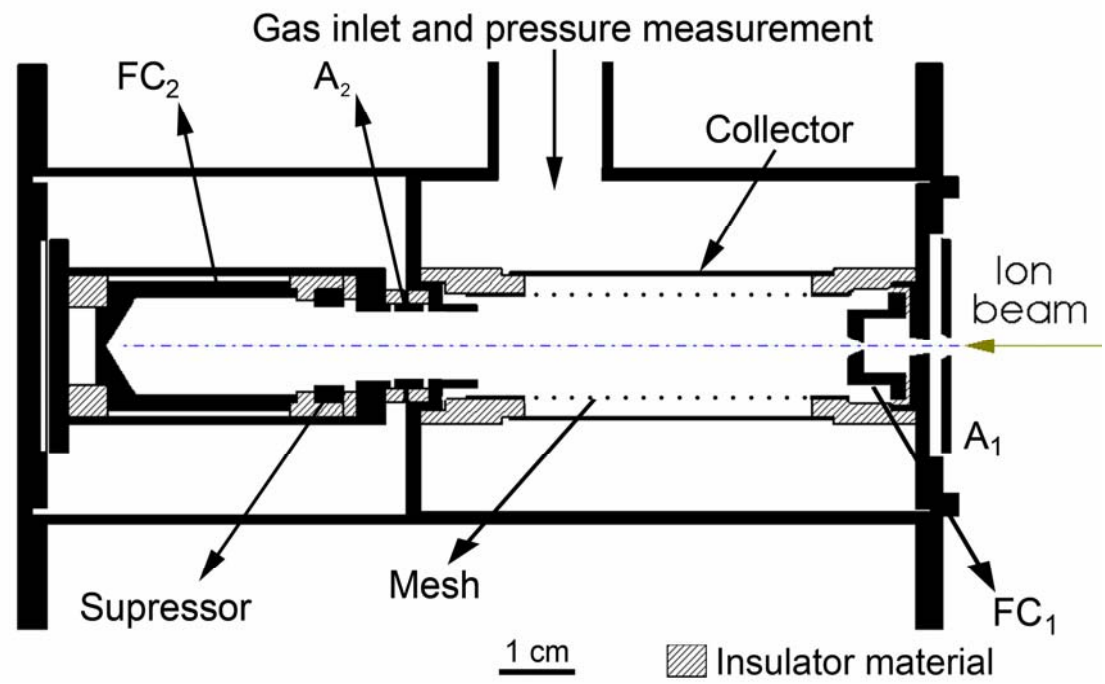

Figure 3.10 – Scheme of the assembled charge exchange experiment.

3.3.3. Vacuum system, gas injection and pressure measurement

The charge exchange apparatus is placed in a 100 CF cross recipient. The pre-vacuum system is evacuated by means of a rotary vane pump and the high vacuum conditions are reached by a 240 l/s turbo-molecular pump. The background pressure in the housing chamber is measured by a Penning gauge and is normally in the lower 10^{-8} mbar range while the pressure inside the gas chamber is generally one order of magnitude higher. Figure 3.11 shows a schematic view of the vacuum system, gas inlet and pressure measurement.

The target gas is admitted through a needle valve and transported to the collision chamber via a connector gas tube with electrical insulator break. The total pressure in the gas cell is measured by a capacitance manometer (Baratron). The purity of the target gas is monitored by a quadrupole partial pressure gauge (QPPG). Figure 3.12 shows a typical residual gas spectrum inside the gas chamber measured by the QPPG after one day of pumping. At a total pressure of $3.3 \cdot 10^{-6}$ mbar, high percentages of N_2 and H_2O are present. Figure 3.12b shows the pressure spectrum when the gas cell is filled with argon gas at a typical work pressure of $1.0 \cdot 10^{-4}$ mbar. With 5% of the total pressure N_2 is intolerably high. For normal operation, the total pressure in the gas cell therefore has to be about $1.0 \cdot 10^{-7}$ mbar, where residual gases like N_2 and H_2O amount are less than 0.1% of the total background pressure when target gas is admitted to the collision chamber.

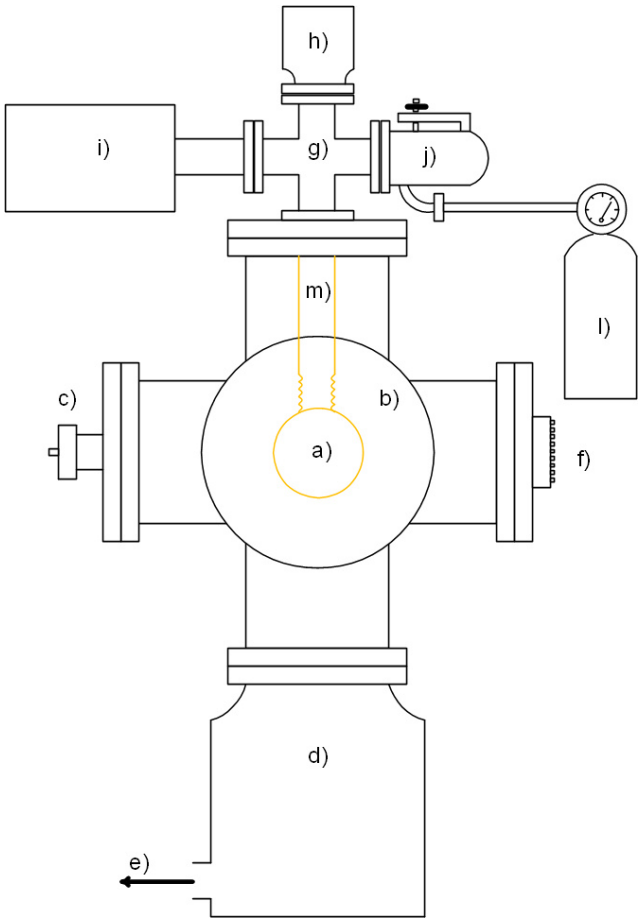

Figure 3.11 – End view of the experimental setup. a) charge exchange apparatus, b) 100 CF cross recipient, c) Penning pressure gauge, d) 240 l/s turbo-molecular pump, e) to rotary vane pump, f) electrical connections, g) 35 CF cross, h) capacitance manometer – Baratron, i) quadrupole partial pressure gauge, j) needle valve, l) target gas bottle, m) connector gas tube with electrical insulator break.

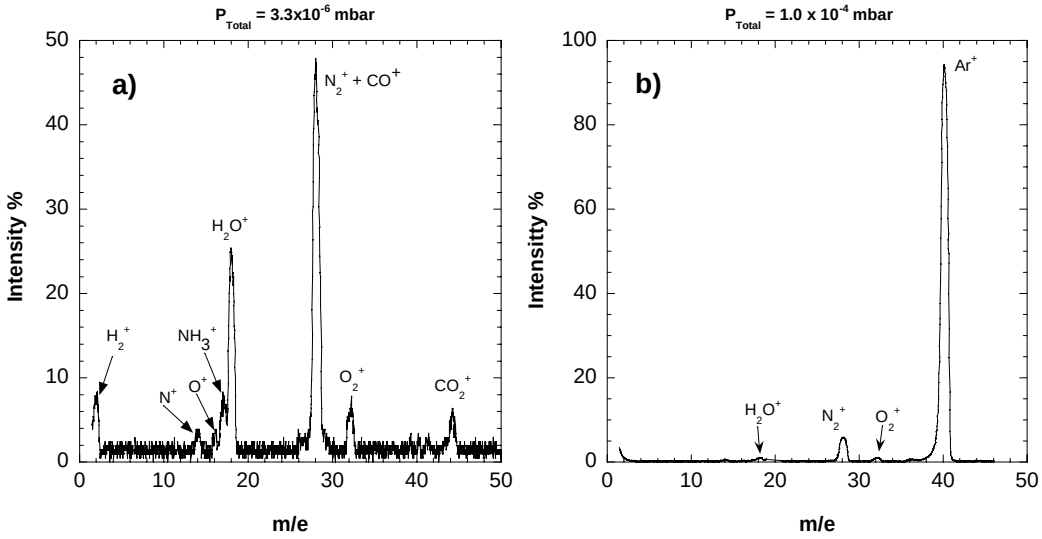

Figure 3.12 – Partial pressure spectra as measured by the quadrupole gauge inside the gas chamber. a) spectrum of residual gases, note that the gas intensities are given in percentages of the background pressure of $3.3 \cdot 10^{-6}$ mbar. b) spectrum for the case of argon gas injection (partial pressures in percentages of a pressure of $1.0 \cdot 10^{-4}$ mbar).

3.3.4. Electrical connections

Figure 3.13 shows a schematic representation of the electrical connections for the electrostatic lens system and the collision chamber. The deflection system consists of two pairs of parallel plates positioned vertically and horizontally. The power supply connected to the deflection plates provides a maximum voltage of 60 V and can have the polarity inverted in order to change the beam deflection direction. The electrostatic lenses can be tuned independently and are connected to three distinct stabilized power-supplies which deliver a voltage of 3000 V maximum.

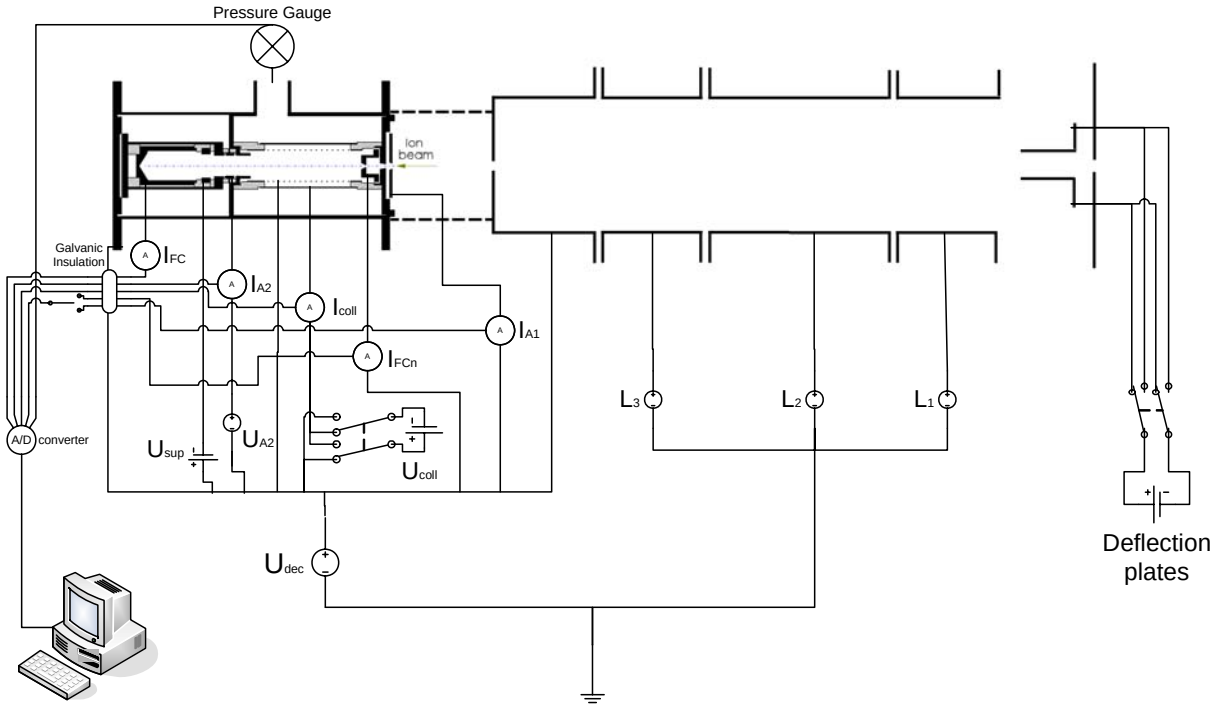

Figure 3.13 – Scheme of electrical connections for the electrostatic lens system and the collision chamber.

The voltage applied to the gas cell (U_{dec}) is the reference potential for the other components of the charge exchange system, i.e. it is the "high voltage ground". The plate A_1, Faraday cup for normalization (FC_1), meshed cylinder, plate A_2 and the Faraday cup for current measurement (FC_2) are biased at the same potential as the gas cell. The suppressor is biased always negatively with respect to the potential applied to the gas cell (U_{dec} - 50V) in order to keep secondary electrons in the last Faraday cup. The collector is biased either slightly positively or negatively with respect to U_{dec} depending whether collection of electrons

or ions is desired. Five picoammeters are dedicated to measure the currents. Those picoammeters are put on "high-voltage ground" using an insulator transformer. The picoammeters are equipped with an output signal voltage which is proportional to the measured current. This output signal is connected to a galvanic insulator in order to transform the signal to low voltages so it can be connected to the data acquisition system.

The voltage settings are divided in three different modes depending on which event we are interest in, as shown in Table 3.1. The measurement modes will become clear in the chapter 4.

Table 3.1 – Voltage settings for three different measurement modes as a function of U_{dec} ($0 \leq U_{dec} \leq 3000V$).

Measurement mode:	**U_{L2} (V)**	**U_{Coll} (V)**	**U_{A2} (V)**
Attenuation + Slow ions	U_{dec} - 100	U_{dec} – 15	U_{dec}
Attenuation + Slow electrons	U_{dec} - 100	U_{dec} + 15	U_{dec}
Beam stopping	U_{dec} - 100	U_{dec}	U_{accel} + 100

3.3.5. Data acquisition

During the measurements, the currents on the first isolated plate (A_1), in the first Faraday cup (FC_1), on the collector, on plate A_2 and in the last Faraday cup (FC_2) are constantly monitored by means of five picoammeters. Throughout the deceleration mode, a high voltage (U_{dec}) is applied to the gas chamber elements and therefore the picoammeters have to be on high voltage ground and their analogue output has to be connected to a home made optical galvanic insulator as shown in Figure 3.13.

The galvanic insulator and the Baratron controller analogue output are connected to a NI USB-6008 12-Bit multifunction data acquisition board which performs the analog/digital (A/D) conversion. A LabVIEW [60] based program was developed during this thesis and used to handle, save and analyze the data. Using this program it is possible to monitor all currents and target gas pressure in real time.

Figure 3.14 shows the developed LabVIEW based program used for data acquisition and analysis. After pressing the button "START" the program begins to store the signal of 4 channels: pressure (P), FC_2 current (I_{FC2}), collector current (I_{coll}) and current for normalization (I_{FC1}). In order to assure a correct current dependency on pressure during the collisions, we normalize the current measured in the FC_2 to the current measured in the FC_1 ($I_{norm} = I_{FC2} / I_{FC1}$). This ratio is displayed in an additional chart. In the main screen it is also possible to set

the voltage range for the NI USB-6008 and the coupling range for the picoammeters. If all settings are correctly defined, the target gas is admitted to the gas chamber. The program loads the stored arrays and plots them as a function of time. In order to analyse all events during the measurement, the plots are divided in "non normalized current" and "normalized current" as shown in Figure 3.15 and 3.16, respectively. The cross sections are evaluated in three extra windows (Figure 3.17, 3.18 and 3.19). The determination of the cross section will be presented in chapter 4.

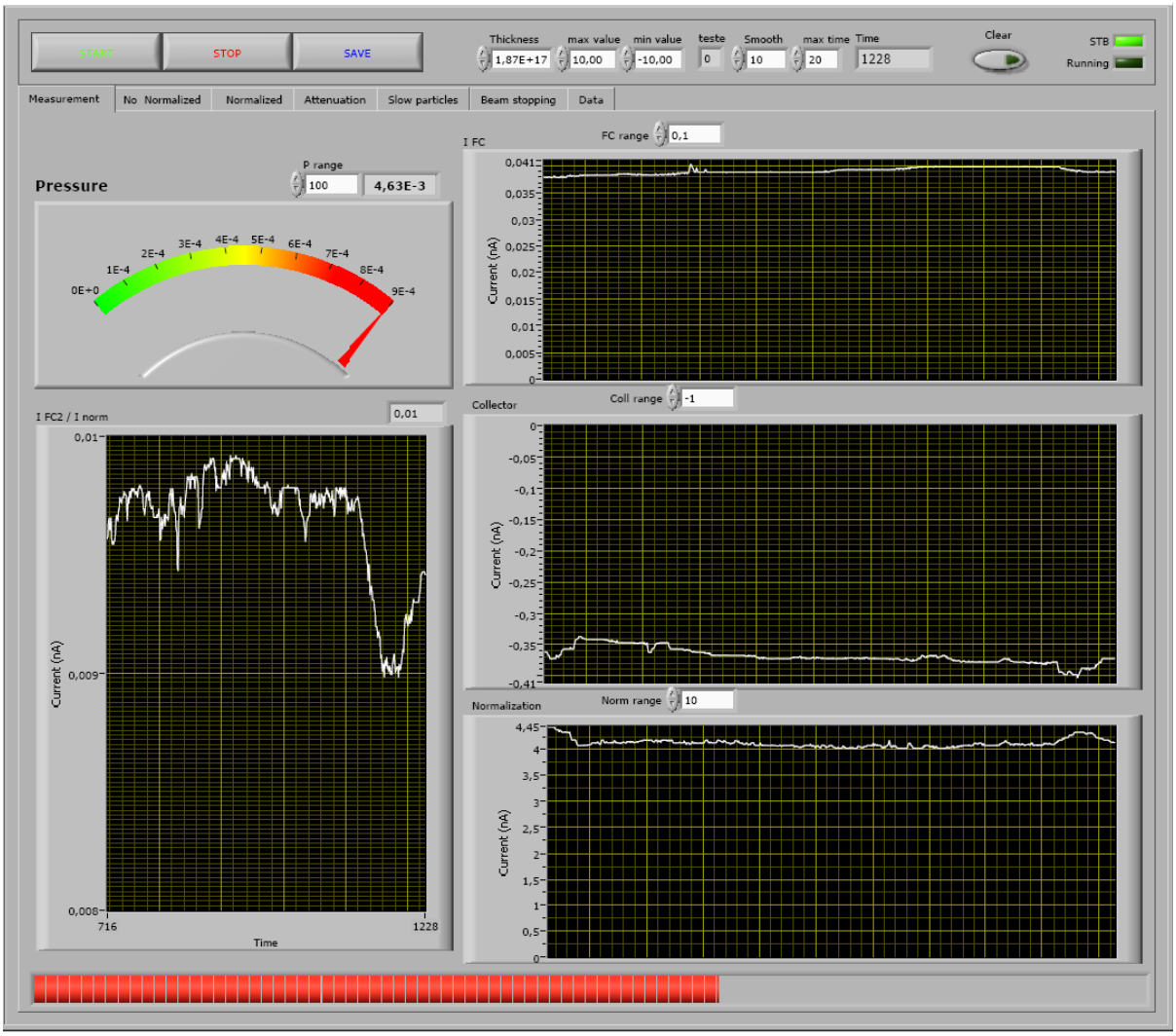

Figure 3.14 – Main-screen of the LabVIEW based program used to acquire and analyse the experimental data.

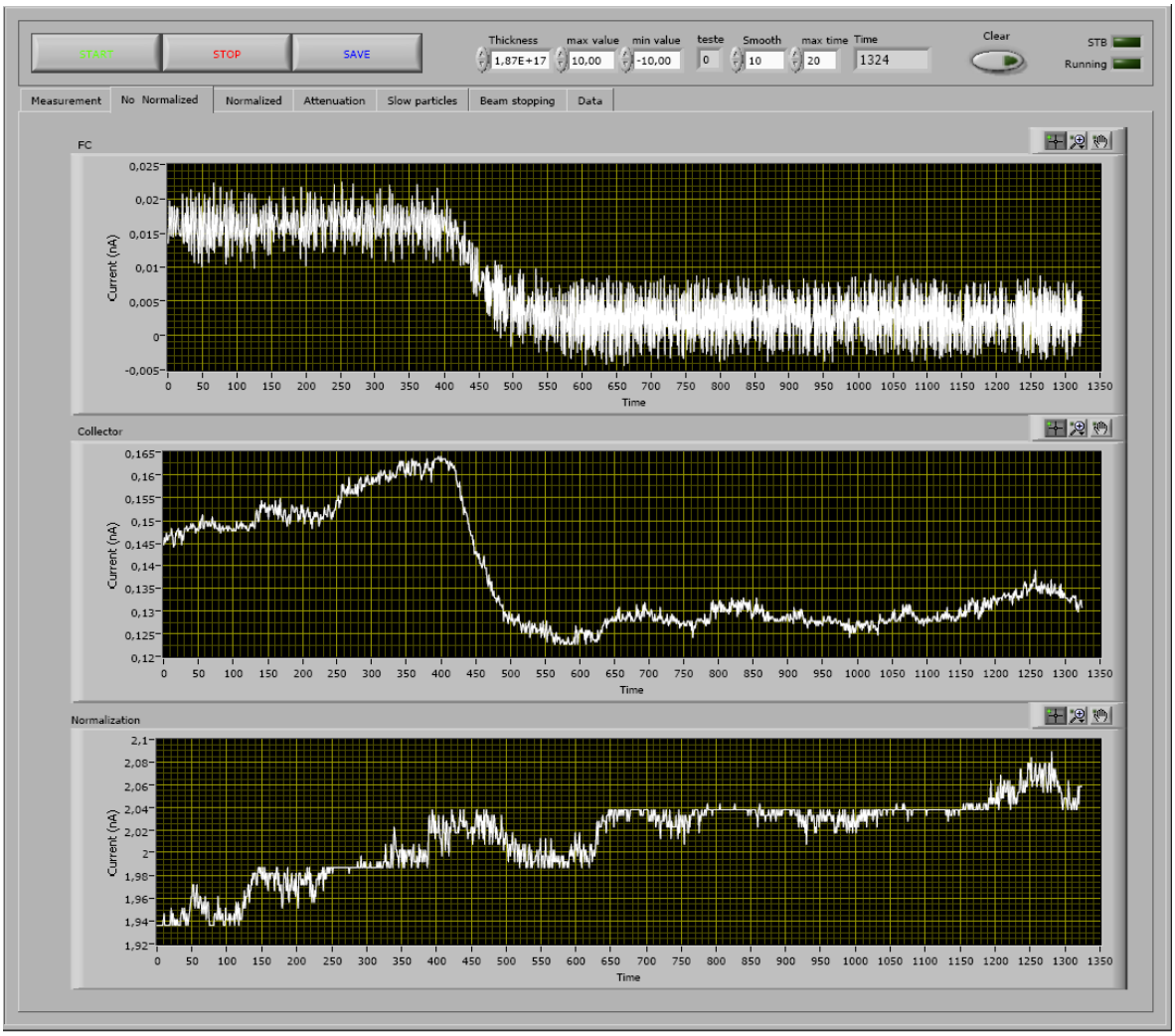

Figure 3.15 – Auxiliary-screens of the LabVIEW based program used to acquire and analyse experimental data. The non normalized currents of first Faraday cup(I_{FC1}), collector (I_{coll}) and second Faraday cup (I_{FC2}) as a function of time are shown for a typical case.

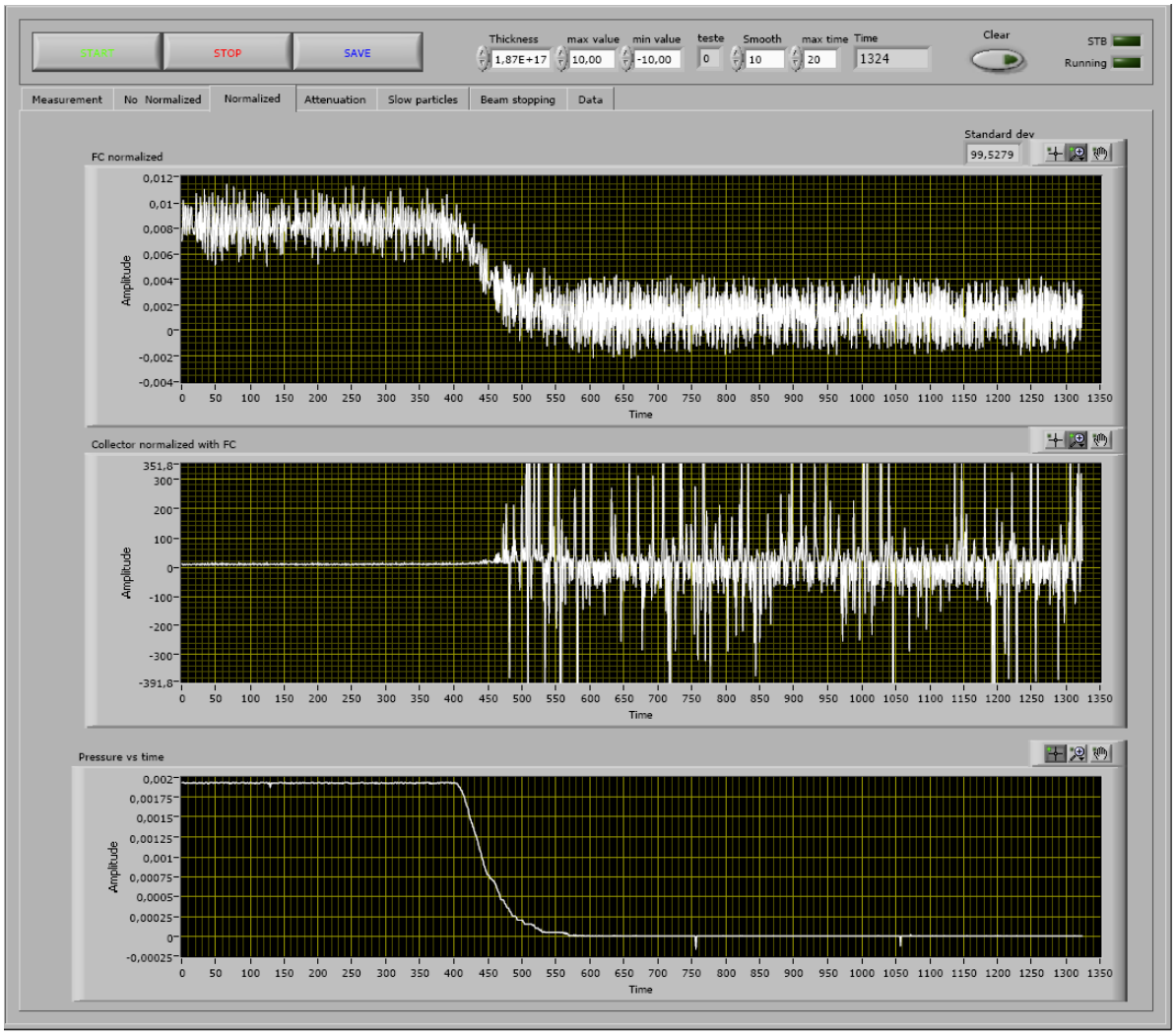

Figure 3.16 – Auxiliary-screens of the LabVIEW based program used to acquire and analyse experimental data. The normalized current I_{FC2}/I_{FC1}, I_{coll}/I_{FC2} and pressure as a function of time are shown.

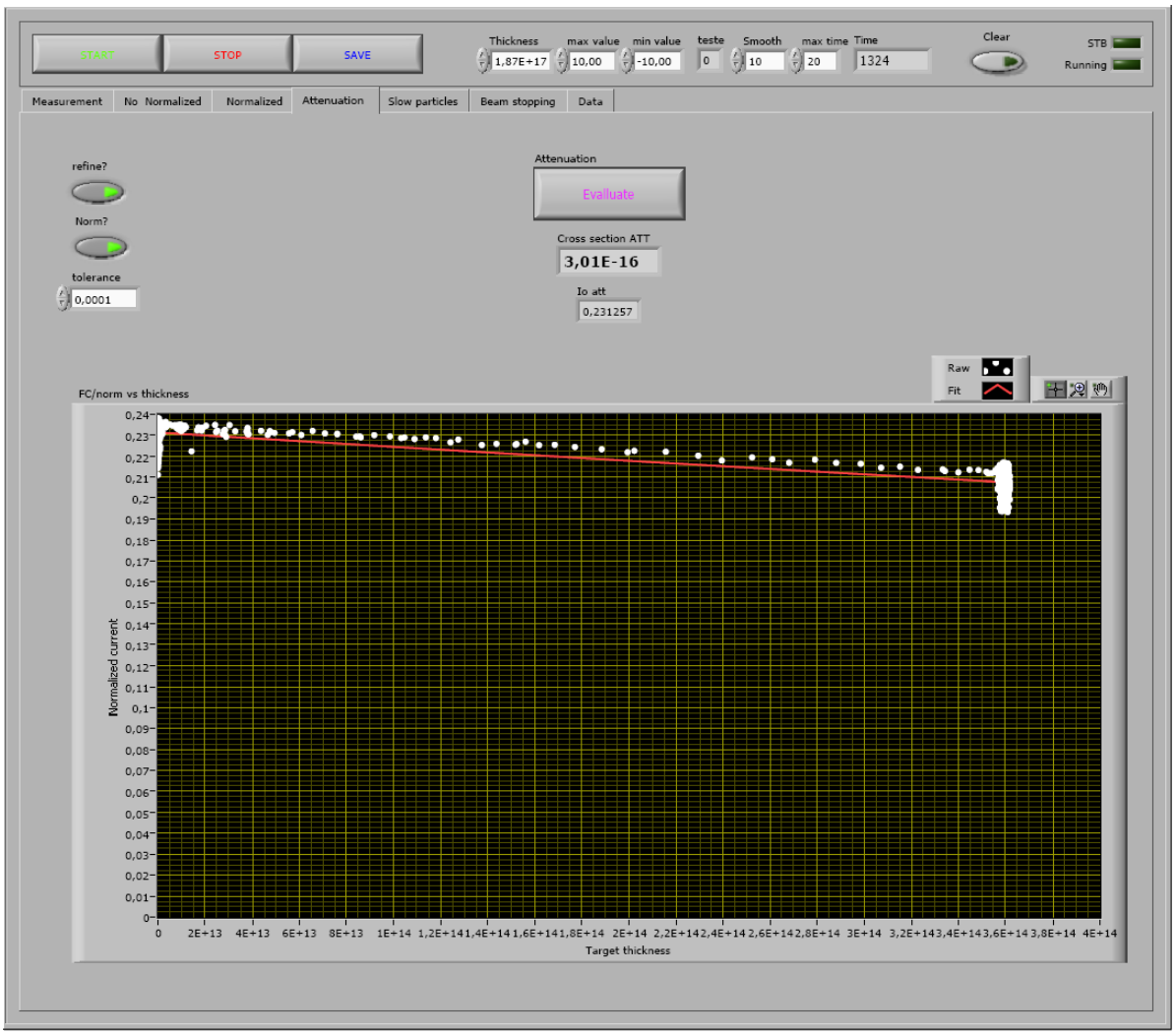

Figure 3.17 – Evaluation-screen of the LabVIEW based program used to acquire and analyse experimental data in the "attenuation mode". The attenuated normalized current as a function of target thickness is shown.

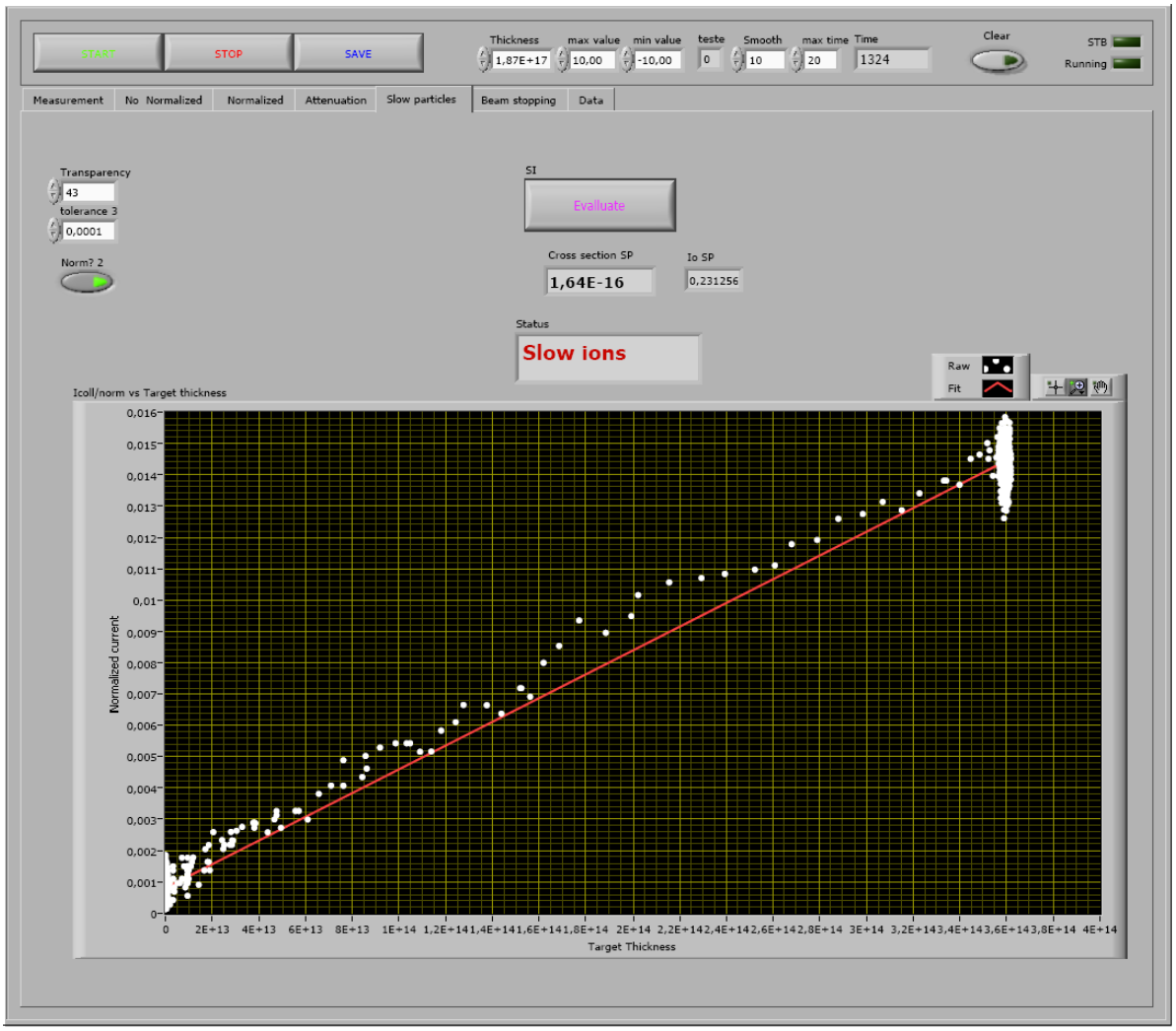

Figure 3.18 – Evaluation-screen of the LabVIEW based program used to acquire and analyse experimental data in the "slow particles collection mode". The slow target ion current (normalized) is shown as a function of target thickness.

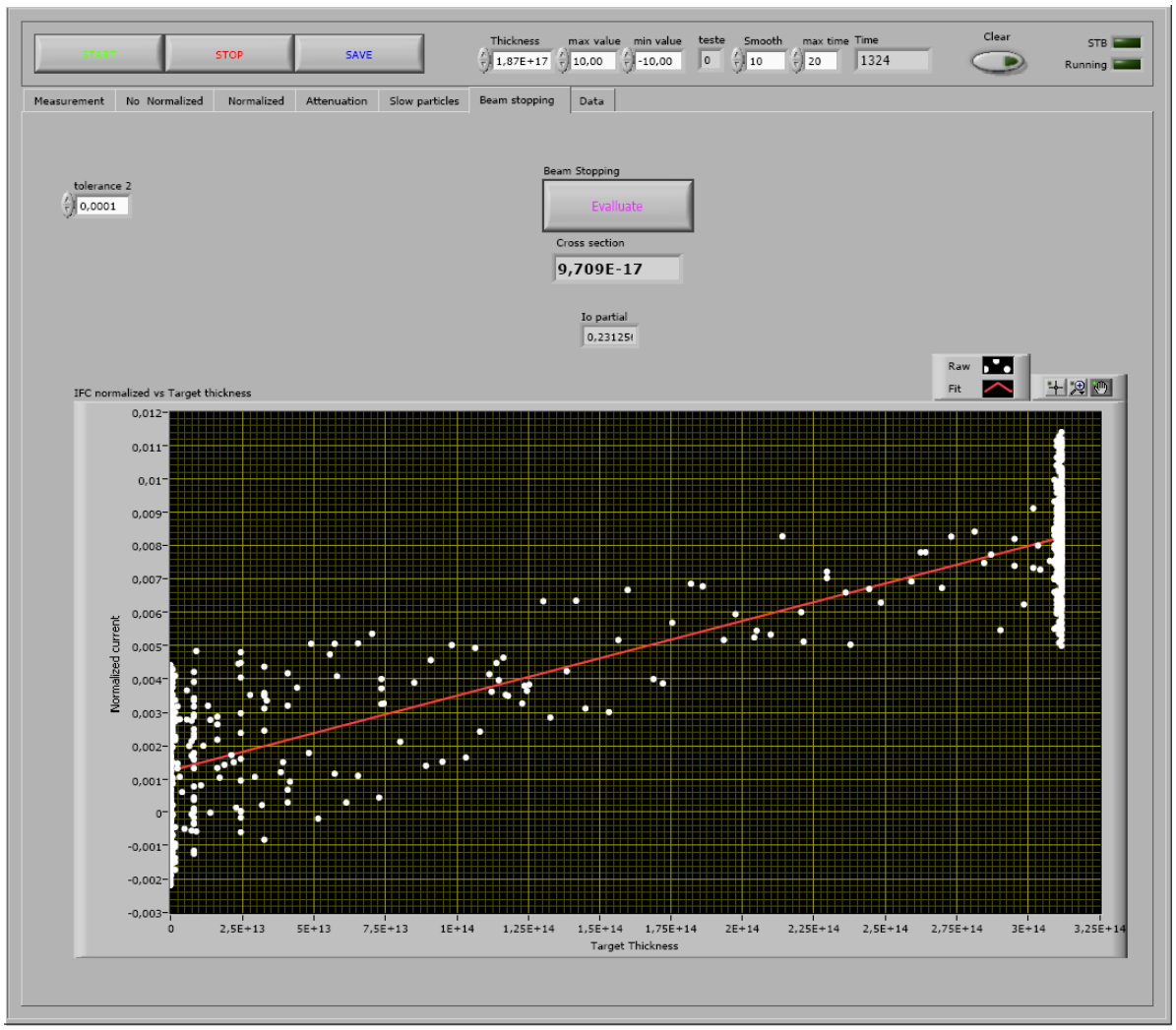

Figure 3.19 – Evaluation-screen of the LabVIEW based program used to acquire and analyse experimental data in the "beam stopping mode". The (normalized) current of produced single charged projectiles as a function of target thickness is shown.

4. Experimental Procedure

Using the experimental setup described in the previous chapter, collision experiments between ions and atoms as well as molecules have been carried out. In order to identify and evaluated the different events, several steps are needed.

In this chapter a description of the experimental procedure will be given. The ion beam impact energy definition is discussed, followed by a description of the different possible methods for cross section evaluation. Finally, the step from data acquisition to data analysis is described.

4.1. Definition of the primary ion beam impact energy

As mentioned in the previous section, the projectile ions are extracted due to the potential U_{accel} (between 1 and 10 kV) applied to the ion source. The initial kinetic energy (E_i) of the primary ion beam with charge q is given by:

$$E_i = q(U_{accel} + U_{plasma}) = qU_{accel}^{eff} \tag{4.1}$$

where U_{plasma} is the plasma potential (typically a few Volts) leading to an effective acceleration potential U_{accel}^{eff}. Considering the extraction of doubly charged ions (q = 2), the impact energy collisions range down to 2000 eV was mainly defined by changing the potential applied to the ion source. To reach lower impact energies, the incoming ion beam was decelerated by means of appropriate potentials applied to the gas cell (see chapter 3.3). The final impact energy is therefore defined by:

$$E_f = q(U_{accel}^{eff} - U_{dec}) \tag{4.2}$$

where U_{dec} is the deceleration potential applied to the gas cell. The final kinetic energy accuracy is mainly determined by the energy spread of the ion beam due to the influence of the plasma potential on extraction region. In our ion source the energy spread is estimated to be about ± 5·q eV. Because there is a protector resistor connecting the power supply to the ion source, the voltage applied to the ion source changes as a function of the plasma current

obeying the Ohmic law. Therefore the actual U_{accell} is always measured by means of a voltage probe.

4.2. Determination of the target thickness

Once the ion beam enters the gas cell the most important parameter that can be changed during collisions is the target gas thickness (π). For a uniform target gas the target thickness is defined as target gas number density (n) times the length inside the gas cell (L) where the collisions take place. Therefore π has dimension of an area. The factor nL is obtained from:

$$\pi = nL \Rightarrow \pi = \frac{pL}{k_B T} \tag{4.3}$$

where p is the gas target pressure, T the absolute thermodynamic temperature and k_B the Boltzmann constant. Assuming that the pressure gradient in the entrance slit of the collision cell is linear, the effective collision path length for attenuated ion beam is the geometrical distance from the entrance slit of the FC_1 to the centre of the suppressor corrected by the FC_1 aperture diameter. In our experiment the target thickness, at room temperature, was obtained from equation (4.3) considering the constant values as:

$$k_B = 1.38 \cdot 10^{-23}\ \text{J/K}$$
$$L = 7.56\ \text{cm}$$
$$T = 293\ \text{K}$$

Since 1 mbar = 10^{-4} J/cm^3, we obtain:

$$\pi = \frac{p[mbar]L[cm]}{k_B\left[\frac{J}{K}\right]T[K]}$$

$$= \frac{10^{-4} \times p\left[\frac{J}{cm^3}\right] \times 7.56[cm]}{1.38 \cdot 10^{-23}\left[\frac{J}{K}\right] \times 293[K]} \tag{4.4}$$

$$= p \times 1.87 \cdot 10^{17}[cm^2]$$

The target thickness accuracy is mainly determined by the instrumental error of the pressure measurement which is $\pm 5 \cdot 10^{-6}$ mbar and the uncertainty of the value of the effective target length L.

4.3. Determination of cross sections

In this work, the charge transfer reactions were identified by analysis of *fast* projectiles and *slow* product ions, and additionally by analysis of slow electrons produced during the collisions. Since the main goal of this thesis deal with doubly charged ions, the equation (1.1) becomes:

$$A^{2+} + B \rightarrow A^{(2-t)+} + \left[B\right]^{r+} + (r-t)e^{-} \tag{4.5}$$

which lead to single (t = 1) and double (t = 2) electron capture (SEC and DEC, respectively). If $t \neq r$ the so-called target transfer ionization (TI) process occurs in which (r - t) electrons are ejected. In the case that t = 0 but $r \neq 0$ a direct ionization (DI) process occurs, which means, the projectile ionizes the target without capture electron. The particle B can be an atom or a molecule. In the latter case, the molecular target can exhibit several exit channels after the collisions, e.g. excited or dissociative states, etc, depending on impact energy and accessible states. The cross sections associated to the identified reactions were obtained by a combination of different techniques, as described in the next sections.

4.3.1. Attenuation method

Let's consider the collision system shown in equation (4.5). A beam of A^{2+} projectile ions, all assumed to have practically the same speed and direction of motion, is incident on a target consisting of particles *B,* which can be either atoms or molecules. Compared to the incident particle speed, the speed of the target particles can be neglected. In traversing the collision region we allow two possible results: (a) a projectile ion passes through the target with its charge unchanged; (b) the projectile ion captures t electron(s) from the target and therefore its final charge state will be (2 - t). Clearly, if the target thickness (π) increases, the probability of case (b) occur increases as well.

Employing the experimental setup described in chapter 3, we obtain the attenuation of the flux of doubly charged ions by measuring the beam intensity (I_{FC}) at the last Faraday cup as a function of target thickness (π). If the target thickness is increased from π to $\pi + d\pi$, the change in the beam intensity (dI_{FC}) in the FC is proportional to the change in thickness $d\pi$ and to the intensity of particles entering target $I_{FC}(\pi)$. That is,

$$dI_{FC} = -\sigma_{att} I_{FC}(\pi) d\pi \tag{4.6}$$

where the proportionality constant, σ_{att}, inserted into equation (4.6) has the dimensions of an area and is usually referred to as the total attenuation cross section. Equation (4.6) can be integrated, leading to

$$I_{FC}(\pi) = I_0 \exp(-\sigma_{att}\pi) \approx I_0 (1 - \sigma_{att}\pi) \tag{4.7}$$

where I_0 is the primary ion current measured in FC_2 without attenuation. The linear approximation in equation (4.7) can only be applied for small current attenuation. To assure single collision the current attenuation has to be less than 10% of the initial current.

Considering the decrease of the doubly charged ion current due to DEC and SEC processes and the related increase of the singly charged ion current due to SEC process as a function of small target thickness π, the total attenuated current from equation (4.7) can be written as:

$$I_{FC}(\pi) \approx \frac{I_0}{2}\left[2 - (2\sigma_{20} + \sigma_{21})\pi\right] \tag{4.8}$$

where σ_{20} and σ_{21} are the DEC and SEC cross sections, respectively.

A typical example of ion beam current attenuation is shown in Figure 4.1 for the symmetric collision system Ar^{2+} on Ar at 1 keV impact energy. It is important to note that the final attenuation in this example (at the highest π values) was much higher than 10% and therefore neither linear approximation nor single collision conditions ($\sigma_{att} * \pi << 1$) are assured.

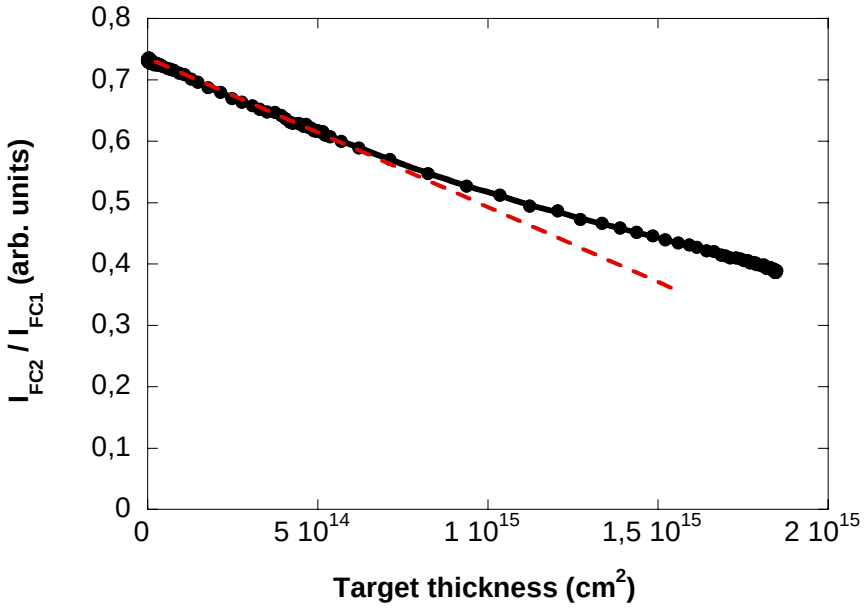

Figure 4.1 – Typical beam current attenuation data, showing the current measured in the last Faraday cup (I_{FC2}) normalized to the incoming current measured in the first Faraday cup (I_{FC1}) for Ar^{2+}-Ar collisions at 1 keV impact energy.

4.3.2. Retarding field measurements (Beam stopping mode)

In order to discriminate SEC and DEC processes (both contributing to beam attenuation, see equation (4.8)) a retarding field technique has been applied. After traversing the target gas cell, fast primary and (charge-exchanged) secondary ions are separated by a retarding field. For an initial ion acceleration voltage U_{accel}^{eff} the primary doubly charged ions will be reflected by a slightly higher retarding potential, while ions that have captured one electrons can only be reflected by a higher potential $U_R \geq 2U_{accel}^{eff}$. For doubly charged primary ions, the SEC cross section can be obtained from the such separated current of fast singly charged ions which increase with target thickness π as

$$I_{sep}(\pi) = \frac{I_0}{2}\left(1 - e^{-\sigma_{21}\pi}\right) \approx \frac{I_0}{2}\sigma_{21}\pi \tag{4.9}$$

By means of SIMION ion trajectory simulations optimum retarding field geometry has been calculated. Figure 4.2 shows a cross section view of the gas chamber where He^{2+} ions (represented by the black lines) are flying through the system with 2 keV kinetic energy and 3° initial opening angle. A positive voltage (U_{A2}) of 1100 V is applied to the retarding ring A_2, while the collision chamber is at deceleration voltage U_{dec} = 900V. The blue lines represent singly charged produced ions (with 2 keV energy) which are not reflected by the 1100 V retarding field.

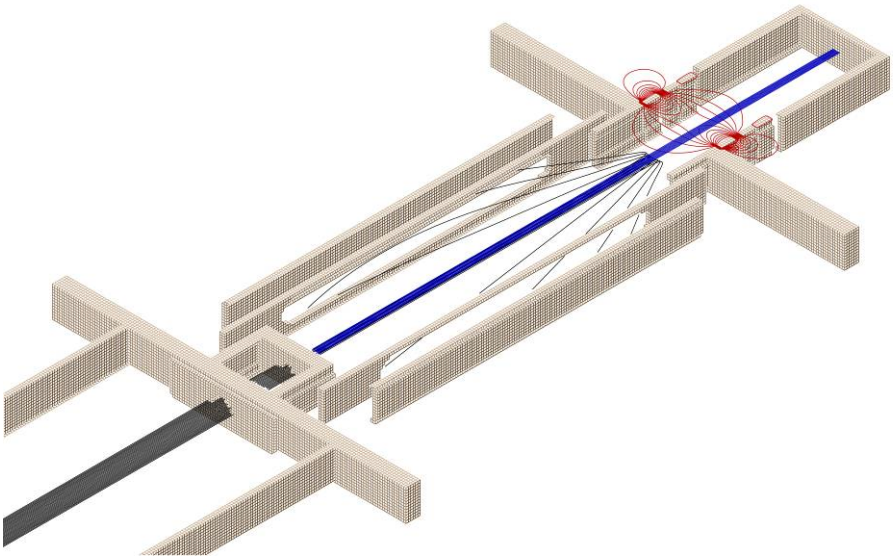

Figure 4.2 – A SIMION simulation of the retarding field method. A doubly charged ion beam with 2 keV kinetic energy (black line) passes through the centre of the system and is reflected by the retarding potential of 1100 V applied to A2. The blue lines represent the singly charged ions produced during SEC collisions.

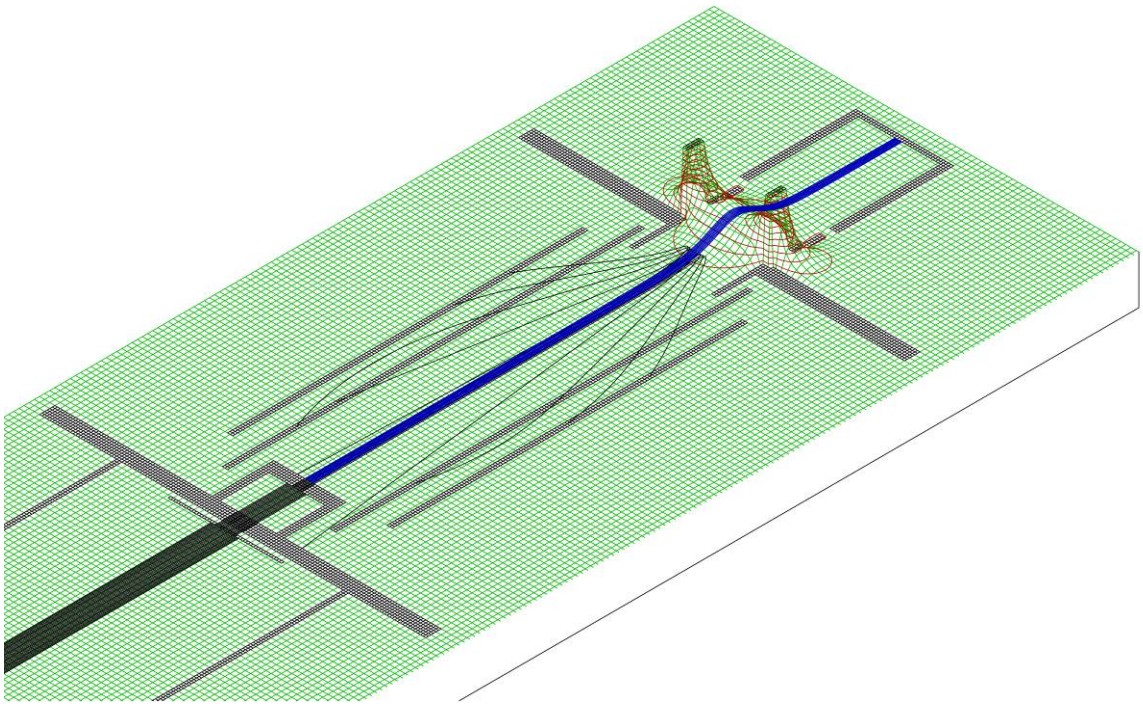

Figure 4.3 – Potential-view of the collision chamber calculated by SIMION. A doubly charged ion beam with 2 keV kinetic energy (black line) passes through the centre of the system and is reflected by the retarding potential of 1100 V applied to A2. The blue lines represent the singly charged ions produced during SEC collisions.

4.3.3. Collection of slow particles

Charged slow secondary particles (target gas ions and electrons) produced in collisions can be collected on a cylindrical electrode surrounding the collision region which is shielded by a highly transparent mesh. To distinguish between slow positive ions and negatively charged electrons the potential applied to the collector with respect to the meshed cylinder is reversed. The next sections describe the procedure for measuring the currents of slow ions and electrons.

4.3.3.1. Measurement of slow ions

The measurement of slow (target gas) ions produced in the collisions is closely related to the attenuation measurement and can be used as a cross-check if charge conservation is considered. The dependence of slow positively charged ions measured on the collector (biased negatively) as function of π is given by

$$I_{coll}^{+}(\pi) = \varepsilon \frac{I_0}{2}\left(1 - e^{-\sigma_+ \pi}\right) \approx \varepsilon \frac{I_0}{2}\sigma_+ \pi \tag{4.10}$$

where σ_+ is the slow ion production cross section and ε the transparency factor ($0 \le \varepsilon \le 1$) of the mesh in front of the collector electrode. This transparency factor is necessary because the meshed cylinder has 6 slits, each with an area of 195 mm^2 (see Figure 3.9). Moreover, the mesh consists of a coiled 0.1 mm molybdenum wire, with 2 mm separating each turn, which gives 98% transparency. Due to this fact the collector can measure just a fraction of the total slow ions produced in the chamber during the collision. The efficiency factor ε can be estimated by considering the local variation of the transparency with the location along the beam axis where the slow target ions are produced and by assuming an isotropic angular distribution of these particles. As a first estimation, we found that 38% of all slow ions produced can be measured on the collector electrode.

A more refined estimate has to take into account the influence of the collector electric field on the mesh transparency. Figure 4.4 shows the meshed cylinder and collector as simulated using SIMION, together with a potential-view calculation. In this simulation the meshed cylinder is kept at ground potential while the collector is biased negatively (-15 V). It is possible to see a non uniform electric field close to the meshed cylinder wall. The influence of this non-uniformity on ε depends on the target ions kinetic recoil energy. We have therefore decided to calibrate the efficiency factor ε by measurements of resonant single electron capture cross section (as shown in chapter 5.2), rather than to calculate it.

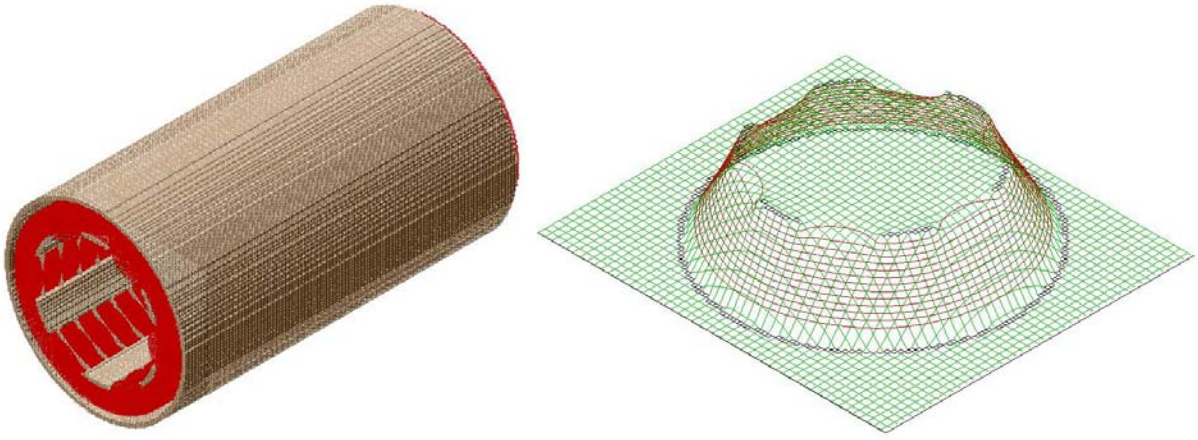

Figure 4.4 – A SIMION simulation of the meshed cylinder and collector electrode system. Left side: a cross section view is shown. Right side: the potential-view is shown. In this simulation the meshed cylinder is kept at ground potential while the collector is biased negatively (-15 V).

4.3.3.2. Measurement of slow electrons

In order to investigate the transfer ionization cross section (σ_{TI}) (process (4.5) with $t \neq r$) the collector is biased positively and consequently electrons ejected during the collisions can be measured. The increase of the slow electron current measured on the collector as a function of target thickness π is given by:

$$I_{coll}^{TI}(\pi) = -\varepsilon' \frac{I_0}{2}\left(1 - e^{-\sigma_{TI}\pi}\right) \approx -\varepsilon' \frac{I_0}{2}\sigma_{TI}\pi \qquad (4.11)$$

here ε' is the transparency factor of the mesh for electrons, which probably differs from ε ($\varepsilon \leq \varepsilon' \leq 1$).

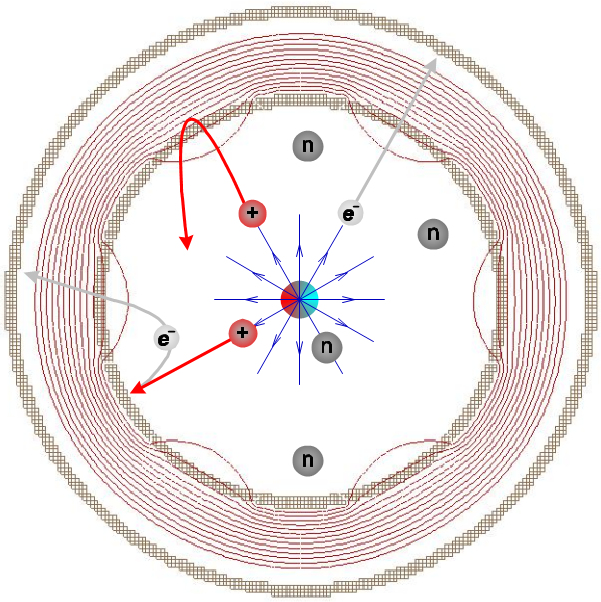

Figure 4.5 – A cross section view of the meshed cylinder and the collector. The ion beam is travelling in the centre of the collision region and perpendicular to the paper. A positive voltage of 15 V is applied to the collector (outer ring) while the mesh (inner ring) is keep at ground potential.

An unavoidable effect of this method is that secondary electrons emitted by particle impact on the meshed cylinder walls are also collected and the measured electron current therefore has to be corrected. Figure 4.5 illustrates this problem by showing a cross section view of the meshed cylinder and the collector. The ion beam is travelling in the centre and perpendicular to the paper. The produced ions and electrons are assumed to spread in all directions. Since a positive voltage is applied to the collector, the electrons produced by the reactions will see the electric field close to the meshed cylinder walls and consequently will be measured in the collector. The produced slow ions do not have enough kinetic energy to

reach the collector and, therefore, will be reflected back to the collision region. If some of these ions bombard the meshed cylinder walls they have a finite probability to release secondary electrons from this surface, which will be accelerated towards the collector.

There are two distinct mechanisms for releasing electrons from a solid under ion bombardment: kinetic electron emission (KE) [63, 64] and potential electron emission (PE) [64-68].

The KE occurs at the expense of the kinetic energy of the projectile. At higher velocities most of the ejected electrons are generated in direct binary collisions of the ions with the valence electrons or with target atoms. The process involves normally three steps: the excitation of the electron, its transport to the surface, and its escape through the surface barrier [65]. KE arises irrespective of the projectile charge only above some impact velocity threshold which, however, is not well defined because of different possible contributions to the apparent electron emission [67].

Using the free electron gas model, the maximum energy transferred in a binary interaction with a light projectile is [63]

$$T_M = 2m_e v(v + v_F), \tag{4.12}$$

where m_e is the mass of the electron, v is the velocity of the ion, and v_F is the Fermi velocity ($v_F \approx 1.98 \cdot 10^6$ m/s for iron). The "classical" threshold velocity for the KE is obtained by setting T_M equal to the work function of the material [63]. For stainless steel, the threshold velocity will be approximately $1.79 \cdot 10^5$ m/s. Corresponding to a kinetic energy of 166 eV/amu. Figure 4.6 shows the current measured on the collector normalized to the current measured in FC_1 as a function of the voltage applied to the collector for Ar^{2+} on Ar collisions at 1 keV impact energy and a fixed pressure in the collision chamber. From these measurements it is possible to see that the recoiling target ions have a maximum kinetic energy of about 5 eV. These measurements have been repeated for the other collisions system studied in this thesis, and show that the maximum kinetic energy never exceeds 10 eV. This is much smaller than the threshold for KE, so electron emission by the KE mechanism remains unlikely.

The other electron emission mechanism is PE which uses the energy released upon the neutralization of an ion [66]. The incident ion can liberate electrons from the metal only if the ground-state recombination energy of the ion exceeds twice the work function of the target. PE yields are reasonably constant for ion velocities below $5 \cdot 10^5$ m/s (corresponding to a kinetic energy of 1.3 keV/amu) and steeply decrease at higher velocities [66, 67]. The first and second ionization energies, I_1 and I_2 respectively, of the target ions and molecules used in

the present work are shown in Table 4.1. It is important to notice that the second ionization potential of H_2 can not be used as a potential energy to cause PE. Therefore two H^+ ions, with 13.6 eV potential energy each, should be used instead. For all ions presented in Table 4.1 the potential energies exceed 2 times the work function of stainless steel ($\varphi \approx 4.4$ eV), so all recoiling ions have in principle enough potential energy to cause electron emission due to the PE mechanism.

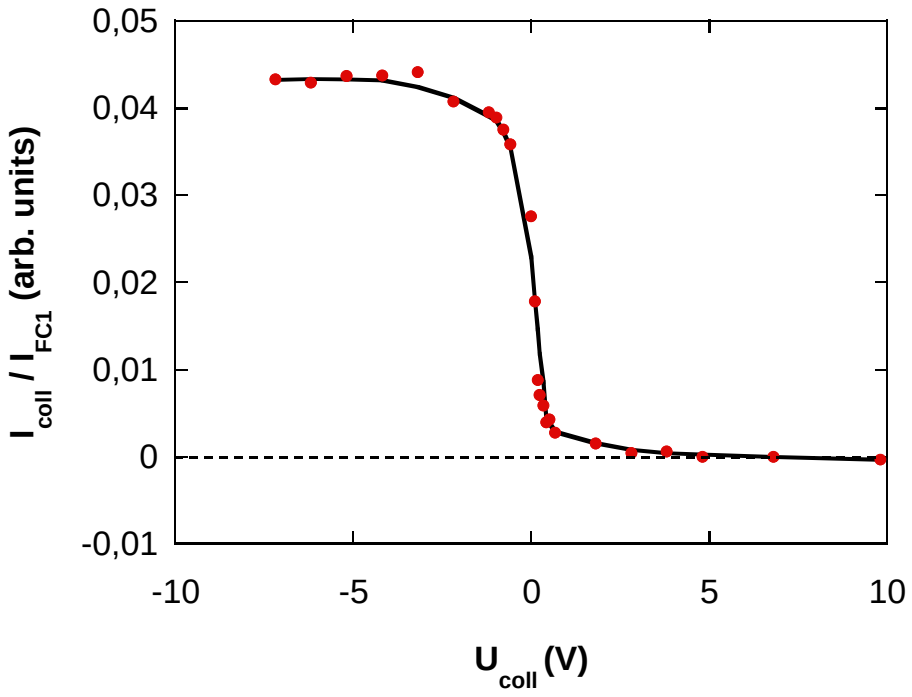

Figure 4.6 – Current of slow target ions (I_{coll}) measured on the collector and normalized to the current (I_{FC2}) measured in the last Faraday cup as a function of the potential between the collector and the meshed cylinder for collisions of incident single charged argon ions (1 keV kinetic energy) on neutral argon gas atoms ($5 \cdot 10^{-4}$ mbar pressure).

Table 4.1 – The first and second ionization energies, I_1 and I_2 respectively, of the atoms and molecules used in the present experiment.

	I_1 (eV)	**I_2 (eV)**
Ar [a]	15.8	27.6
Ne [a]	21.6	41.0
He [a]	24.6	54.4
O_2 [b]	12.1	24.2
H_2 [c]	16.1	31.7
H [c]	13.6	-

Ionization energies: [a] Ref. [69]; [b] Ref. [70]; [c] Ref. [71]

The semiempirical electron yield, i.e. the average number of electrons emitted per incident ion, for a potential energy W_q can at least be estimated by [72]:

$$\gamma = \frac{0.2}{\varepsilon_F}(0.8W_q - 2\varphi), \tag{4.13}$$

where ε_F is the Fermi energy (≈ 11.1 eV for iron), φ is the work function (≈ 4.4 eV for stainless steel). Table 4.2 shows the such estimated PE yield γ for all possible product ions from the targets investigated in this work. The semiempirical formula does not take into account the projectile velocity as well as the gracing impact angle dependency [67] and therefore should be considered as an upper limit for γ.

Table 4.2 – Calculated potential electron yield γ in units of (e^-/ion) for different ions.

	Ar^+	Ar^{2+}	Ne^+	Ne^{2+}	He^+	He^{2+}	O_2^+	O_2^{2+}	H_2^+	H^+
γ	0.07	0.24	0.15	0.43	0.20	0.63	0.02	0.19	0.07	0.04

Using these electron yields it is possible to estimate the contribution of secondary electrons to the electron current measured on the collector. Experimentally, this current is

$$I_{coll}^{-}(\pi) = -\varepsilon' \frac{I_0}{2}\sigma_{-}\pi \tag{4.14}$$

with σ_{-} being the apparent electron production cross section. I_{coll}^{-} has mainly two contributions:

$$I_{coll}^{-}(\pi) = I_{coll}^{TI}(\pi) + I_{coll}^{\gamma}(\pi), \tag{4.15}$$

where $I_{coll}^{TI}(\pi)$ is the current of electrons produced by transfer ionization and $I_{coll}^{\gamma}(\pi)$ is the current of secondary electrons produced by PE measured on the collector. $I_{coll}^{\gamma}(\pi)$ is proportional to the number of singly and doubly charge slow ions produced during the collisions, which means:

$$I_{coll}^{\gamma}(\pi) = \sum_{q=1}^{2} \gamma_q \left(\frac{I_q(\pi)}{q} \right), \tag{4.16}$$

where q is the charge of the slow ions (q = 1,2), I_q is the current of slow ions with charge q and γ_q is the respective potential electron emission yield (Table 4.2). In equation (4.16) we consider that all secondary electron emitted from the meshed cylinder walls to be measured on the collector cylinder, instead of introduce a new efficiency factor (or transparency factor) for secondary PE electrons. Considering single and double electron capture, equation (4.16) can be written as:

$$I_{coll}^{\gamma}(\pi) = \frac{I_0}{2}\left(\gamma_1\sigma_{21} + 2\gamma_2\sigma_{20}\right)\pi\,. \tag{4.17}$$

Finally substituting equations (4.14), (4.11) and (4.17) in equation (4.15) one obtains the following equation for the transfer ionization cross section σ_{TI}:

$$\sigma_{TI} = \sigma_{-} - \frac{1}{\varepsilon'}\left(\gamma_1\sigma_{21} + 2\gamma_2\sigma_{20}\right). \tag{4.18}$$

The values of potential electron yield for singly and doubly charged ions, γ_1 and γ_2 respectively, are obtained from Table 4.2. The use of equation (4.18) for the determination of the TI cross section bears severe limitations:

- The associated error of σ_{TI} will be very large due to the error propagation of SEC and DEC cross sections;
- The values for the PE yield are crude estimates, which might change considerably when impurities or adsorbents on the components are present;
- The transparency factor ε' for electrons most likely differs from the value ε for ions and cannot be determined experimentally in an independent way.

4.4. Data acquisition and cross section evaluation

The developed program for data acquisition described in chapter 3.3.5, is able to evaluate the cross sections for SEC, DEC and TI from equations (4.8), (4.9), (4.14) and (4.18). The data acquisition and cross section evaluation cycle is shown in Figure 4.7. Once kinetic energy and ion beam species are defined and sufficient beam intensity (typically 10 nA) is measured in the last Faraday cup, the experiment can begin. The first step is to monitor and record the currents and pressure measured in the apparatus. Then the programme will check whether these values (normalized and not normalized currents, as well as pressure) are sufficiently stable. The maximum accepted standard deviation is 1%. After that, the target pressure is varied and the total attenuation is measured. In order to assure single collisions a maximum attenuation value of less than 10% was accepted. After these first checks, the cross section evaluations are carried out for three different modes: a) collector biased negatively: attenuation and slow ions, b) collector biased positively: attenuation and slow electrons, c) beam stopping mode: A_2 biased with the same potential as the ion source (this method is just applicable for incident doubly charged ions).

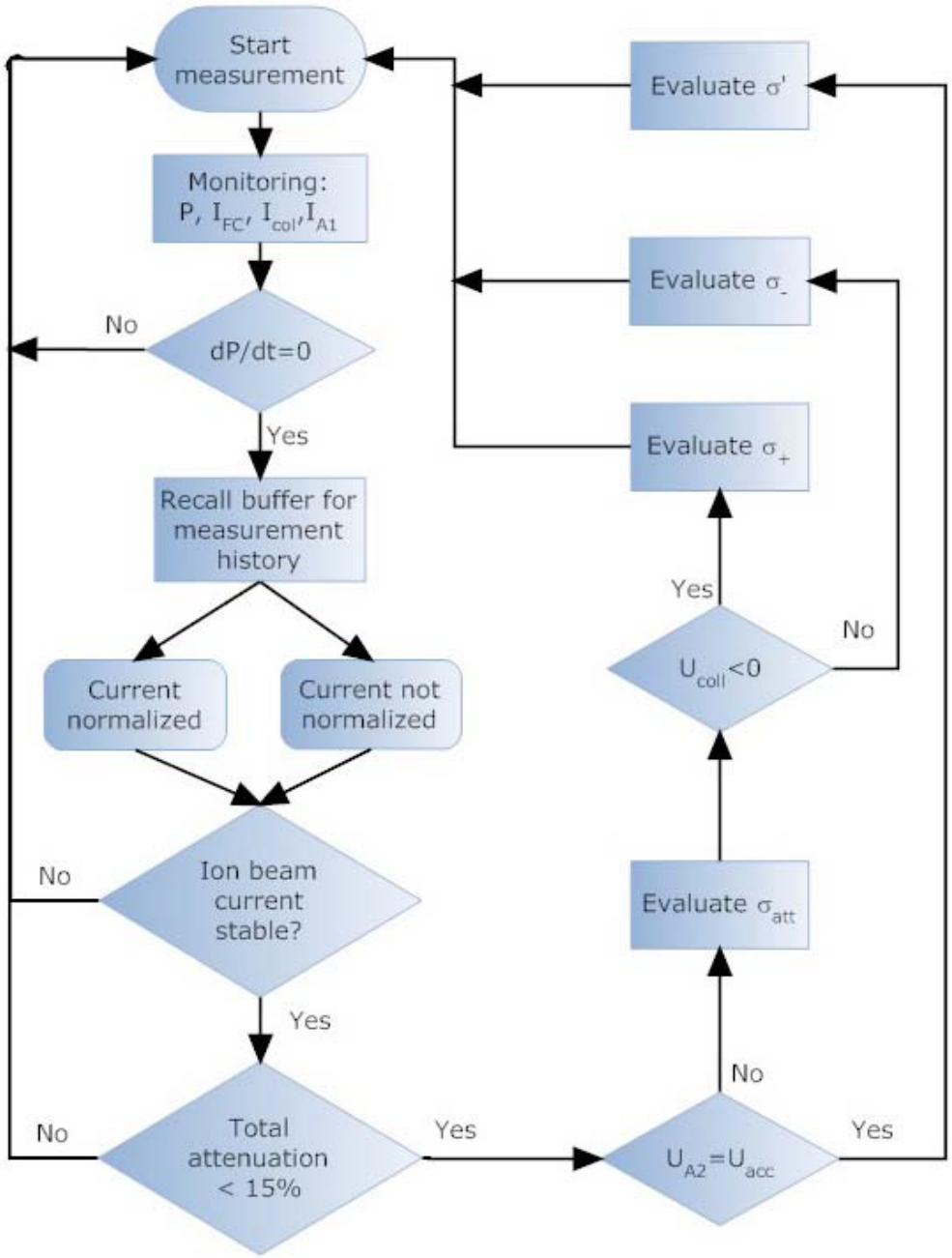

Figure 4.7 – Schematic representation of the data acquisition and cross section evaluation procedure.

5. Results and Discussion

5.1. Experimental error sources

In this work, the statistical uncertainty of the measured cross section values ranges typically from 0.3 to 8.3 %. The cross sections measurement have been successively repeated, until the data reached a determined standard deviation of less than 6%. For the total error estimates, several other factors are also taken into account: (i) target thickness uncertanty, (ii) analogue digital conversion precision, (iii) temperature variation of the target gas, (iv) target gas impurities. These are estimated to be 5, 2, 6 and 1 %, respectively. The total experimental error of the absolute cross sections can be obtained through the square root of the quadratic sum of these uncertainties, and was therefore of the order of 12%.

5.2. Resonant single electron capture

In order to check the reliability of the apparatus and applied experimental procedures and to calibrate the transparency factor ε (see section 4.3.3.1), the resonant single electron capture processes,

$$X^{+}_{fast} + X_{slow} \xrightarrow{\sigma_{10}} X_{fast} + X^{+}_{Slow} \tag{5.1}$$

for X = Ar, Ne and He have been measured. For these processes the attenuation of the incoming ion beam as function of target gas density (equation (4.7)) is given by:

$$I(\pi) = I_0 \exp(-\sigma_{10}\pi) \approx I_0 \left(1 - \sigma_{10}\pi\right), \tag{5.2}$$

where σ_{10} is the single electron capture cross section and I_0 the current in the last Faraday cup without attenuation. On the other hand, the current of slow ion current, as measured on the collector, increases nearly linearly as a function of the target thickiness:

$$I_{coll}(\pi) \approx I_0 \varepsilon \sigma_{10} \pi \tag{5.3}$$

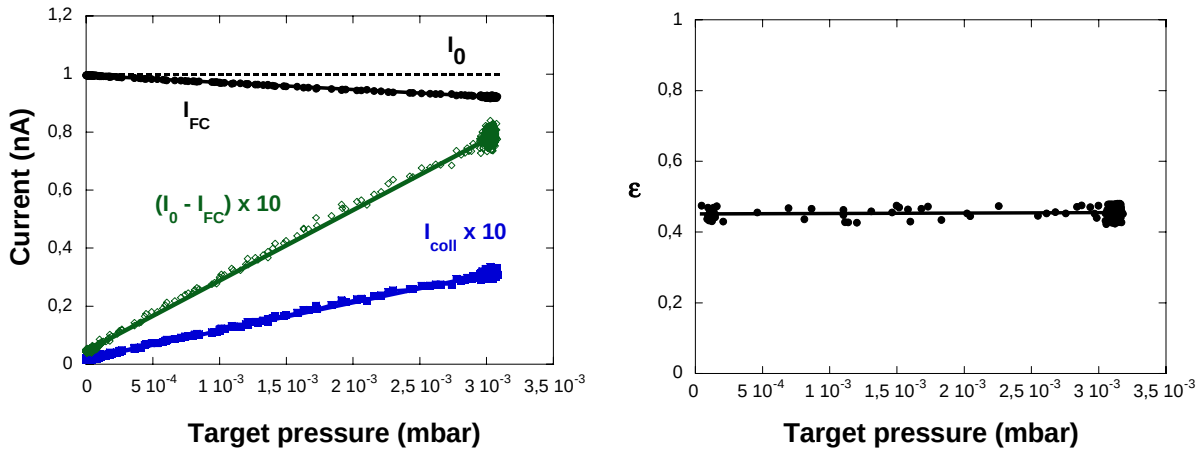

Figure 5.1 – Left window – current measured in the last Faraday cup (I_{FC}), slow ion current measured on the collector (coll) and value ($I_0 - I_{FC}(\pi)$) as a function of target pressure (related to target thickness) for Ar^+–Ar collisions at 1 keV impact energy. The two last currents were multiplied by 10 for better comparison. Right window – efficiency factor ε for slow ion collection as derived from equation (5.4) as a function of target pressure for Ar^+–Ar collision at 1 keV impact energy.

From equations (5.2) and (5.3) it is obvious that both techniques should provide the same cross section, since there is just one reaction channel. In this case, every charge exchanged fast ion should give rise to a corresponding slow ion. From this measurement it is, therefore, possible to calibrate the factor ε discussed in chapter 4.3.3. An example of such type of measurement is shown in the left window of Figure 5.1 for the symmetric system $Ar^+_{fast} + Ar_{slow} \rightarrow Ar_{fast} + Ar^+_{slow}$ at 1 keV impact energy. The green diamonds give the value ($I_0 - I_{FC}(\pi)$) which should be equal to the total current of slow ions produced in the collisions if all of them would be collected. It is possible to see that the collector electrode just receives a fraction ε of these total slow ions. Therefore, the efficiency (transparency) factor ε is obtained from the ration

$$\varepsilon = \frac{I_{coll}(\pi)}{I_0 - I_{FC}(\pi)}. \qquad (5.4)$$

Figure 5.1 (right) shows that the transparency factor ε is independent of the target gas pressure (as expected). The value was found to be 0.46 ± 0.02, in reasonable agreement with a estimated value of 0.38 calculated from geometrical considerations (c.f. 4.3.3.1)

The reliability of this determination of the efficiency factor ε was further checked in measurement of Ar^+ – Ar, Ne^+ – Ne and He^+ – He collisions at different impact energies. Results are shown in Figure 5.2, 5.3 and 5.4, respectively. In all cases both techniques provide equal results (within our experimental uncertainties) when using the measured efficiency

factor $\varepsilon = 0.46$. Moreover, our data were found to be in good agreement with already published theoretical and experimental results. Additionally, we have performed EOBM cross section calculation for the resonant collision system in order to check the new developed code (see section 2.5). The calculated SEC cross sections were performed using the first ionization potential given in Table 4.1. The results were found to be in a reasonable well agreement with the values here presented.

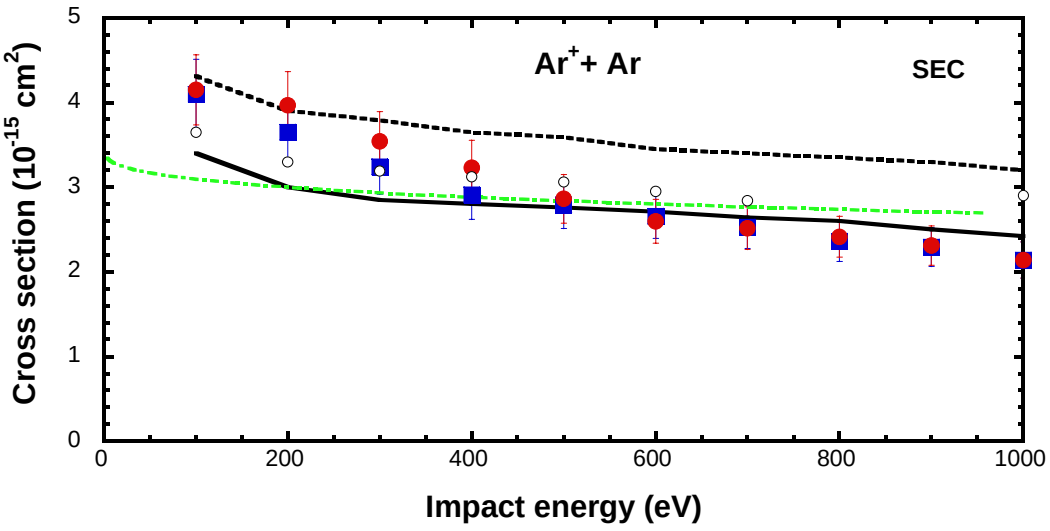

Figure 5.2 – Resonant SEC cross section for Ar^+ + Ar as a function of impact energy. Full squares – ion attenuation technique from this work, full circles – slow ion collection technique from this work, full line – theory of Copeland at al. [73], dotted line – theory of Sakabe at al. [74], open circles – experimental results of Hayden at al. [75], green dashed line – EOBM calculation from this work (c.f. chapter 2.5.2).

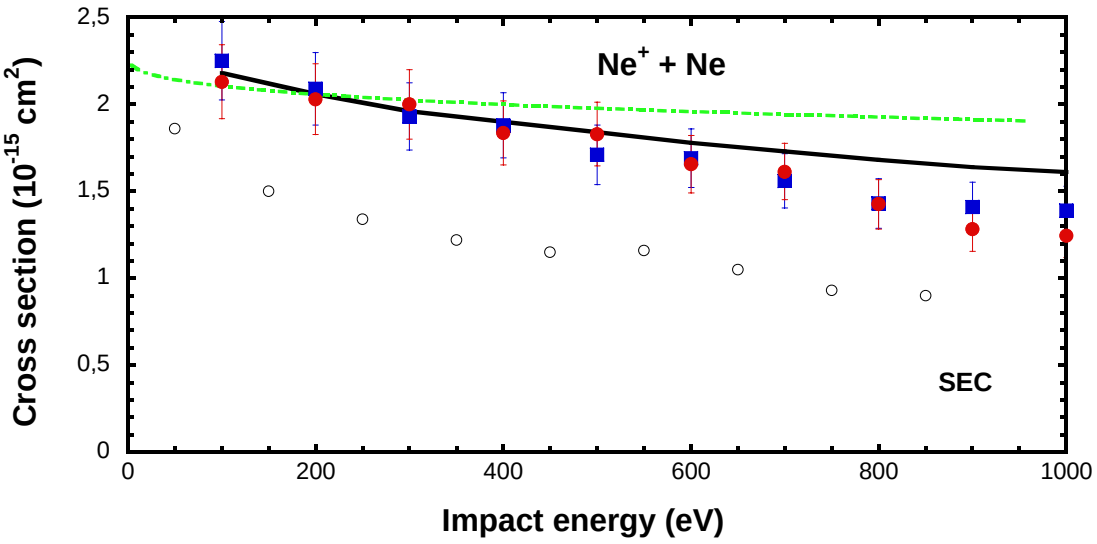

Figure 5.3 – Resonant SEC cross section for Ne^+ + Ne as a function of impact energy. Full squares – ion attenuation technique from this work, full circles – slow ion collection technique from this work, full line – theory of Sakabe et al. [74], open circles – experimental results of Dillon et al. [76] , green dashed line – EOBM calculation from this work (c.f. chapter 2.5.2).

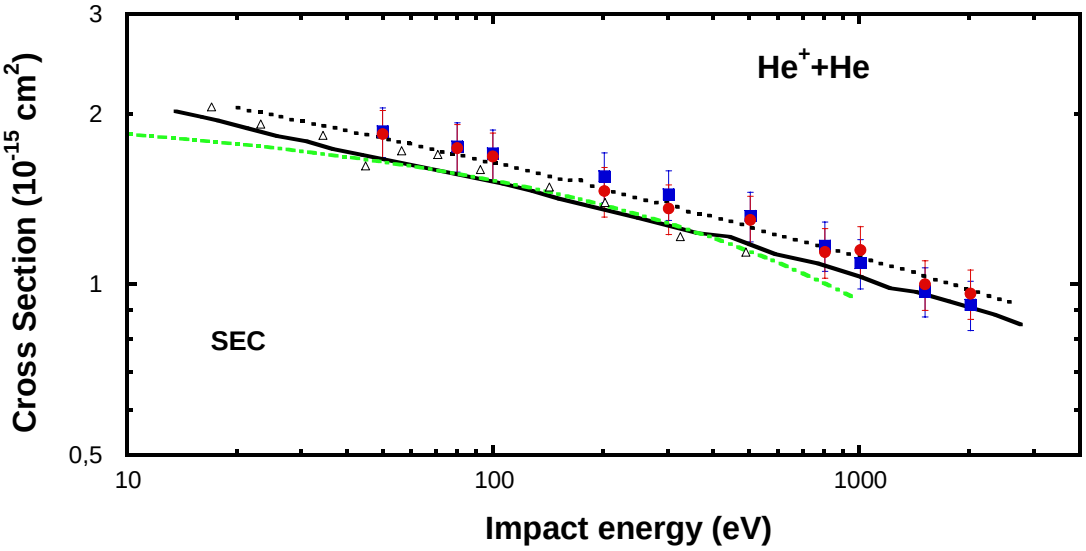

Figure 5.4 – Resonant SEC cross section for He^+ + He as a function of impact energy. Full squares – ion attenuation method technique from this work, full circles – slow ion collection technique from this work, full line – theory of Sakabe et al. [74], dotted line – theory of Copeland et al [73], open triangles – experimental results of Hinds et al [77] , green dashed line – EOBM calculation from this work (c.f. chapter 2.5.2).

5.2.1. Discussion of resonant charge-transfer

A general feature of the resonant charge-exchange cross section in singly charged ion– atom– collisions is that it decreases with increasing energy, while non-resonant charge-exchange cross sections at first increase to a broad maximum and then decrease with further increasing energy [78]. Calculations of symmetric resonant charge-exchange cross sections are generally carried out by studying the process in three velocity ranges. The present work lies in the "intermediate" to "low" velocity range ($v < 10^8$ cm/s). In this impact energy range the cross section for symmetric resonant charge exchange decreases with increasing impact velocity v as [79]:

$$\sigma(v)^{\frac{1}{2}} = a - b \ln v \tag{5.5}$$

where a and b are constants. Table 5.1 shows the values of the constants a and b obtained by fitting equation (5.5) to the resonant SEC cross sections obtained for the collision system Ar^+ – Ar, Ne^+ – Ne and He^+ – He using the two methods of beam attenuation and slow ion collection. The results of this fits are shown in Figure 5.5.

Table 5.1 – Values of the constants *a* and *b* obtained from the fitting of the resonant single electron capture cross sections using equation (5.5).

	Attenuation method		Slow ions collection	
	a	*b*	*a*	*b*
Ar	2.112	0.482	2.175	0.520
Ne	1.669	0.289	1.651	0.283
He	1.583	0.218	1.552	0.204

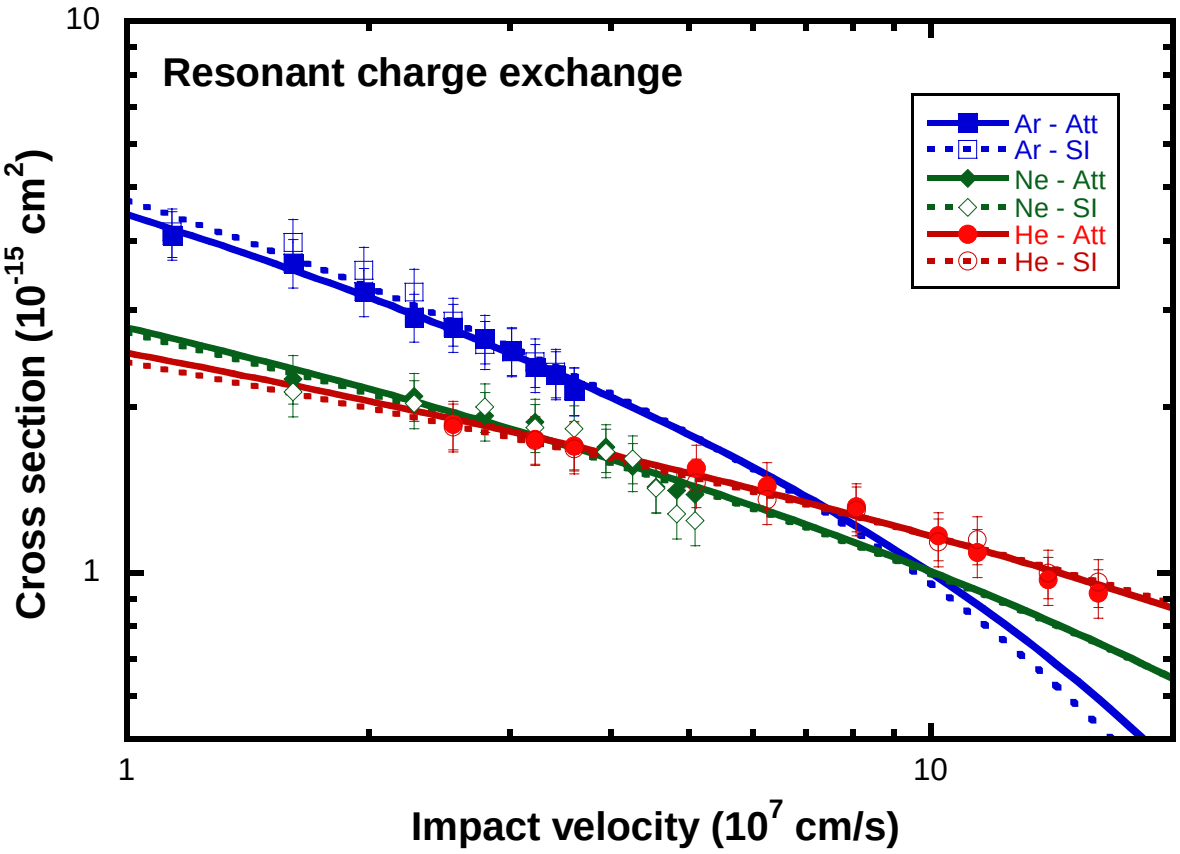

Figure 5.5 – Resonant SEC cross section as function of impact velocity. The cross sections for Ar, Ne and He singly charged ions collisions with their respective neutral gases are fitted accordantly to equation (5.5).

5.3. SEC and DEC for symmetric systems

Single and double electron capture and transfer ionization cross sections for Ar^{2+}, Ne^{2+} and He^{2+} ions in their respective neutral gases were measured in the collision energy range up to 10 keV. The statistical accuracy for these cross sections for consecutive measurements is typically about 6%. Because the cross sections for double electron capture are obtained by a combination of equations (4.8) and (4.9) the error propagation leads to a somewhat reduced accuracy for the DEC cross section values as compared to the SEC values. In addition, the cross section for electron production was derived according to the procedure outlined in section 4.3. In the evaluation of equation (4.18) the effective transparency factor $\varepsilon' = 1$ was used and the error propagation leads to uncertainties, which varied for the different collision system and averaged 50 % of the absolute values in the worst case. Cocke et al [80] have reported that transfer ionization (TI) is the dominant channel at low impact energies, while direct ionization (DI, i.e. the target is ionized at the expense of only the projectile's kinetic energy) can be neglected. Therefore, in this work we consider that the electron ejection from the target is mainly due to TI.

In addition, we have performed LZ and EOBM calculations as outlined in sections 2.4 and 2.5, respectively. We have calculated the SEC cross sections by Landau-Zener for the available exothermic channel and the resulting energy defect (ΔE), crossing radius (R_c) and interaction matrix elements (H_{12}) are presented and the theoretical results are compared to the experimental values (and theoretical results, when available). Furthermore, we have calculated the SEC and DEC cross sections by the EOB. The values for the free parameters of the model were fixed at $\alpha = 2$ and $f_T = 2$. Initially, a variation of the parameter α has been performed in order to find a value for the minimum distance for electron capture (R_m) as realistic as possible based on the avoid crossing distance, in cases where the adiabatic curves were available. In the literature [54] it has been shown that a better agreement with experimental values is achieved for $1 < \alpha < 2$. The theoretical results of SEC and DEC cross section by EOBM are discussed and compared to the experimental data (and theoretical results, when available).

5.3.1. Ar^{2+} on Ar

Collisions of Ar^{2+} on Ar were performed in the impact energy range from 50 eV to 4 keV. This system has been extensively investigated in the literature and by means of translational energy spectroscopy several exit channels were found to be of importance for low impact energy [81, 82]. These different reaction channels in the symmetric collision system Ar^{2+} – Ar are summarised in Table 5.2. The system has just one exothermic reaction with an energy defect of 11.9 eV, all other reactions are endothermic with ΔE values between -1.6 and -20.9 eV. The smallest ΔE value leads to an excited Ar^{+*} projectile ion formed in the ^2S or ^2P state.

Table 5.2 – Individual reactions channels for charge transfer of $Ar^{2+}(3s^23p^4)$ + Ar $(3s^23p^6)$ collisions [81, 82].

	Reaction products	I_2 (eV)	I_1 (eV)	ΔE (eV)	R_c (a_o)	H_{12} (a.u.)
a)	$Ar^+(3s^2\,3p^5,\,^2P) + Ar^+(3s^2\,3p^5,\,^2P)$	27.63	15.76	+11.87	2.29	0.187
b)	$Ar^{+*}(3s\,3p^6,\,^2S) + Ar^+(3s^2\,3p^5,\,^2P)$	14.15	15.76	-1.61	-	-
c)	$Ar^{+*}(3s^2\,3p^4\,3d) + Ar^+(3s^2\,3p^5,\,^2P)$	11.23	15.76	-4.53	-	-
d)	$Ar^+(3s^2\,3p^5,\,^2P) + Ar^{+*}(3s\,3p^6,\,^2S)$	27.63	29.24	-1.61	-	-
e)	$Ar^{+*}(3s\,3p^6,\,^2S) + Ar^{+*}(3s\,3p^6,\,^2S)$	14.15	29.24	-15.09	-	-
f)	$Ar^{+*}(3s^2\,3p^4\,3d) + Ar^{+*}(3s\,3p^6,\,^2S)$	11.23	29.24	-18.01	-	-
g)	$Ar^+(3s^2\,3p^5,\,^2P) + Ar^{+*}(3s^2\,3p^4\,3d)$	27.63	32.16	-4.53	-	-
h)	$Ar^{+*}(3s\,3p^6,\,^2S) + Ar^{+*}(3s^2\,3p^4\,3d)$	14.15	32.16	-18.01	-	-
i)	$Ar^{+*}(3s^2\,3p^4\,3d) + Ar^{+*}(3s^2\,3p^4\,3d)$	11.23	32.16	-20.93	-	-
j)	$Ar^{2+}(3s^2\,3p^4) + Ar^+ + e^-$	0	15.76	-15.76	-	-
l)	Ar $(3s^23p^6) + Ar^{2+}(3s^23p^4)$	43.39	43.39	0	-	-

The measured SEC and DEC cross sections (σ_{21} and σ_{20}, respectively) are plotted as a function of impact energy in comparison with previously published data in Figure 5.6. In the collision energies regime applied in our measurement, two-electron capture processes take place predominantly. The DEC cross section (σ_{20}) increases with decreasing impact energy. The explanation of this behaviour is straightforward, since the total internal energy before the collision is the same as that after the collision (Table 5.2 process l). Such events are called symmetric resonant DEC processes and there is generally a high probability for them to occur. The present values are in a good agreement with experimental results by Okuno [83] both in the energy dependence and in the absolute magnitude. The SEC cross sections from the literature, however, scatter significantly. Our measured SEC cross section agree with these previous measurements regarding the overall trend and the order of magnitude. Interestingly the single electron capture does exceed the double electron capture, even at the higher impact

energies used. The differences among the various experimental results may be caused by a different amount of highly excited metastable Ar^{2+} projectile ions present in the beam. For such metastable states curve crossings are available in a favourable region of inter-nuclear distances yielding a small energy defect and therefore higher cross sections, as has been pointed out by [82]. The binding energy levels of ground state different excited metastable Ar^{2+} projectile ions are compared in Figure 5.8.

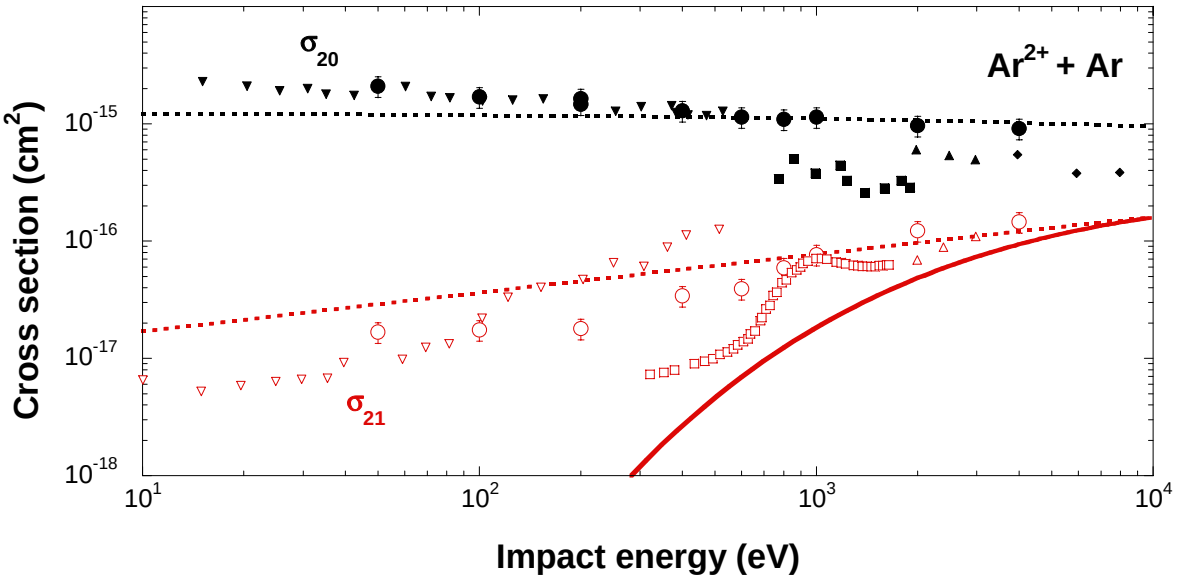

Figure 5.6 – SEC and DEC cross section for Ar^{2+}–Ar collisions as a function of impact energy. Double electron capture is represented by full black symbols, single electron capture by open red symbols. Circles – this work, squares – experimental results by Huber [81], triangles – experimental results by Cosby et al [84], inverted triangles – experimental results by Okuno [83], diamonds – experimental results by Kaneko et al [85]. Theoretical results: dashed black line – DEC cross section by EOBM from this work, dashed red line – SEC cross sections by EOBM from this work, full red line – SEC by LZ calculation from this work.

Because of the complete lack of systematic theoretical work for this collision system, we have performed LZ and EOBM calculations as outlined in sections 2.4 and 2.5, respectively. The results of these calculations are shown in Figure 5.6 in comparison with the experimental values.

The calculated SEC cross sections by Landau-Zener for the exothermic channel (Table 5.2) has a maximum value of about 10^{-16} cm^2 which fairly agrees with the values up to 1 keV impact energy. For lower impact energies, however, the model predicts much smaller values for this exit channel. More probable reactions in this energy range are those that have the smallest ΔE, i.e. processes b), c), d) and g) from Table 5.2. Because these reactions are endothermic, the cross section cannot be estimated by the Landau-Zener method.

Therefore SEC and DEC cross sections have been calculated by the EOB model using the respective ionization potentials listed in Table 5.2. Our EOB calculations result in R_m = 3.77 a.u. and predict a DEC cross section almost independent of impact energy with the maximum value of about $1.1 \cdot 10^{-15}$ cm^2 which is in reasonable agreement with the experimental values. The calculated SEC cross sections have the correct order of magnitude as our experimental values and reproduce their impact energy dependence very well, approaching the maximum value predicted by LZ model at around 10 keV impact energy.

In addition, the cross section for electron production was derived according to the procedure outlined in section 4.3. Figure 5.7 shows the electron production cross section values obtained in this work. Our TI cross sections are small for low impact energies but strongly increase with increasing the impact energy, however, remain in all cases well below the values for SEC and DEC. To our knowledge, there is no previous data on transfer ionization in the present energy range as well as for higher impact energies.

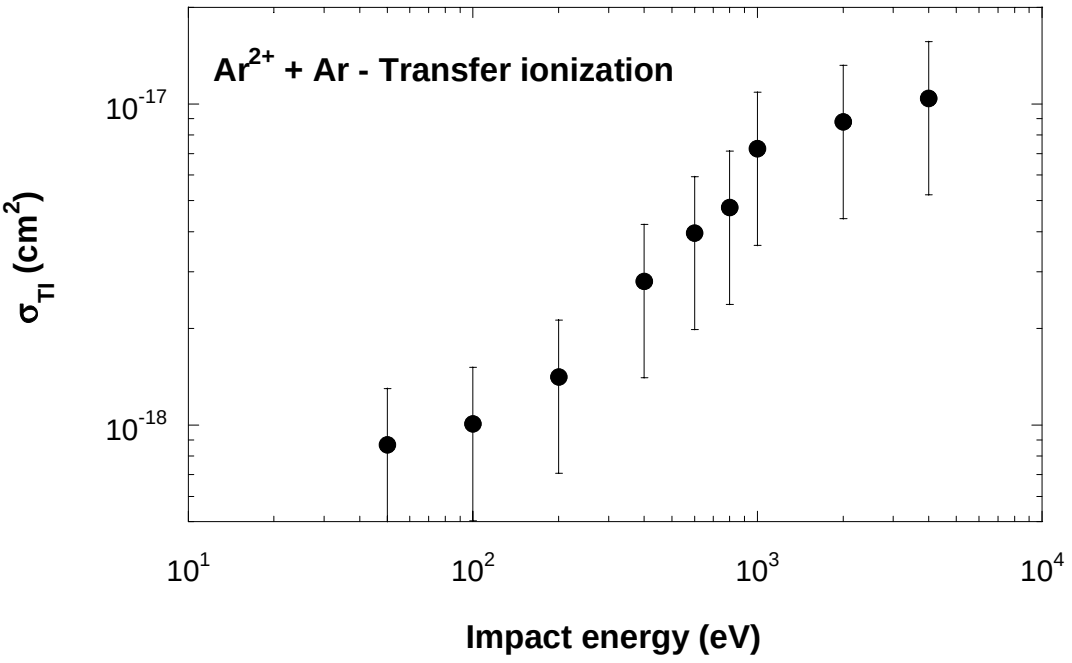

Figure 5.7 – Transfer ionization (TI) cross section as a function of impact energy for the collision system Ar^{2+} + Ar.

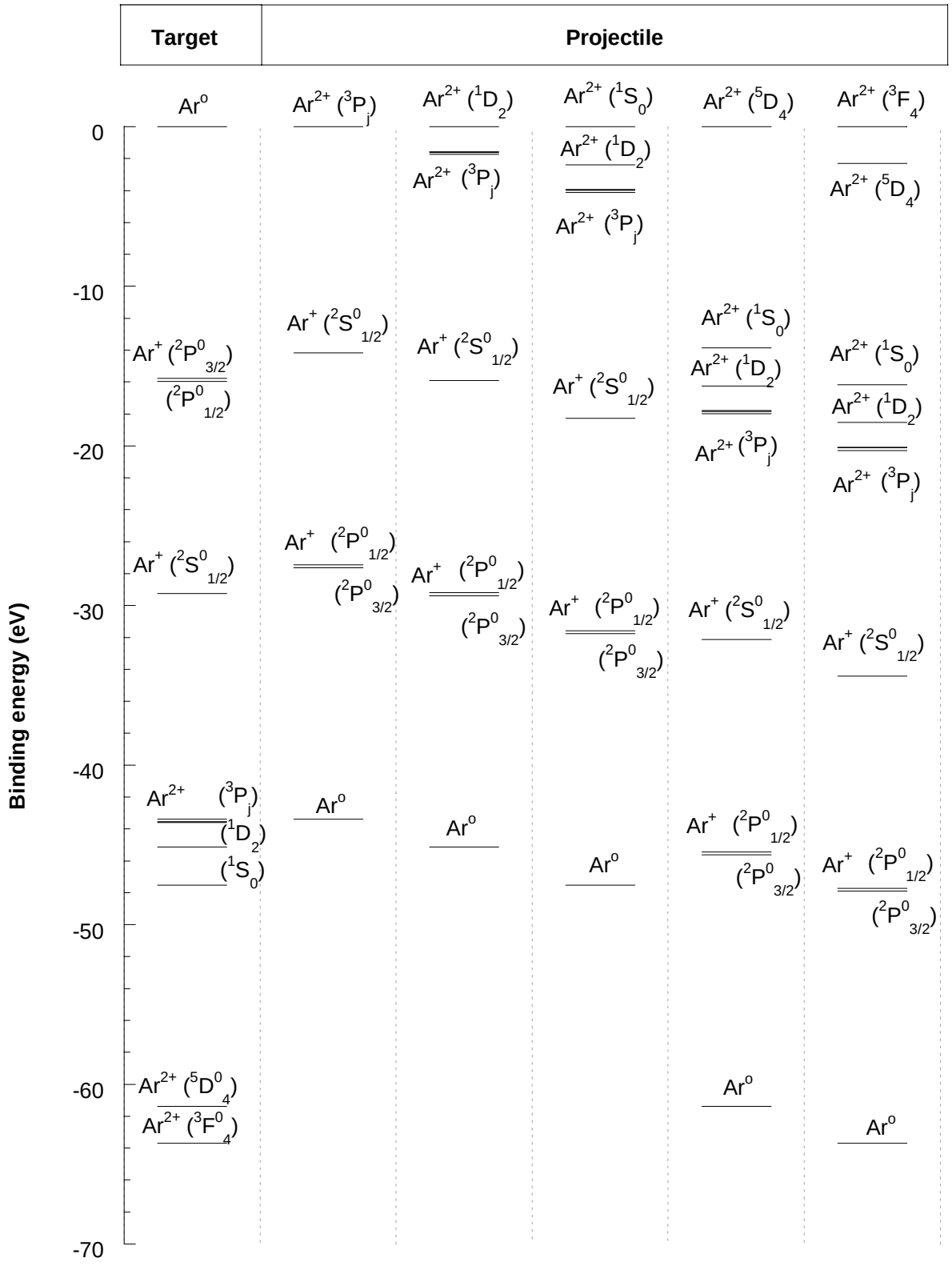

Figure 5.8 – Binding energy levels for some selected states relevant for single and double electron capture in Ar^{2+} – Ar collisions [69].

5.3.2. Ne^{2+} on Ne

Collisions of Ne^{2+} on Ne were performed in the impact energy range from 90 eV to 10 keV. The measured SEC and DEC cross sections are plotted as a function of collision energy and compared with previously published data in Figure 5.9.

Similar to Ar^{2+} – Ar collisions, the DEC cross section is again dominant and the DEC cross section values increase with decreasing collision energy. On the contrary, the SEC cross section steadily increases with increasing impact energy. Our results are in reasonably good agreement to previously published experimental data for both single- and double- electron capture.

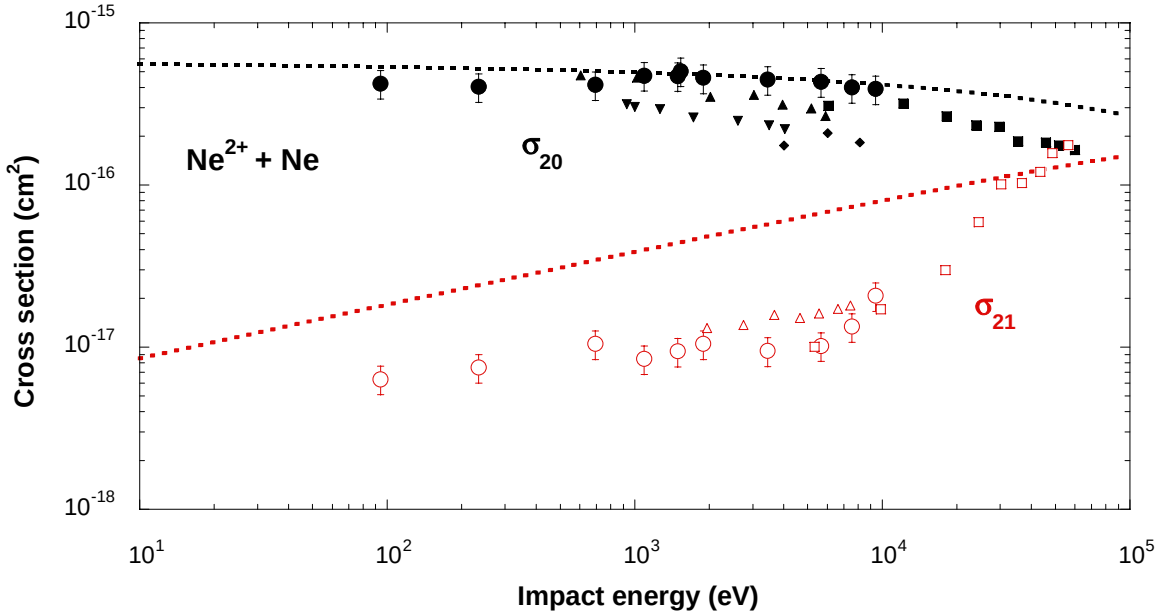

Figure 5.9 – SEC and DEC cross section for Ne^{2+}–Ne collisions as a function of impact energy. DEC cross section: full circles – this work, full triangles – experimental results by Latypov et al [86], full squares – experimental results by Flaks et al [87], full diamonds – experimental results by Kaneko [85], full inverted triangles – experimental results by Hasted et al [78]. SEC cross section: open circle – this work, open triangles – experimental results by Hertel et al [88], open squares – experimental results by Flaks et al [87]. Theoretical results: dashed black line – DEC cross section by EOBM, dashed red line – SEC cross sections by EOBM

Again, to our knowledge no systematic theoretical work has been carried out for this collision system, therefore we have performed LZ and EOBM calculations as outlined in sections 2.4 and 2.5, respectively.

The calculated SEC and DEC cross sections by EOB model are shown in Figure 5.9 in comparison to the experimental values. The calculations were performed using the respective

ionization potentials listed in Table 5.3. EOB model leads to a minimum distance for electron capture of R_m = 2.54 a.u. and predicts a DEC cross section almost independent of impact energy for energies below 10 keV and has a maximum value of about $5.5 \cdot 10^{-16}$ cm^2 at the lowest impact energy. Both the absolute magnitude and the dependency on impact energy are in a reasonable good agreement with our experimental data. The SEC cross sections calculated within the EOBM roughly agree in impact energy dependence but show much higher values for impact energies below 10 keV than our experimental SEC cross section data.

In order to perform Landau-Zener calculations, possible exothermic reaction channels must be identified. Table 5.3 summarizes the different reaction channels in the symmetric collision system Ne^{2+} - Ne and gives the energy defect (ΔE), crossing radius (R_c) and interaction matrix elements (H_{12}) obtained by the Landau-Zener method for these exothermic channels. Three exothermic channels can be associated to a single electron capture leaving the neon target in Ne^+ $2s^2$ $2p^5$ ground state configuration. However, it has been shown [89] that the dominant process should be the capture of a 2s electron into the Ne^+ ground state (process b) in Table 5.3) which is moderately endothermic and produces a $2s2p^6$ state in the target. The results of our LZ SEC calculation for the three exothermic channels from Table 5.3 are shown in Figure 5.10 and compared to the experimental data. For the exit channel a) the LZ model predicts much smaller values than the observed experimentally, while for exit channels d) and g) the cross section is overestimated. These results indicate that, although these exit channels have small energy defects, a SEC followed by excitation of the projectile is not very probable.

Table 5.3 – Individual reactions channels for charge transfer of $Ne^{2+}(2s^22p^4)$ + Ne $(2s^22p^6)$ collisions. Energy levels obtained from ref. [69].

	Reaction products	I_2 (eV)	I_1 (eV)	ΔE (eV)	R_c (a_o)	H_{12} (a.u.)
a)	$Ne^+(2s^2\ 2p^5) + Ne^+(2s^2\ 2p^5)$	40.96	21.56	19.40	1.40	0.376
b)	$Ne^+(2s^2\ 2p^5) + Ne^{+*}(2s\ 2p^6)$	40.96	48.47	-7.51	-	-
c)	$Ne^+(2s^2\ 2p^5) + Ne^{+*}(2s^2\ 2p^4\ 3s)$	40.96	49.41	-8.45	-	-
d)	$Ne^{+*}(2s\ 2p^6) + Ne^+(2s^2\ 2p^5)$	26.91	21.56	5.35	5.08	0.017
e)	$Ne^{+*}(2s\ 2p^6) + Ne^{+*}(2s\ 2p^6)$	26.91	48.47	-21.56	-	-
f)	$Ne^{+*}(2s\ 2p^6) + Ne^{+*}(2s^2\ 2p^4\ 3s)$	26.91	49.41	-22.50	-	-
g)	$Ne^{+*}(2s^2\ 2p^4\ 3s) + Ne^+(2s^2\ 2p^5)$	27.85	21.56	6.29	4.32	0.035
h)	$Ne^{+*}(2s^2\ 2p^4\ 3s) + Ne^{+*}(2s\ 2p^6)$	27.85	48.47	-20.62	-	-
i)	$Ne^{+*}(2s^2\ 2p^4\ 3s) + Ne^{+*}(2s^2\ 2p^4\ 3s)$	27.85	49.41	-21.56	-	-
j)	$Ne\ (2s^2\ 2p^6) + Ne^{2+}(2s^2\ 2p^4)$	62.52	62.52	0	-	-

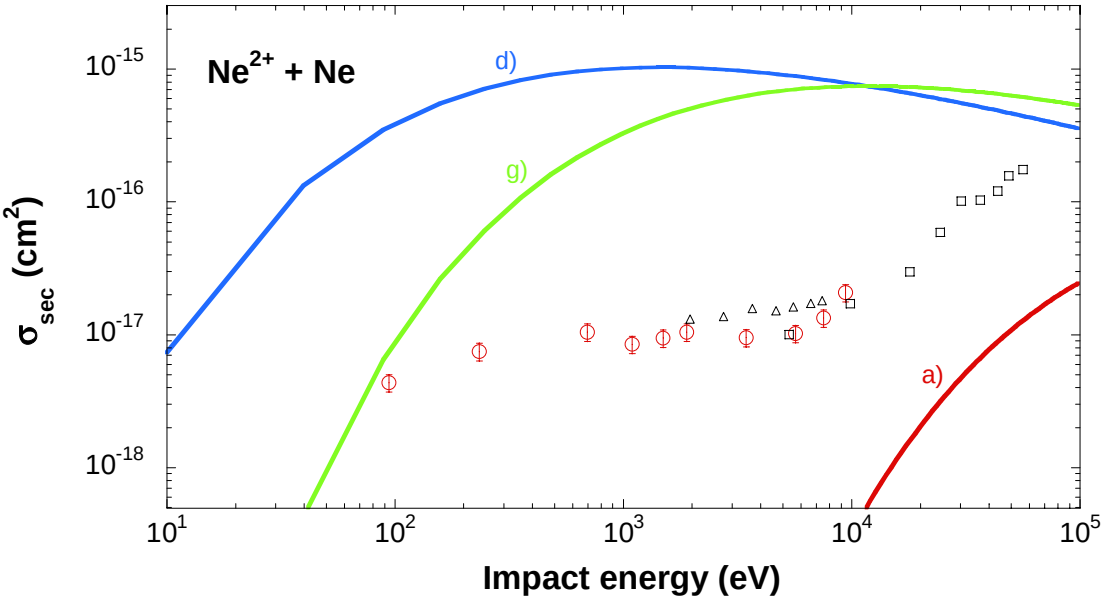

Figure 5.10 – SEC cross section for Ne^{2+} – Ne collision as a function of impact energy. Experimental data as in Figure 5.9. Full lines – present Landau-Zener calculation for the three exothermic reaction channel listed in Table 5.3 (c.f. text).

The cross section for electron production was again derived accordantly to the procedure outlined in section 4.3. Figure 5.11 shows the resulting electron production cross section values again interpreted as due to TI. These TI cross sections are small for lower impact energies but increase with increasing the impact energy. To our knowledge, there is no previous data on transfer ionization in the present energy range as well as for higher impact energies.

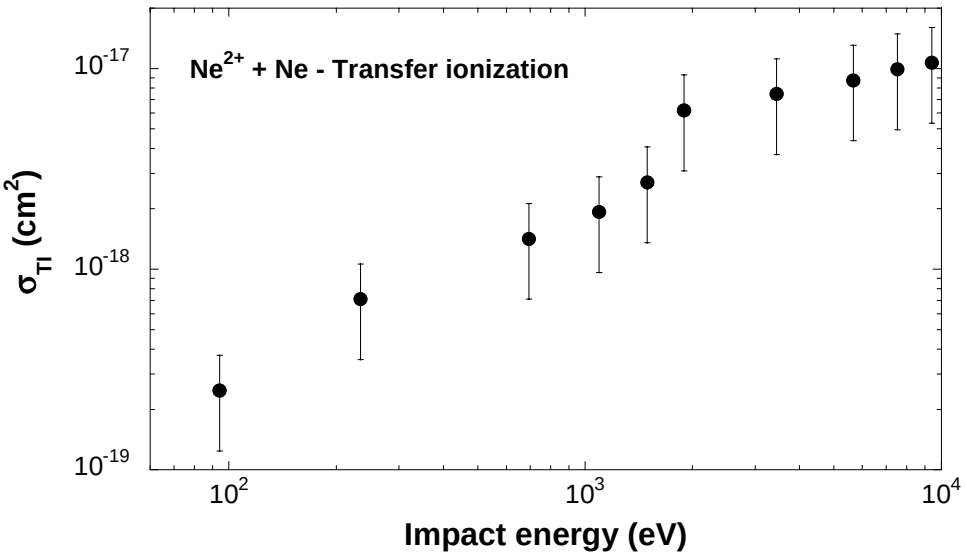

Figure 5.11 – Transfer ionization cross section for Ne^{2+} – Ne collision as a function of impact energy.

5.3.3. He^{2+} on He

Collisions of He^{2+} with He atom were performed in the impact energy range from 0.25 to 2.5 keV/amu. The measured cross sections for DEC and SEC are plotted as a function of collision energy together with previously published data in Figure 5.12. For the He^{2+} on He collision system there is a general agreement -both theoretically and experimentally - that the single electron capture cross section is small for energies below 10 keV/amu and the most favourable reaction is double electron capture. On the other hand, at energies above 10 keV/amu one-electron transitions dominate over two-electron transitions. This general feature of the He^{2+} - He collision system has been observed experimentally [90-92] and confirmed in calculations with adiabatic two-electron molecular wave-functions [93, 94] and in atomic orbital (AO) close coupling calculation [95]. As shown in Figure 5.12, our results are in good agreement with the data from the literature both for single- and double- electron capture. Moreover our results extend the cross section data to considerably lower impact energies, demonstrating that the observed trend continue with decreasing impact energy (i.e. the DEC cross section is dominant and its value increases while the SEC cross section is decreasing with decreasing impact energy).

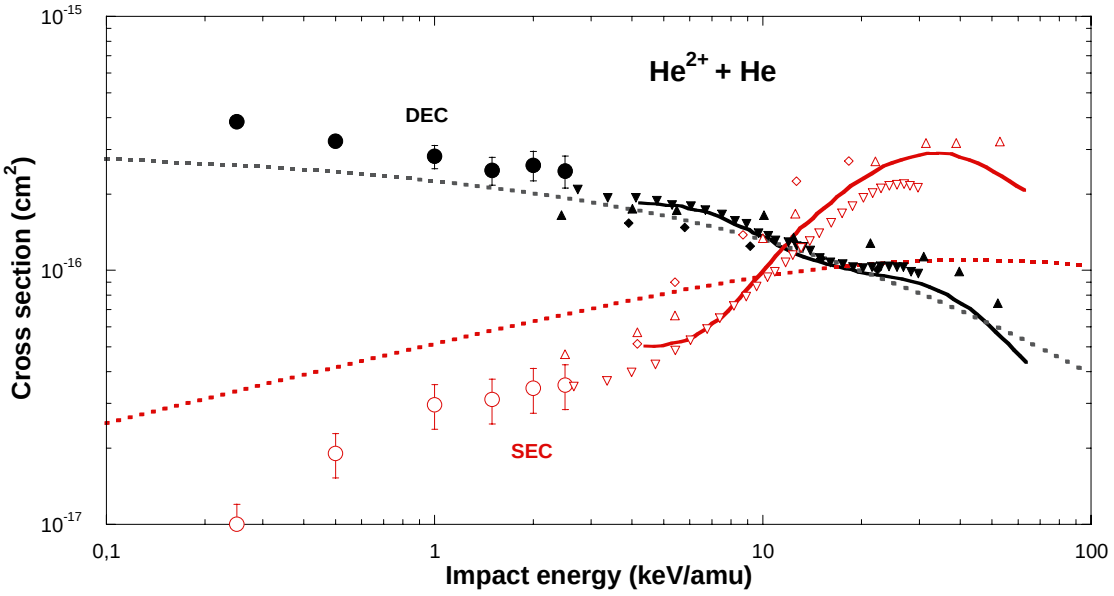

Figure 5.12 – Cross section for He^{2+}-He collisions as a function of impact energy. DEC cross section: full circles – this work, full triangles – experimental results by Berkner et al [92], full diamonds – experimental results by Bayfield et al [91], full inverted triangles – experimental results by Afrosimov et al [90], full red line – AO calculation by Fritsch [95]. SEC cross section: open circle – this work, open triangles – experimental results by Berkner et al [92], open inverted triangles – experimental results by Afrosimov et al [90], open diamonds – experimental results by Bayfield et al [91], full red line – AO calculation by Fritsch [95].

In addition we have performed LZ and EOBM calculations as described in sections 2.4 and 2.5, respectively.

The SEC and DEC cross sections as calculated by EOBM are also shown in Figure 5.12. The calculations were performed using the respective ionization potential given in Table 5.4. The calculated DEC cross sections lead to the minimum distance for electron capture of R_m = 1.91 a.u. and are in very good agreement with the experimental and theoretical data. On the other hand, the SEC cross section estimated by the EOBM predicts too higher values for impact energies below 10 keV (about a factor of 2) and only agrees qualitatively with the impact energy trend observed experimentally.

To perform Landau-Zener calculations, the possible reaction channels with exothermic reaction energy defect must be identified. The different reaction channels in the symmetric collision system He^{2+} - He are summarised in Table 5.4 together with the energy defect (ΔE). The crossing radius (R_c) and the interaction matrix element (H_{12}) values obtained by the Landau-Zener method for the exothermic channels are also shown in the table. The system is characterised by four exothermic channels, all of then associated to single electron capture and the remaining target in He^+ 1s configuration. All processes leading to target excitation have an endothermic energy defect and consequently the Landau-Zener method is not applicable.

Table 5.4 – Individual reactions channels for charge transfer of He^{2+} + He ($1s^2\ ^1S$) collisions. Energy levels obtained from ref. [69].

	Reaction products	I_2 (eV)	I_1 (eV)	ΔE (eV)	R_c (a_o)	H_{12} (a.u.)
a)	He^+ (1s) + He^+(1s)	54.42	24.58	+29.84	0.91	0.552
b)	He^+ (1s) + He^{+*}(n = 2)	54.42	65.31	-10.89	-	-
c)	He^+ (1s) + He^{+*}(n = 3)	54.42	72.95	-18.53	-	-
d)	He^+ (1s) + He^{+*}(n = 4)	54.42	75.60	-21.18	-	-
e)	He^{+*}(n = 2) + He^+ (1s)	40.81	24.58	+16.23	1.67	0.326
f)	He^{+*}(n = 3) + He^+ (1s)	48.37	24.58	+23.79	1.14	0.478
g)	He^{+*}(n = 4) + He^+ (1s)	51.02	24.58	+26.44	1.03	0.514
h)	He^{+*}(n l) + He^{+*}(n l)	-	-	<0	-	-
i)	He^+ (1s) + He^{2+} + e^-	54.42	~77	~ -23[†]	-	-
j)	He^{2+} + He (1s) + e^-	0	24.58	-24.6[†]		
l)	He ($1s^2\ ^1S$) + He^{2+}	79.0	79.0	0	-	-

[†] Ref. [96]

Figure 5.13 shows the SEC cross section as calculated by Landau-Zener theory together with experimental- and theoretical results as a function of impact energy. Results are shown for each exothermic channel in Table 5.4. The values for the crossing radii were found to be in a good agreement with the values from adiabatic potential energy curves [97, 98]. Electron capture into n=2 with the target remaining in He^+ 1s ground state (process e)) has the highest cross section in comparison to the other exothermic channels calculated by LZ theory. However the SEC values become very small for lower impact energy. These results show suggest that the target does not stay in the He^+ 1s ground-state when an electron is captured.

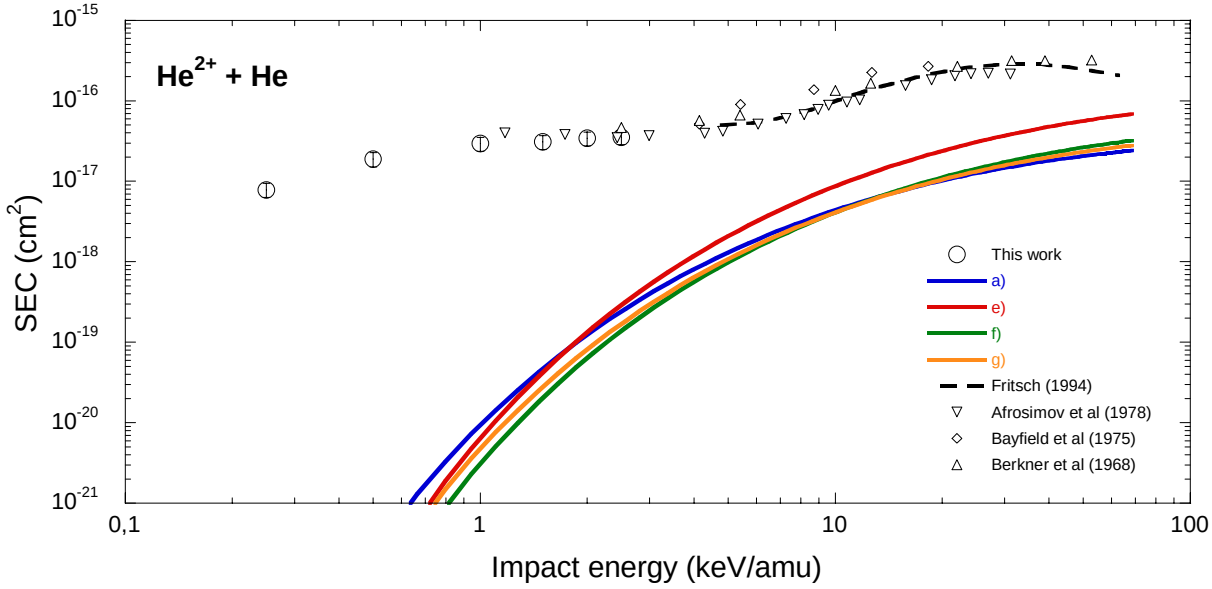

Figure 5.13 – Single electron capture cross section as a function of impact energy for the He^{2+} – He collision system. Experimental data as in Figure 5.12. Full lines – present Landau-Zener calculation for the four exothermic reaction channels listed in Table 5.4.

Similar to the collisions system presented previously, the cross section for electron production was derived accordantly to the procedure outlined in section 4.3. Figure 5.14 shows the resulting electron production cross section values again interpreted as due to TI. Our TI cross sections increase with increasing the impact energy are in a fair agreement with the tabulated values given by ref. [99].

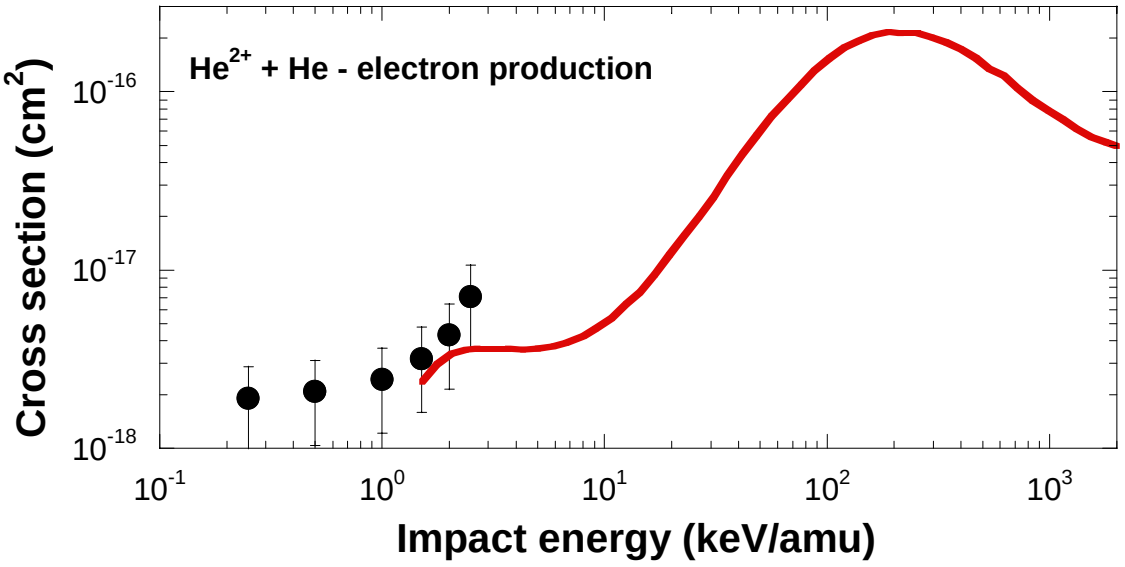

Figure 5.14 – Transfer ionization cross sections as a function of impact energy for the He^{2+} – He collision system. Full black circles – this work, open red circles – values from ref [99].

5.4. Charge-exchange in He^{2+} – Ne collisions

Collisions of He^{2+} on Ne have been extensively used for translational energy spectroscopy (TES) calibration [100, 101] in view of the fact that the associated energy defect for SEC is very characteristic. Nonetheless, only a few experimental results for SEC and DEC cross sections for this system exist and no theory has been applied so far. In the present work, we have measured SEC and DEC cross sections in the collision impact energy range from 0.1 to 6 keV. Additionally, we have carried out LZ and EOBM calculations as described in chapters 2.4 and 2.5, respectively.

The measured SEC cross sections and the results of our calculations are shown as a function of collision impact energy in Figure 5.15 and compared with previously published data. Our SEC cross section values increase monotonically with increasing impact energy and are in an excellent agreement with the experimental results of Hanaki [102]. Unfortunately, the connection to data points for impact energies above 5 keV/amu is not quite clear.

By means of TES, some exit channels have been found to be present [101] in collision of He^{2+} with Ne. The by far most probable reaction channel for SEC is given by [100]:

$$He^{2+} + Ne\ \ 2s^2 2p^6\ {}^1S \rightarrow He^{+}(1s) + Ne^{+*}\ \ 2s2p^6\ {}^2S \quad \text{with}\ \ \Delta E = 5.94\ \text{eV}\,, \qquad (5.6)$$

this reaction has a crossing distance (R_c) at about 4.6 a.u. as shown in the potential curves of $^1\Sigma^+$ states for the $(HeNe)^{2+}$ quasimolecule (see Figure 5.16, [103]).

The SEC cross sections calculated by LZ theory predicts a maximum value of $8.5 \cdot 10^{-16}$ cm^2 at an impact energy about 7 keV/amu, which is a factor of 1.7 higher than the maximum value measured by Rudd et al [104]. Furthermore, the theoretical cross sections decrease abruptly for impact energies below 1 keV/amu, a trend not observed experimentally. On the other hand, the EOBM results show a much better agreement with the experimental impact energy dependence but are about a factor of 1.5 higher than the experimental values. The model predicts a maximum SEC cross section for impact energies between 10 and 20 keV/amu, which is in a fair agreement with the data of Rudd et al [104] and Dubois et al [105].

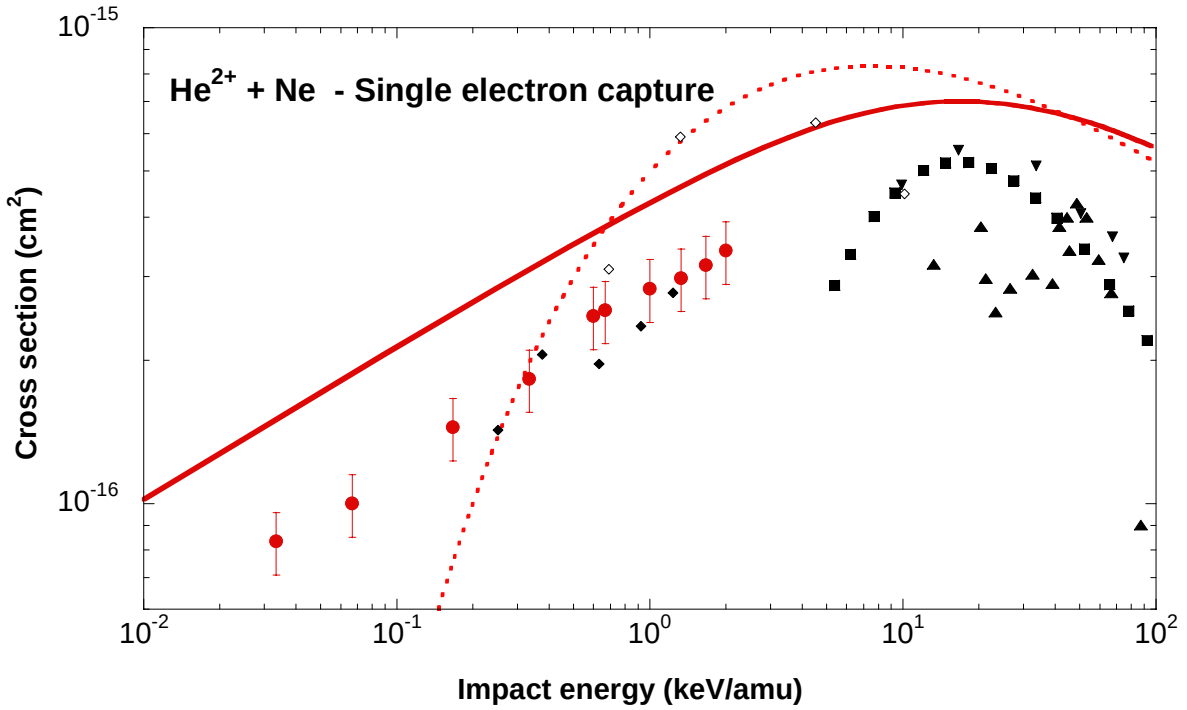

Figure 5.15 – SEC cross section cross sections for $^3He^{2+}$-Ne collisions as a function of impact energy. Full circles – experimental results from this work, full diamonds – experimental results by Hanaki et al. [102], full squares – experimental results by Rudd et al. [104], full triangles – experimental results by Baragiola et al [106], inverted triangles – experimental results by DuBois et al [105], open diamonds – experimental results by Afrosimov [90] et al. Theoretical results from this work: dotted line – LZ theory, full line – EOBM calculation.

Our measured DEC and calculated EOBM cross sections and are plotted as a function of collision energy in Figure 5.17 together with previously published data. In fair agreement with the data of Hanaki [102] our measured DEC cross section values decrease with decreasing impact energy, however the absolute values of these authors are about a factor of 2 smaller than ours at 600 eV/amu. The present results can be smoothly connected to data at

higher impact energies [104, 106]. For impact energies above 500 eV/amu, the DEC cross sections exceed the SEC cross section values. The corresponding reaction channel is [107]:

$$He^{2+} + Ne\ \ 2s^2 2p^6\ {}^1S \rightarrow He^*(2\ {}^3S) + Ne^{2+}\ \ (2p^4\ {}^3P) \quad \text{with} \quad \Delta E = -3.41 \text{ eV} . \qquad (5.7)$$

which has a smaller energy defect than the most favourable reaction for SEC. For impact energies lower than 500 eV/amu, however, the SEC cross sections are surprisingly greater than DEC.

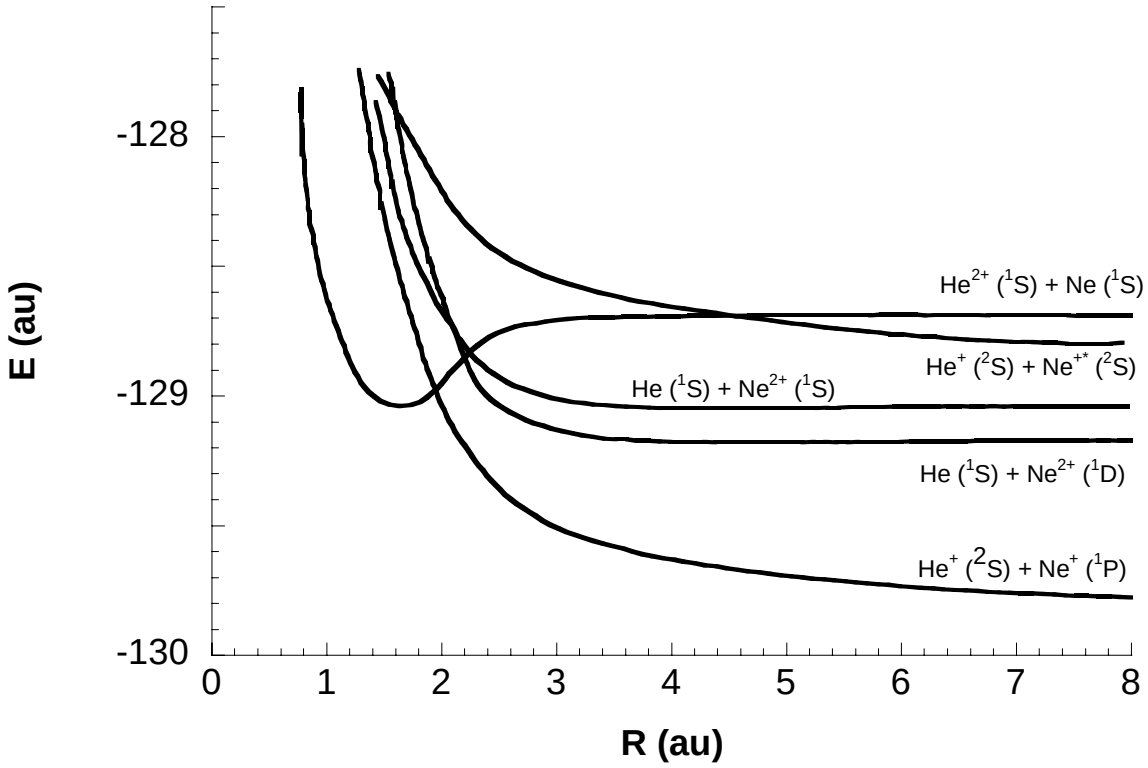

Figure 5.16 – Quasidiabatic potential curves of $^1\Sigma^+$ states for the $(HeNe)^{2+}$ quasimolecule (taken from [103]).

We have also carried out EOBM calculations for DEC. The results are shown in Figure 5.17. While there is a quite good agreement with experimental data at high impact energies, the model predicts a monotonically increasing cross section with decreasing impact energy for impact energies below 1 keV/amu in striking contrast to our experimental results. A possible explanation for these high cross sections at lower impact energies could be the fact that the model considers hydrogen-like states for both the target and the projectile in order to calculate the effective quantum number *n* which labels the binding energy of the electron (equation (2.44)). This approximation results in the "no-return" -hypothesis: once the electron crosses the barrier, it will not return to the target. This hypothesis migth be well justified for projectiles with high atomic number, as already pointed out in [54], but this is not the case for

He^{2+} – Ne collisions, where the atomic number of the projectile is much smaller than the atomic number of the target and therefore the recapture of electron by the target must be taken into acount.

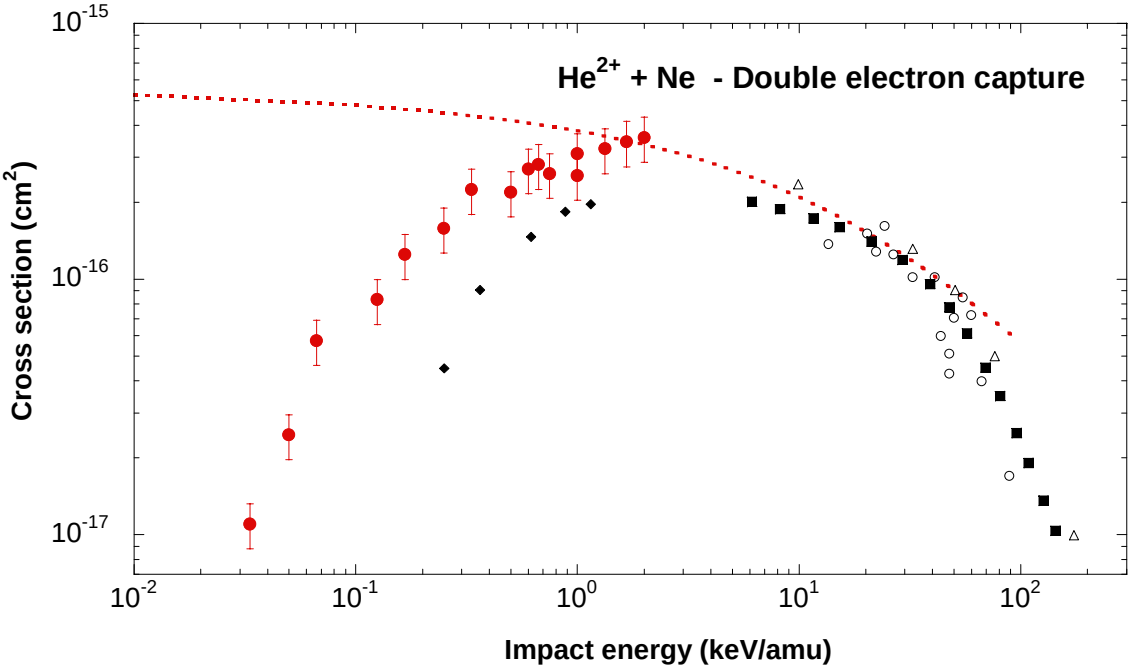

Figure 5.17 – DEC cross section for $^3He^{2+}$ – Ne collisions as a function of impact energy. Full circles – experimental results of this work, full diamonds – experimental results by Hanaki et al [102], full squares – experimental results by Rudd et al [104], open circle – experimental results by Baragiola et al [106], open triangles – experimental results by DuBois et al [105], dotted line – EOBM calculation from this work.

Figure 5.18 shows the resulting electron production cross section values again interpreted as due to TI. Our TI cross sections increase with increasing the impact energy and can be smoothly connected to the electron production measurement by Rudd et al [104].

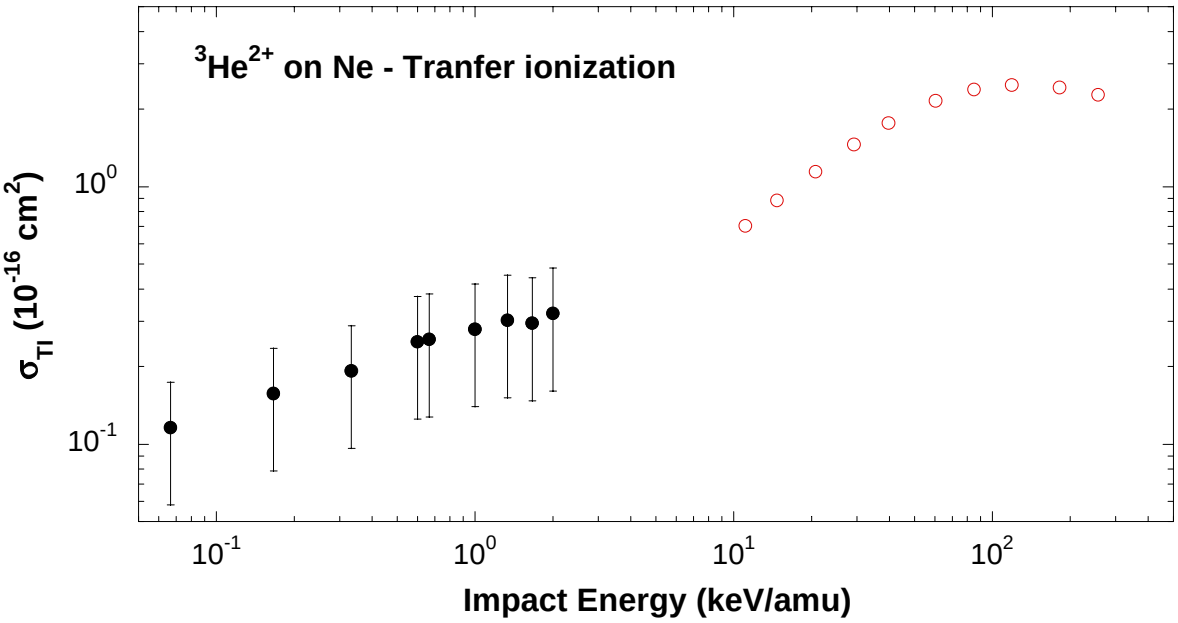

Figure 5.18 – Transfer ionization cross section for He^{2+} – Ne colision as a function of impact energy. Full black circles – experimental results from this work, open red circles – experimental results by Rudd et al [104].

5.5. Electron capture for doubly charged ions colliding with molecules

Collisions of He^{2+} with O_2 and H_2 were measured for ion impact energies below 2000 eV/amu. The final impact energies were defined by both the potential applied to the ion source and the deceleration voltage applied to the gas cell. In order to check the influence of electrostatic lenses at low impact energies, several different combinations of the source and deceleration voltages leading to the same impact energy were applied but no systematic difference between the results was found. The associated error bars give the absolute errors. In the worst case the absolute errors were estimated to be about 20%.

In contrast to ion-atom collisions, the EOB model is very limited for application to ion-molecule collisions because the potential barrier formed between collision partners is considered with a two-centre Coulombic potential for the respective electrons. The applicability for molecular collision would be justified as far as the relevant critical barrier distance is much larger than the molecular sizes, which are not the case of the ion-molecule collision systems investigated in this work, for which the multi-centre nature of target molecules is expected to be of great importance. A three-centre Coulomb over-barrier model has been proposed by Ichimura and Yamaguchi [108] but their model is velocity independent consequently resulting in a geometrical cross section (similar to equation (2.40)). A more

precise model would incorporate the multi-centre nature of the molecular targets, the relative velocity between the nuclei, the molecules orientation and the angular momentum of the electrons, but this development is out of the scope of this thesis.

5.5.1. He^{2+} - O_2 collisions

In charge exchange processes of He^{2+} colliding with O_2, cross section data are still scarce in the literature and no systematic theoretical work has been carried out. Ishii et al. [109] reported SEC and DEC cross sections for He^{2+} - O_2 collisions at low impact energy where they showed that the DEC cross section appears to dominate the SEC cross section below 100 eV/amu. Okuno et al. [110] studied the DEC processes for He^{2+} - O_2 collisions by means of a double coincidence time of flight spectroscopy where they identified the exit channels with respective branching rations. Recently Kusakabe et al. [111] presented single and double electron capture cross sections for He^{2+} impact on various molecular targets (among them O_2 and H_2) in the energy range from 0.6 to 2.7 keV/amu. Other experimental investigations of the He^{2+} - O_2 collision system have been concerned mainly with the measurements of state selective single electron capture by means of translational energy spectroscopy (TES) [100, 112-115].

For the impact energy range investigated in this work, it is expected that the following processes are most important during single collisions of He^{2+} with O_2 molecules:

(Non-dissociative SEC) $He^{2+} + O_2 \rightarrow He^{+}(n=2) + O_2^{+}\ (\Delta E = 1.3\ eV)$ (5.8)

(Dissociative SEC) $He^{2+} + O_2 \rightarrow He^{+}(n=1) + O_2^{+*}$ (many dissociative states) (5.9)

(Dissociative DEC) $He^{2+} + O_2 \rightarrow He + O^{+} + O^{+}$ (5.10)

$He^{2+} + O_2 \rightarrow He + O^{2+} + O$ (5.11)

(Diss. DEC with ionization) $He^{2+} + O_2 \rightarrow He + O^{2+} + O^{+} + e^{-}$ (5.12)

The processes (5.10), (5.11) and (5.12) were identified by means of double coincidence time-of-flight [110] at 1 keV/amu impact energy with 78%, 9.9% and 12% branching ratios respectively. The process (5.8) represents the non-dissociative single electron capture into n=2 states of He^{+} with production of O_2^{+} in the ground state $(X\,^2\prod_g)$. Process (5.9) has a rather broad energy gain ($6 < \Delta E < 10$ eV) and represents the dissociative single electron capture into the n=1 state of He^{+} with production of O_2^{+} in several excited states [100, 112, 113].

In our setup we are only able to distinguish between SEC (process (5.8)+(5.9)) and DEC (process (5.10)+(5.11)+(5.12)). The measured SEC and DEC cross sections are shown in Figure 5.19 and Figure 5.20 as a function of impact energy. The measurements were not only performed with $^4He^{2+}$ but also with $^3He^{2+}$ isotopes in order to check whether possible impurity ions with the same mass to charge ratio (e.g. H_2^+) as $^4He^{2+}$ influence the measured signals. The cross section results for both isotope projectiles agree very well, which indicates that the contribution from H_2^+ projectiles is of no relevance.

As far as SEC cross sections are concerned, the present results are in reasonably good agreement with previous measurements, although we could neither fully reproduce the trend presented by Ishii et al. [109] nor Kamber et al [112]. The SEC cross section increases with increasing incident energy. Unfortunately the connection with data for impact energies above 5 keV/amu is still not clear yet (see Figure 5.19).

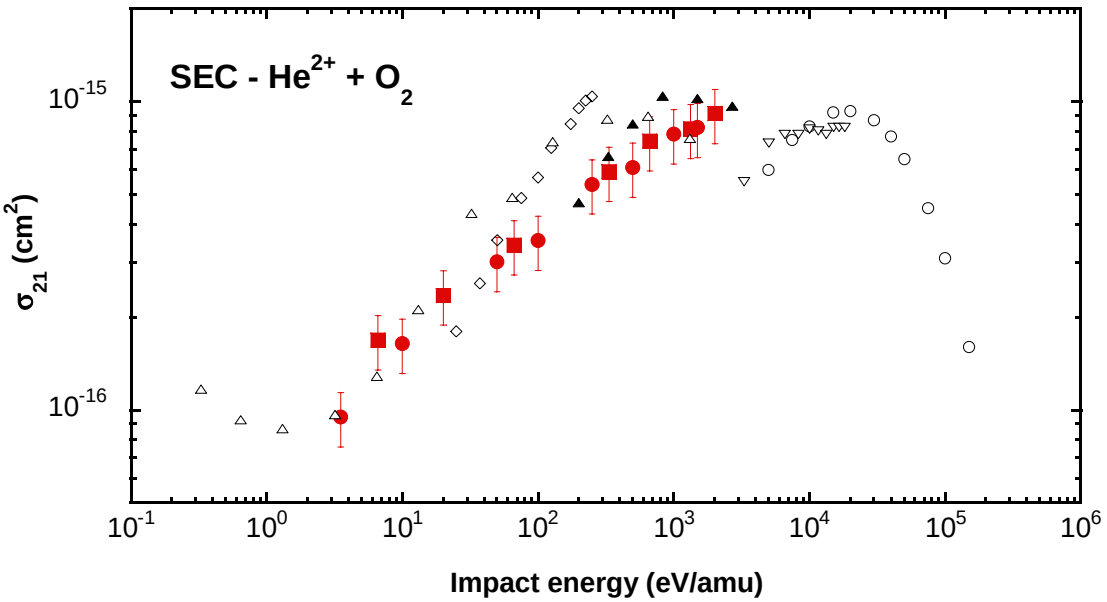

Figure 5.19 – SEC cross section for $^4He^{2+}$ and $^3He^{2+}$ – O_2 collisions as a function of impact energy. Full circles – experimental results from this work ($^4He^{2+}$ projectiles), full squares – experimental results from this work ($^3He^{2+}$ projectiles) , full triangles – experimental results by Kusakabe et al. [111], open diamonds – experimental results by Kamber et al. [112], open triangles – experimental results by Ishii et al. [109], open circles – experimental results by Rudd et al. [104], inverted open triangles – experimental results by Shah and Gilbody [116].

In the impact energy range from 0.2 to 2 keV/amu our data for the DEC cross section agree very well with earlier experimental results (Figure 5.20). For impact energies below 0.2 keV/amu our cross sections increase as the collision energy decreases. This is in qualitative agreement with results of Ishii et al [109], but these authors obtained higher values for the

DEC cross sections. A possible explanation for this difference could be the limited acceptance angle of their experiment leading to an artificial increase of beam current attenuation with decreasing impact energy. Our apparatus, on the contrary, is designed to accept scattering angles up to ±8° (c.f. chapter 3.3.2).

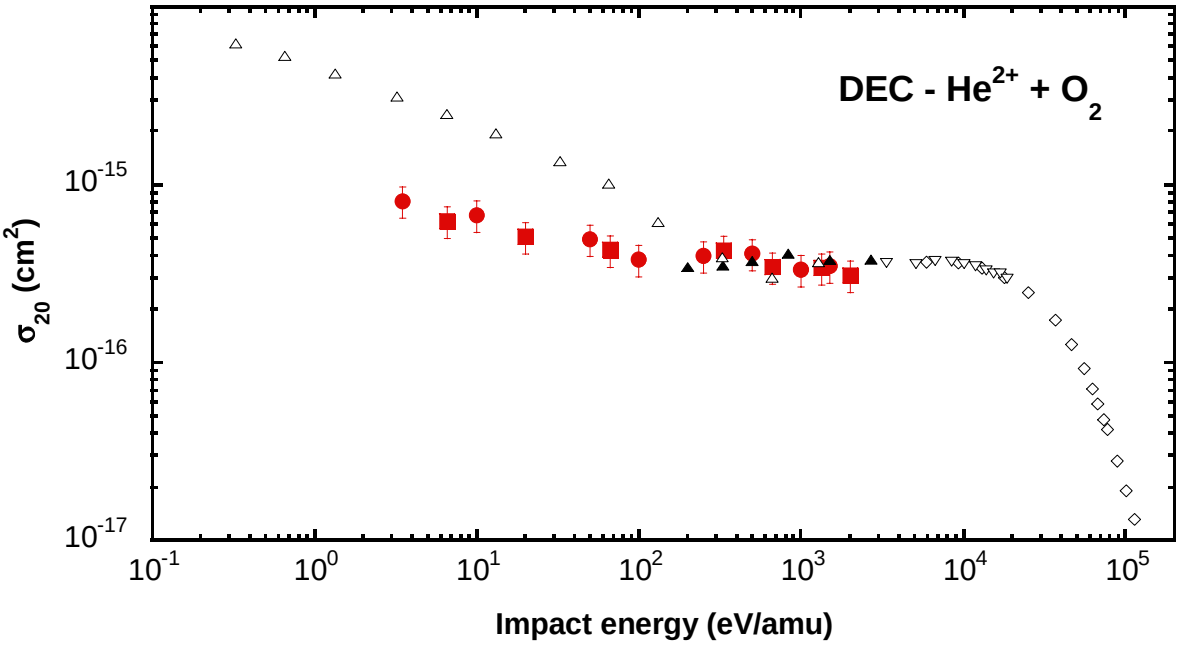

Figure 5.20 – DEC cross section for $^4He^{2+}$ and $^3He^{2+}$ on O_2 collisions as a function of impact energy. Full circles – experimental results from this work ($^4He^{2+}$ projectiles), full squares – experimental results from this work ($^3He^{2+}$ projectiles) , full triangles – experimental results by Kusakabe et al. [111], open triangles – experimental results by Ishii et al. [109], open diamonds – experimental results by Rudd et al. [104], inverted open triangles – experimental results by Shah and Gilbody [116].

5.5.2. He^{2+} – H_2 and He^{2+} – D_2 collisions

For charge exchange processes of He^{2+} with H_2 molecules quite a few number of experimental data [9, 91, 100, 104, 106, 111, 117-120] and theoretical results [71, 121-123] have been published at intermediate and low impact energies. However, for ion impact energy < 1 keV/amu these results remain inconclusive. Measurements by Shah and Gilbody [116] and Kusakabe et al. [118] of SEC and DEC processes above 1 keV/amu showed that SEC is dominant by about an order of magnitude in the cross section. The measurement of the same processes at low energies by Okuno et al. [120] has indicated that the DEC cross section dominates over the SEC cross section. Shimakura et al. [71] studied theoretically SEC and DEC processes in the energy range from 17 eV/amu to 0.67 keV/amu based on a molecular orbital expansion method and showed that the calculated DEC cross sections values indeed

exceed the SEC values below 100 eV/amu. Recently Kusakabe et al. [111] presented their experimental SEC and DEC cross section in the energy range from 0.6 to 2.7 keV/amu where they found that SEC is the dominant reaction and that the DEC cross sections have a nearly constant value at their impact energy range.

In the low impact energy range the following processes are most relevant in He^{2+} – H_2 (D_2) collisions:

$$He^{2+} + H_2 \longrightarrow He + H^+ + H^+ \tag{5.13}$$

$$He^{2+} + H_2 \longrightarrow He^+ + H_2^+ \tag{5.14}$$

$$He^{2+} + H_2 \longrightarrow He^+ + H^+ + H \tag{5.15}$$

$$He^{2+} + H_2 \longrightarrow He^+ + 2H^+ + e^- \tag{5.16}$$

Process (5.13) is the double electron capture (DEC), with associated cross section σ_{20}, which leads to target dissociation due to Coulomb explosion. Process (5.14) is the non-dissociative single electron capture (SEC-ND) leading to the formation of He^+ (n = 2) with a minimum endothermic energy defect about -1.8 eV which can be broadened due to vibrational excitation ($\nu = 0 \rightarrow \infty$) of the H_2^+ molecular product ions [117]. The dissociative single electron capture (SEC-D) reaction (process (5.15)) also carries a broad defect energy associated to the limits of Franck-Condon transitions from the H_2 $^1\Sigma_g$ ground state to repulsive states of H_2^+ leading to H^+ + H(2s) and H^+ + H(2p) products [100, 117]. Process (5.16) is the single electron capture with target excitation followed by electron ejection (SEC-TI) and can possible to form a large number of dissociative H_2^{+*} states. At our low impact energies SEC-TI reaction channels prefer considerably small exothermic defect energy (typically ΔE = 5 eV [100]).

The present experimental cross sections for SEC (reactions (5.14) - (5.16)) and DEC (reaction (5.13)) of $^3He^{2+}$ colliding with H_2 as a function of impact energy are shown in Figure 5.21 and Figure 5.22, respectively. In contrast to O_2 target, only $^3He^{2+}$ ions have been used as projectiles because back-diffusion of H_2 from the collision cell into our ECR ion source could be observed.

Our experimental SEC cross section results are found to be in agreement with Okuno *et al.* [120] and connect smoothly to Kusakabe et al. [118] and Shah and Gilbody [116]. We note that the present SEC cross sections are in excellent agreement with the close-coupling calculation of Kusakabe et al. [111] and fair agreement with the theoretical results of Shimakura [71].

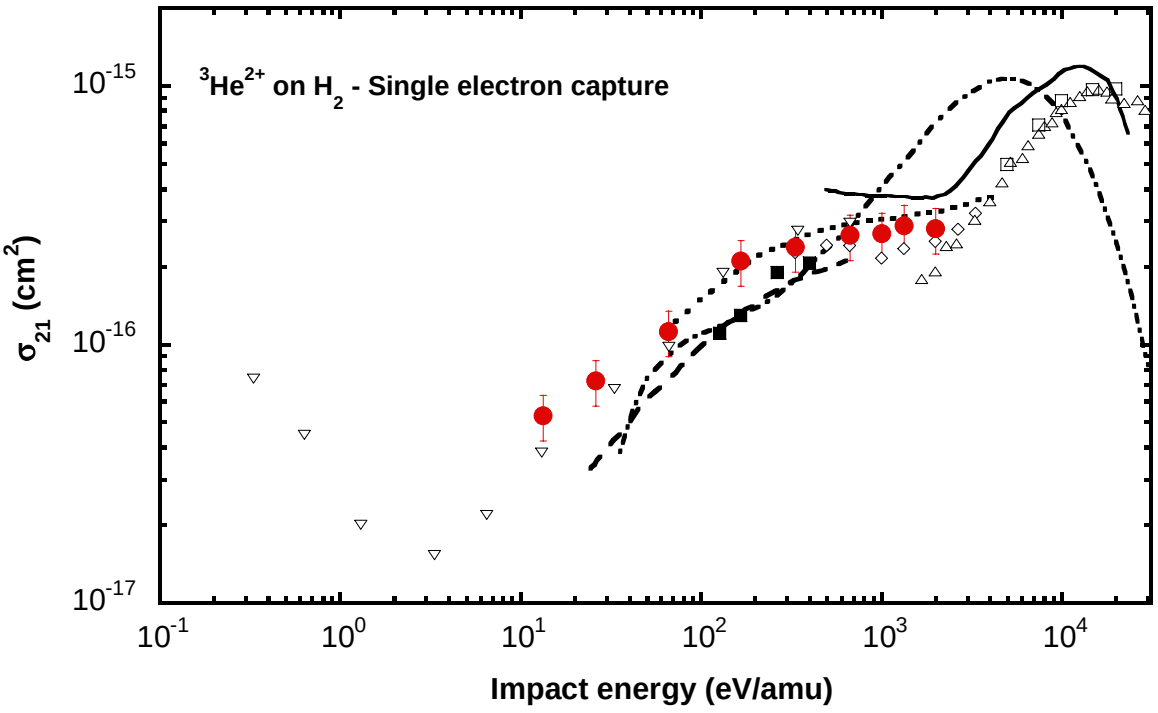

Figure 5.21 – SEC capture cross section for $^3He^{2+}$ – H_2 collisions as a function of impact energy. Experimental results: full circles – this work, full squares – Kusakabe et al [111], open diamonds – Kusakabe et al. [118], open inverted triangles – Okuno et al. [120], open squares – Rudd et al. [104], open triangles – Shah and Gilbody [116]. Theoretical results: full lines – Errea et al. [121], dashed line – Shimakura and Kimura [71], dotted line – Kusakabe et al. [111] dashed-dotted line – tabulated values from [99].

For the DEC cross section, all experimental and theoretical results are in reasonable agreement above 1 keV/amu impact energy. For lower impact energies considerable deviations occur. Okuno et al. [120] found that DEC cross section has a monotonically increasing trend as impact energy decreases and dominates over the SEC cross section for lower impact energies. The theoretical work by Shimakura et al. [71] based on a molecular orbital expansion method supports this trend by showing that indeed the calculated DEC cross sections values exceed the SEC values below 100 eV/amu. In the experimental results presented by Kusakabe et al [111, 118] on the other hand the DEC cross section values do not exceed the SEC cross section. They even report a plateau in the range of 0.13-0.8 keV/amu for DEC cross section, which is to some extent supported by their own close-coupling calculation. The present DEC cross section for $^3He^{2+}$ on H_2 collisions are shown in Figure 5.22 together with previous data. Our DEC cross sections increase monotonically as the impact energy decreases and exceed the SEC for impact energies below 100 eV/amu. Our data are in very good agreement with the theory by Shimakura et al [71] and closely follow the trend of the data by Okuno et al, whose absolute cross section values are about a factor of

2 higher. Again a possible reason for this difference could be due to the small acceptance angle of their experiment, as discussed before. The present DEC cross sections were cross-checked by measurements of the slow ions produced during the collision. As a result we found no discrepancy between the DEC cross section obtained from slow ions- and from attenuation- measurements within our experimental uncertainties.

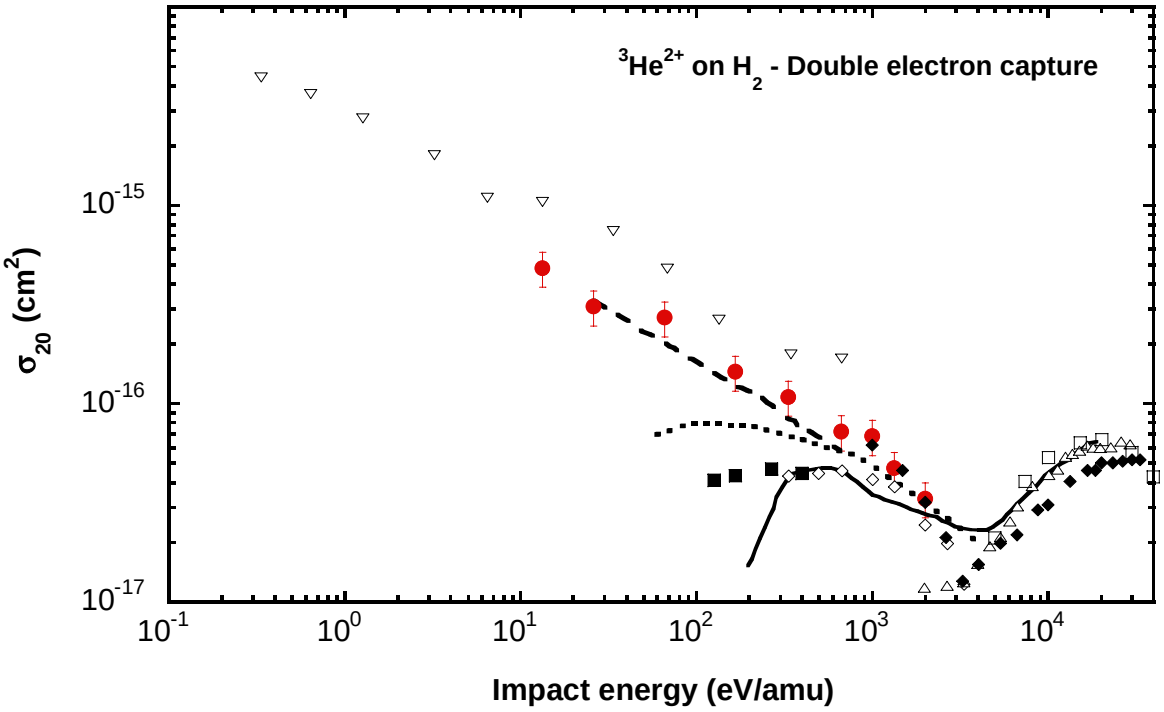

Figure 5.22 – DEC capture cross section for $^3He^{2+}$ – H_2 collisions as a function of impact energy. Experimental results: full circles – this work, full squares – Kusakabe et al [111], open diamonds – Kusakabe et al. [118], open inverted triangles – Okuno et al. [120], open squares – Rudd et al. [104], full diamonds – Afrosimov et al. [124], open triangles – Shah and Gilbody [116]. Theoretical results: full lines – Errea et al. [121], dashed line – Shimakura and Kimura [71], dotted line – Kusakabe et al. [111].

In addition, the transfer ionization cross section (σ_{TI}) obtained by measurement of slow electrons (Eq.(4.11)) has been determined and is shown in Figure 5.23. The σ_{TI} cross section for transfer ionization (reaction (5.16)) increases with increasing impact energy and can be smoothly connected to the measurement by Rudd et al [104].

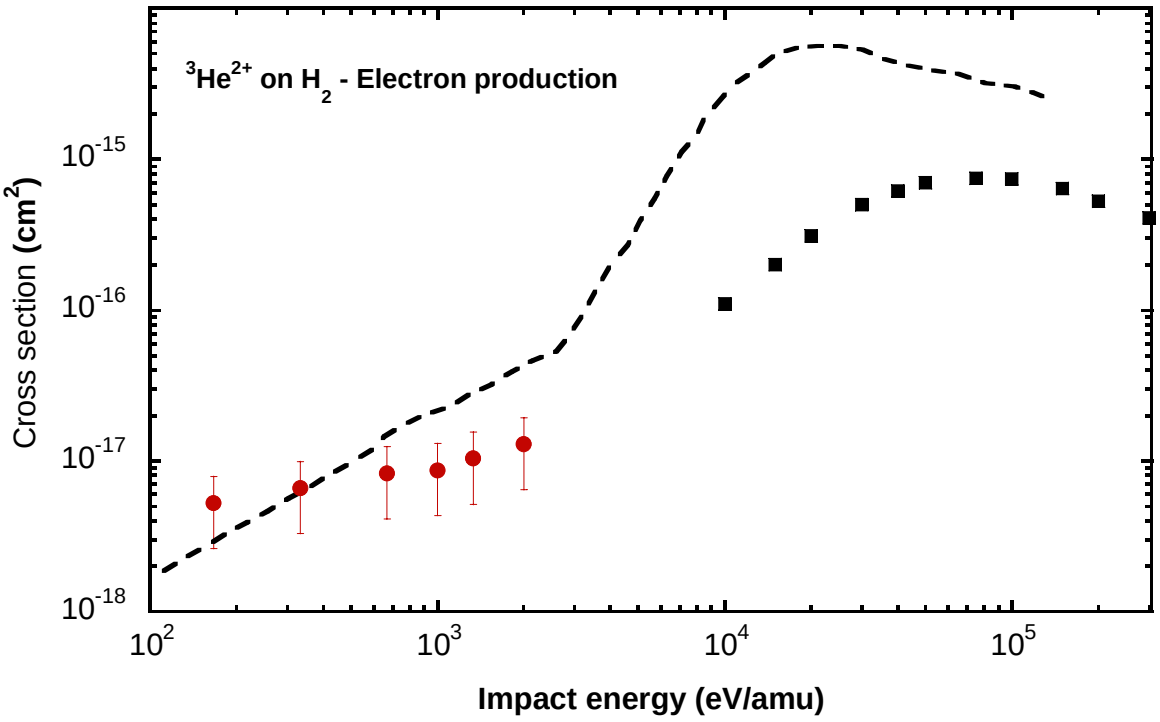

Figure 5.23 – TI cross section (process (5.16)) for $^3He^{2+}$ – H_2 collisions as a function of impact energy. Full circles – present work, full squares – Rudd et al [104], dashed line – TI from ref. [99].

We have also carried out additional measurements for $^3He^{2+}$ – D_2 collisions. D_2 was used since the electronic processes are expected to be identical to those in H_2 targets but the heavier isotope provides kinematic differences e.g. projectile scattering with a larger laboratory angle. SEC and DEC cross sections for $^3He^{2+}$ – D_2 compared to $^3He^{2+}$ – H_2 collisions as a function of impact energy in the centre of mass system are shown in Figure 5.24. We do not observe any systematic changes between H_2 and D_2 results and therefore conclude that our apparatus collects practically all product ions during the collisions even for larger scattering angles.

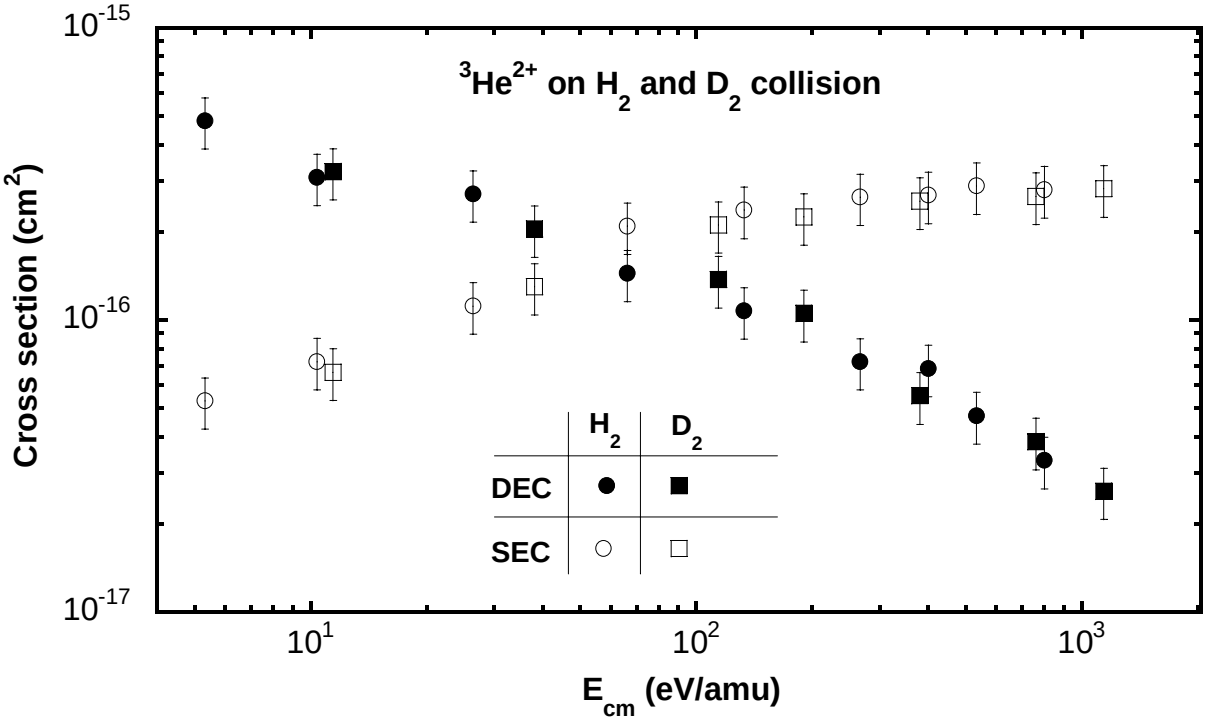

Figure 5.24 – SEC and DEC cross sections for $^3He^{2+}$ – D_2 compared to $^3He^{2+}$ – H_2 collisions as a function of impact energy in centre of mass system. SEC: open circles – experimental results for the H_2 target, open squares – experimental results for the D_2 target. DEC: full circles – experimental results for the H_2 target, full squares – experimental results for the D_2 target.

6. Conclusion and outlook

In this thesis an experimental study of electron capture and ionization processes for (singly and doubly charged) ions colliding with atoms and molecules at low impact energies is presented. These processes play an important role in man-made and astrophysical plasmas.

We have designed, tested and built an apparatus for single- and double-electron capture cross section measurements, which is especially well suited for low impact energy ($100 < E < 2000$ eV). The experimental technique combines collection of slow product ions with primary ion beam attenuation and projectile ions selection by a retarding electric field in a differentially pumped target gas chamber, where the pressure is measured by an absolutely calibrated capacitance manometer.

During the thesis, the experimental setup has been improved to achieve more precise data. In earlier measurements of the resonant SEC cross section for impact of slow singly charged noble gas ions on their atoms (He, Ne, Ar), a discrepancy between values obtained by attenuation technique and slow ions collection has been found. By introducing a larger aperture after the collision region, we could show that the acceptance angle of the initial design was not sufficiently large to collect all projectiles. Therefore, the experimental setup was modified in order to accept larger scattering angles. The good agreement between results for both techniques allowed us to calibrate the transparency factor for the meshed cylinder. Reproducibility of the measured cross sections for different experimental runs was achieved by monitoring the target impurities. The experimental results obtained for the resonant SEC cross sections were found to be in a good agreement with previously published data from the literature, which gave us confidence to also conduct investigations for more complicate collision systems.

Measurements of SEC and DEC cross sections of doubly-charged projectile ions incident on their own neutral atoms (Ar^{2+}, Ne^{2+} and He^{2+}) have been carried out. For all symmetric collision studied in this work, we found that two-electron capture processes take place predominantly at low collision velocity but decrease with increasing impact energy. Such behaviour can be understood because of the resonant nature of the capture process (i.e.

the total internal energy before the collision is the same as that after the collision). On the other hand, the SEC cross sections steadily increase with increasing impact energy. With the exception of Ar^{2+} – Ar collisions, we have extended the cross sections values for the first time towards very low impact energies. All our results were found to be in a reasonably good agreement with previously published experimental data for both single- and double- electron capture.

SEC and DEC cross sections for He^{2+}-Ne collisions have been determined at low impact energies for the first time. To our surprise, we found that at impact energies lower than 500 eV/amu the SEC cross sections exceed the DEC values, although the DEC process has a smaller energy defect associated with it than the SEC. At higher impact energies, the results are also found to be in good agreement to previously published data.

Furthermore, we have measured single and double electron capture cross sections for He^{2+} colliding with O_2, H_2 and D_2. For all molecular targets investigated in this thesis the single electron capture cross sections increase slowly as the collision energy increases, while the opposite trend is observed for the double electron capture cross sections. For H_2 and D_2 targets the DEC cross section exceeds the SEC for impact energies below 100 eV/amu. This fact could be of considerable importance for the removal of He-ash in future burning D–T fusion plasmas. The large cross sections for DEC at low energies can be attributed to the existence of outgoing channels with favorable (small) energy defects.

Additionally, also the electron production in collisions of doubly charged ions with atoms and molecules has been measured. From such measurements, TI cross sections were derived by subtracting contribution due to ion induced electron emission. This procedure, however, results a large uncertainty for the obtained TI-values. Despite the large error bars, we have found that the TI cross sections are small at low impact energies but increase with impact energy, while this is, in principle, expected. It was, in most cases, not possible to compare the obtained experimental results to literature values, because there are no previous data on transfer ionization in the present energy range or at higher impact energies.

Moreover, calculations based on the LZ theory and the EOB model have been performed and the results compared to our experimental data. In the majority of the cases, the calculated SEC by LZ theory underestimates the experimental values, which can be understood by the fact that only exothermic channels are considered in this theory. On the other hand, the EOBM results surprisingly show a much better agreement with the experimentally observed impact energy dependence as well as the absolute cross section magnitude. Due to the two-centre Coulombic potential character of the model, it was only

possible to apply the model for ion – atom but not for ion-molecule collisions. To apply the EOBM for ion – molecule collisions would requires incorporating the multi-centre nature of the molecular targets, the relative velocity between the nuclei, the molecules orientation and the angular momentum of the electrons.

Once published our experimental data, will hopefully also stimulate more refined theoretical (e.g. close coupling) calculations for a more complete understanding of the behaviours of these important cross sections. At least, several theory groups have meanwhile expressed their interest in doing so.

7. List of acronyms

AO – atomic orbital

CODIAN – LabVIEW based program for the control of ECR ion sources

DEC – double electron capture

DI – direct ionization

ECR – electron cyclotron resonance

ECRIS – electron cyclotron resonance ions source

EOBM – extended over barrier method

FC – Faraday cup

KE – kinetic emission

LZ – Landau-Zener

ND – non-dissociative

OBM – over barrier method

PE – potential emission

PTFE – poly tetra fluoro ethylene

QPPG – quadrupole partial pressure gauge

RIMS – recoil-ion momentum spectroscopy

SAMBA – studies on atomic and molecular collisions by beam attenuation

SEC – single electron capture

SIMION – ion and electron optics simulator

SOPHIE – source for production of highly charged ions using ECR

TES – translational energy spectroscopy

TI – transfer ionization

8. Appendix

A. Technical drawings

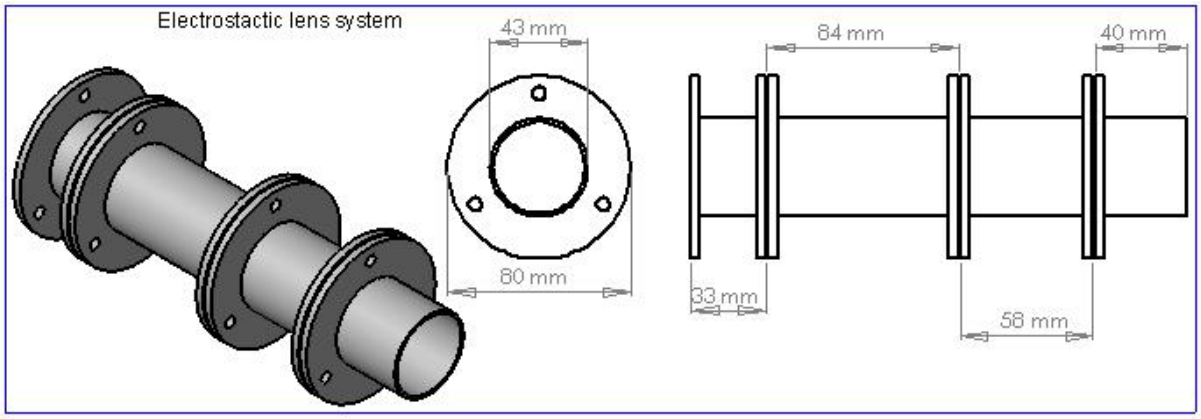

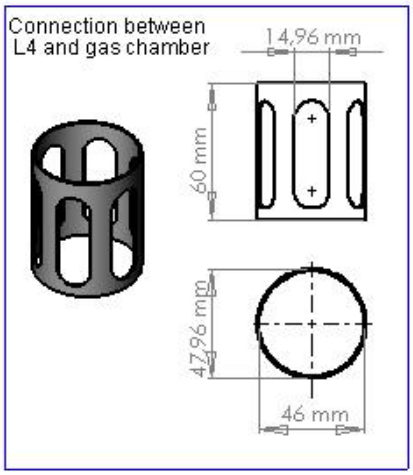

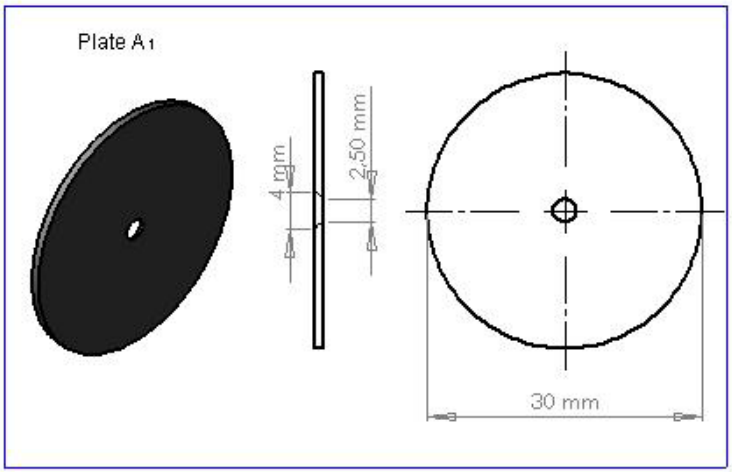

First gas cell flange

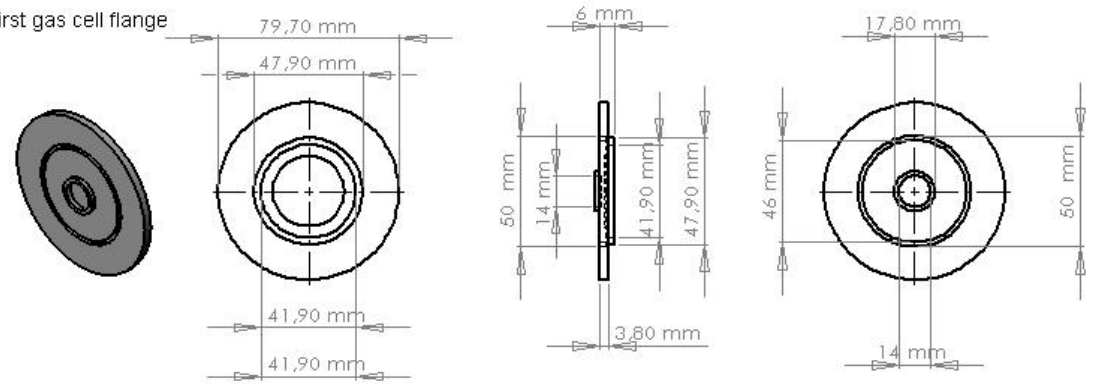

Insulator Teflon ring for FC1

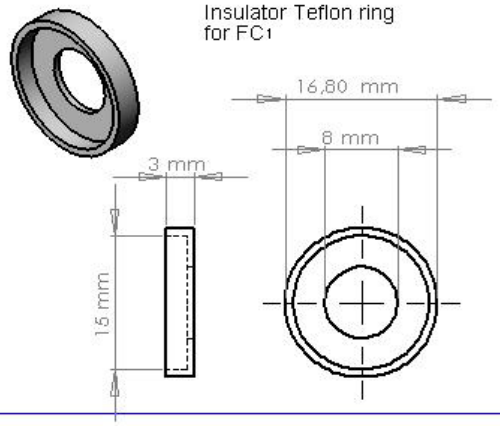

Faraday cup 1 - FC1

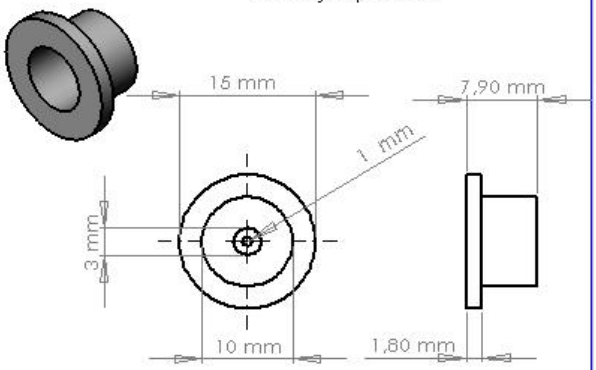

Cylinder for mesh

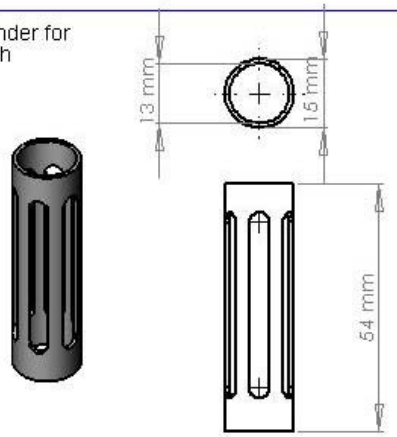

Collector cylinder

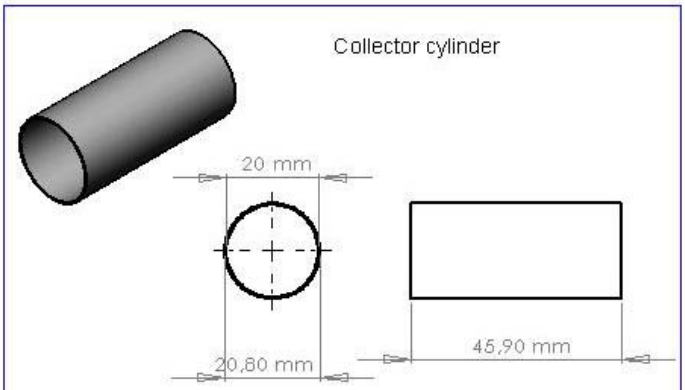

Insulator

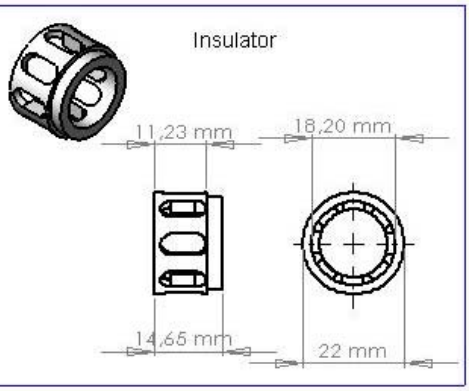

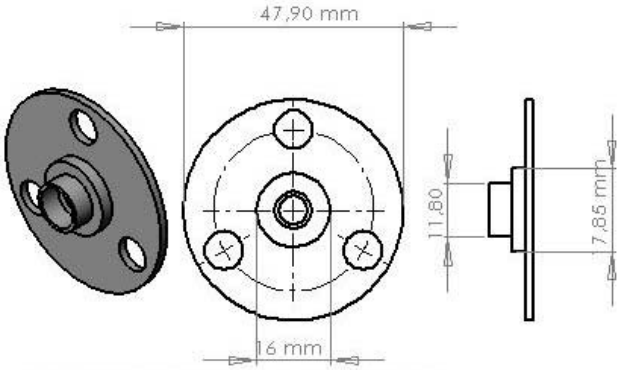

Second flange placed inside the gas chamber

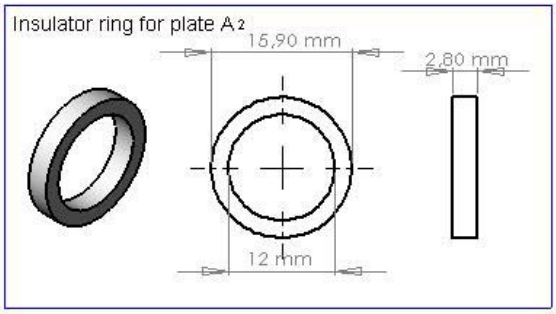
Insulator ring for plate A2
15,90 mm
2,80 mm
12 mm

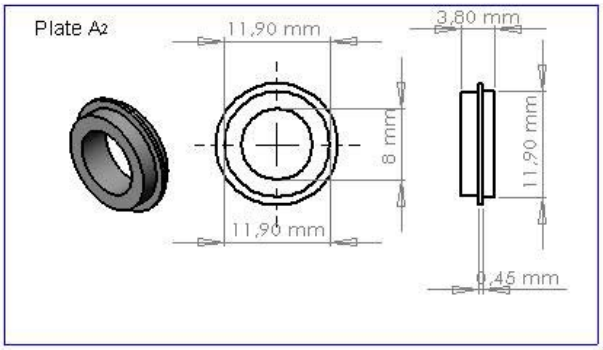
Plate A2
11,90 mm
3,80 mm
8 mm
11,90 mm
11,90 mm
0,45 mm

Faraday cup 2 - FC2
2,50 mm
26,21 mm
4 mm
3,90 mm
47,30 mm
11,90 mm
22 mm
30 mm

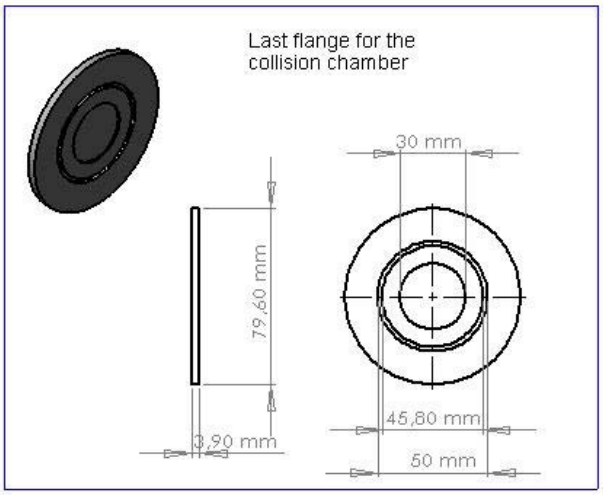
Last flange for the
collision chamber
30 mm
79,60 mm
3,90 mm
45,80 mm
50 mm

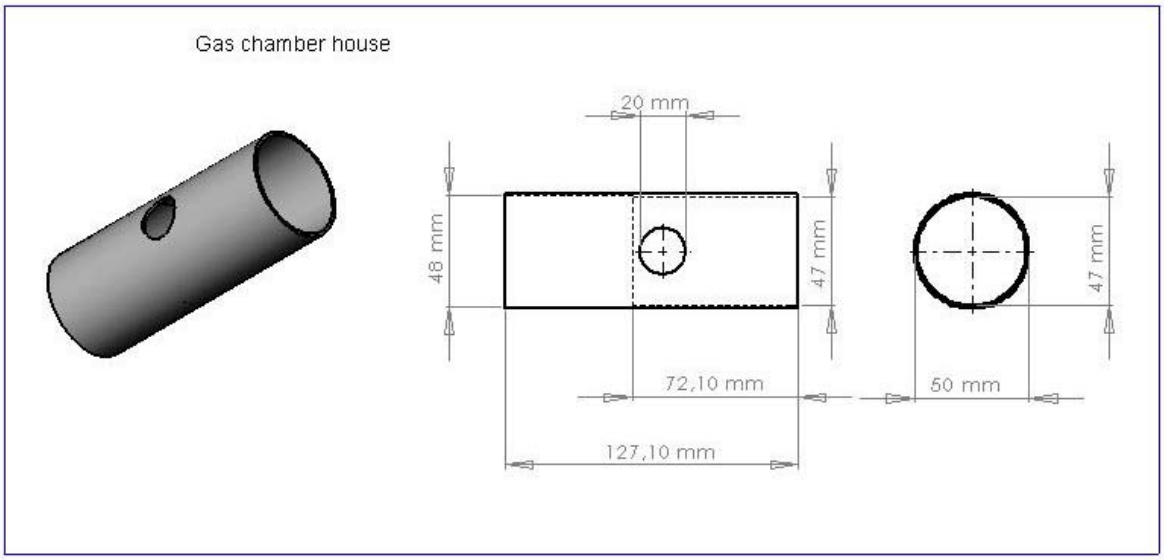
Gas chamber house
20 mm
48 mm
47 mm
47 mm
72,10 mm
50 mm
127,10 mm

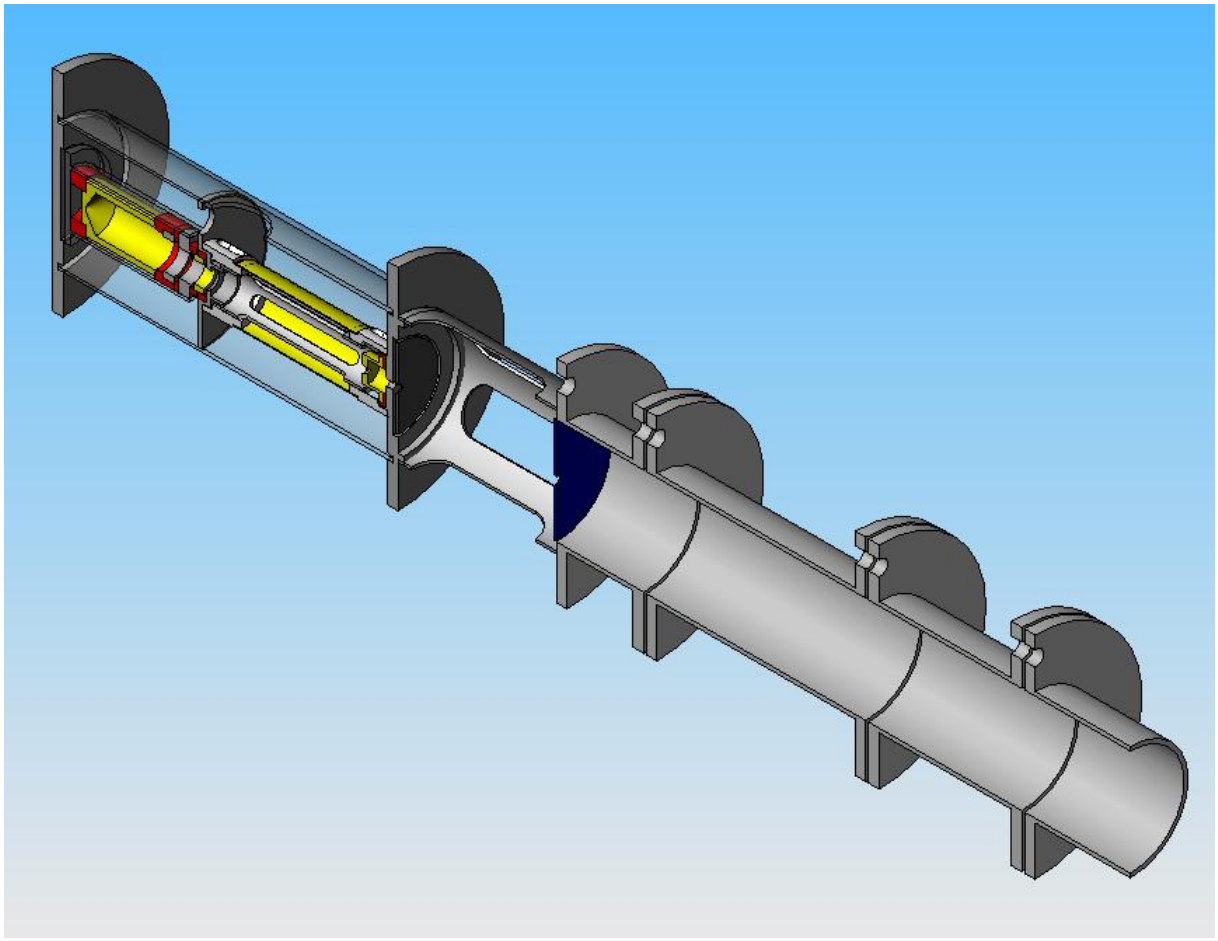

Figure 8.1 – Cross section view of the complete assembled apparatus.

B. Geometry file (SIMION)

The geometry file is a basic code which generates the geometrical potential arrays for SIMION simulation. Here the geometry file developed for the complete system is given, for more information about the code see [62].

```
pa_define(170,170,1300,p,n)                    ;### Scale factor in SIMION 0.33 mm/gu

locate(85,85,250,3) ;  (x,y,z,scale,az,el,rt)
     {
        e(1) ;MESH CILYNDER
                 {
                  fill{
                 within{cylinder(0,0,0,7.5,,54)}
                 notin{cylinder(0,0,0,6.5,,54)}

;CREATION OF THE SLITS
              notin{locate(0,0,-9.5,1)        { box3d(-7.5,-1.5,0,7.5,1.5,-35)}}
                   notin{locate(0,0,-9.5,1,0,60,0) { box3d(-7.5,-1.5,0,7.5,1.5,-35)}}
              notin{locate(0,0,-9.5,1,0,120,0){ box3d(-7.5,-1.5,0,7.5,1.5,-35)}}

;CREATION OF THE CIRCULAR SHAPES IN THE SLITS - BEGINING
              notin{locate(0,0,-9.5,1,90,0,60)  {cylinder(0,0,8,1.1,,16)}}
              notin{locate(0,0,-9.5,1,90,0,120) {cylinder(0,0,8,1.1,,16)}}
              notin{locate(0,0,-9.5,1,90,0,0)   {cylinder(0,0,8,1.1,,16)}}


;CREATION OF THE CIRCULAR SHAPES IN THE SLITS - END
              notin{locate(0,0,-45,1,90,0,0){cylinder(0,0,8,1.1,,16)}}
              notin{locate(0,0,-45,1,90,0,60){cylinder(0,0,8,1.1,,16)}}
              notin{locate(0,0,-45,1,90,0,120){cylinder(0,0,8,1.1,,16)}}
                    }
fill{;coiled wire
                   within{cylinder(0,0,0,7,,0.1)}
                   notin {cylinder(0,0,0,6.9,,0.1)}
                   within{cylinder(0,0,-2,7,,0.1)}
                   notin {cylinder(0,0,-2,6.9,,0.1)}
                   within{cylinder(0,0,-4,7,,0.1)}
                   notin {cylinder(0,0,-4,6.9,,0.1)}
                   within{cylinder(0,0,-6,7,,0.1)}
                   notin {cylinder(0,0,-6,6.9,,0.1)}
                   within{cylinder(0,0,-8,7,,0.1)}
                   notin {cylinder(0,0,-8,6.9,,0.1)}
                   within{cylinder(0,0,-10,7,,0.1)}
                   notin {cylinder(0,0,-10,6.9,,0.1)}
```

```
                within{cylinder(0,0,-12,7,,0.1)}
                notin {cylinder(0,0,-12,6.9,,0.1)}
                within{cylinder(0,0,-14,7,,0.1)}
                notin {cylinder(0,0,-14,6.9,,0.1)}
                within{cylinder(0,0,-16,7,,0.1)}
                notin {cylinder(0,0,-16,6.9,,0.1)}
                within{cylinder(0,0,-18,7,,0.1)}
                notin {cylinder(0,0,-18,6.9,,0.1)}
                within{cylinder(0,0,-20,7,,0.1)}
                notin {cylinder(0,0,-20,6.9,,0.1)}
                within{cylinder(0,0,-22,7,,0.1)}
                notin {cylinder(0,0,-22,6.9,,0.1)}
                within{cylinder(0,0,-24,7,,0.1)}
                notin {cylinder(0,0,-24,6.9,,0.1)}
                within{cylinder(0,0,-26,7,,0.1)}
                notin {cylinder(0,0,-26,6.9,,0.1)}
                within{cylinder(0,0,-28,7,,0.1)}
                notin {cylinder(0,0,-28,6.9,,0.1)}
                within{cylinder(0,0,-30,7,,0.1)}
                notin {cylinder(0,0,-30,6.9,,0.1)}
                within{cylinder(0,0,-32,7,,0.1)}
                notin {cylinder(0,0,-32,6.9,,0.1)}
                within{cylinder(0,0,-34,7,,0.1)}
                notin {cylinder(0,0,-34,6.9,,0.1)}
                within{cylinder(0,0,-36,7,,0.1)}
                notin {cylinder(0,0,-36,6.9,,0.1)}
                within{cylinder(0,0,-38,7,,0.1)}
                notin {cylinder(0,0,-38,6.9,,0.1)}
                within{cylinder(0,0,-40,7,,0.1)}
                notin {cylinder(0,0,-40,6.9,,0.1)}
                within{cylinder(0,0,-42,7,,0.1)}
                notin {cylinder(0,0,-42,6.9,,0.1)}
                within{cylinder(0,0,-44,7,,0.1)}
                notin {cylinder(0,0,-44,6.9,,0.1)}
                within{cylinder(0,0,-46,7,,0.1)}
                notin {cylinder(0,0,-46,6.9,,0.1)}
              }
               }
 e(2) ; Collector
     {
               fill{
          within{cylinder(0,0,-4,11,,46)}
          notin{cylinder(0,0,-4,10,,46)}
           }
   }

e(3) ; FC1
     {
               fill{
          within{cylinder(0,0,4,5,,8)}
          notin{ cylinder(0,0,4,4,,6)}
```

```
                notin{ cylinder(0,0,4,0.5,,8)}
            }
    }

      e(4) ; ALL HOUSE!!
      {
            fill{; first house aperture
          within{cylinder(0,0,6,25,,2)}
          notin{cylinder(0,0,6,1,,2)}
          ;second aperture
          within{cylinder(0,0,-56,25,,2)}
          notin{cylinder(0,0,-56,5,,2)}

          ;GUARD RINGS OF SECOND APERTURE
          within{cylinder(0,0,-51,6,,5)}
          notin{cylinder(0,0,-51,5,,5)}
          ;Ring between stop and suppressor
          within{cylinder(0,0,-61,6,,2)}
          notin{ cylinder(0,0,-61,5,,2)}
           }
    }

e(5) ; RFR - Retarding field ring (A2)
      {
            fill{
          within{cylinder(0,0,-58,6,,2)}
          notin{cylinder(0,0,-58,5,,2)} ;original
           }
    }

e(6) ; SUPPRESSOR
      {
            fill{
          within{cylinder(0,0,-63,6,,2)}
          notin{ cylinder(0,0,-63,5,,2)}
           }
    }

e(7) ; FARADAY CUP
      {
            fill{
          within{cylinder(0,0,-66,6.5,,15)}
          notin{ cylinder(0,0,-66,5.5,,14)}
           }
    }

e(8) ; Plate A1
      {
            fill{; first plate aperture
          within{cylinder(0,0,7,7.5,,0.5)}
          notin{cylinder(0,0,7,1,,0.5)}
```

```
            }
    }

;LENS SYSTEM!!!!

      e(9) ; Cylinder between L4 and Gas Cell
      {
            fill{; first house aperture
          within{cylinder(0,0,66,15,,60)}
          notin{cylinder(0,0,66,14,,60)}
           }
    }

      e(10) ; L4
      {
            fill{
          within{cylinder(0,0,68,15,,2)}
          notin{cylinder(0,0,68,1.5,,2)}
          within{cylinder(0,0,108,15,,40)}
          notin{cylinder(0,0,108,14,,40)}
          within{cylinder(0,0,109,25,,1)}
          notin{cylinder(0,0,109,14,,1)}
           }
    }

      e(11) ; L3
      {
        fill{;
          within{cylinder(0,0,111,25,,1)}
          notin{cylinder(0,0,111,14,,1)}
          within{cylinder(0,0,169,15,,58)}
          notin{cylinder(0,0,169,14,,58)}
          within{cylinder(0,0,170,25,,1)}
          notin{cylinder(0,0,170,14,,1)}
           }
    }

      e(12) ; L2
      {
            fill{;
          within{cylinder(0,0,172,25,,1)}
          notin{cylinder(0,0,172,14,,1)}
          within{cylinder(0,0,255,15,,83)}
          notin{cylinder(0,0,255,14,,83)}
          within{cylinder(0,0,256,25,,1)}
          notin{cylinder(0,0,256,14,,1)}
           }
    }

      e(13) ; L1
      {
```

```
            fill{;
          within{cylinder(0,0,258,25,,1)}
          notin{cylinder(0,0,258,14,,1)}
          within{cylinder(0,0,291,15,,33)}
          notin{cylinder(0,0,291,14,,33)}
          within{cylinder(0,0,292,25,,1)}
          notin{cylinder(0,0,292,14,,1)}
           }
}

  e(14) ; Apperture before L1
  {
            fill{;
          within{cylinder(0,0,320,25,,1)}
          notin{cylinder(0,0,320,1.5,,1)}
           }
}

 };end main locate
```

C. Generated potential array (SIMION)

Here we give the generated geometrical potential arrays using the geometry file given in appendix A as shown in SIMION program.

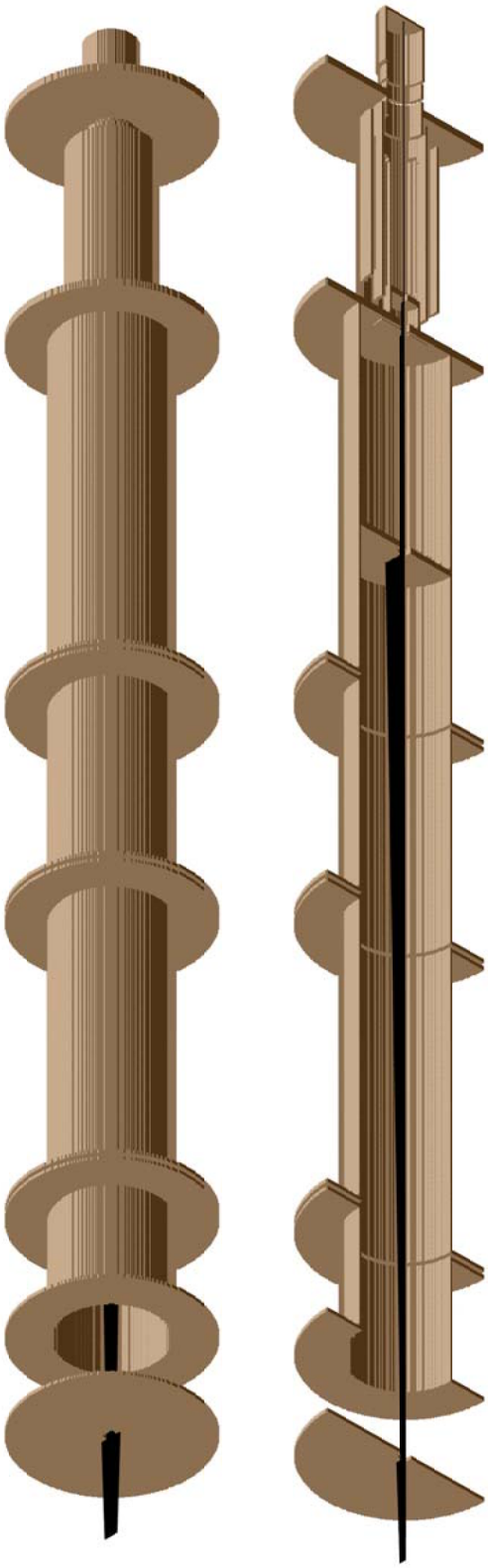

9. Acknowledgments

I would like to dedicate this work to my former supervisor, o.Univ. Prof. Dr. Hannspeter Winter, whose expertise, understanding, and patience, added considerably to my graduate experience. He was the mentor of this investigation but unfortunately it was not given to him to live to see the outcome of this work.

I would like to thanks immensely my actual supervisor, ao.Univ. Prof. Dr. Friedrich Aumayr (Fritz), for his friendship, financial support, advices, suggestions and principally for his close guidance in the final stage of this work. I am very grateful for the opportunities that he has given me to participate in conferences, training courses and summer-schools.

A very special thank-you goes to the workshop team, Ing. Wolfgang Beck, Herbert Schmidt and Rainer Gärtner. In the same manner my thanks go to Ing. Paul Berlinger, who is responsible for all the electronics. It was the skills and hard work of these people, that allowed the experimental setup presented in this thesis to become reality.

A major contribution to the improvement of the charge exchange apparatus came from Gregor Kowaric. I am very grateful for his friendship, for the enjoyable discussions and for the fact, that he brightened up the lab, by bringing Elena there.

I am indebted to Artur Golczewski for developing the C++ codes for the theoretical calculations, for reading this thesis, giving significant suggestions and principally for his constant good mood and friendship. My thanks also go to my office-mate Walter Meissl, for his suggestions, nice discussions and sincere friendship.

I am grateful to Carla and Mario (cumpadi) Barbatti (Max-Planck Institut für Eisenforschung (Düsselfdorf) and Instituted for Quantum Chemistry (Univie), respectively) for the nice discussions and their help with the theoretical part of this work, for correcting my English as well as for their pleasant friendship and for bringing a breeze of the Brazilian atmosphere to the grey landscapes of Vienna.

Of all colleagues, I especially want to thank, Dr. Wolfgang Werner, Dr. Ille Gebeshuber and Mag. Dorian Bridi for the nice atmosphere and encouragement.

My most heartfelt gratitude goes to my wife, Corni, without whose love and encouragement I would not have finished this thesis. As well as to my parents, who, despite the distance, were always supporting and encouraging me throughout this sometimes difficult endeavour.

Finally, I recognize that this research would not have been possible without the financial assistance of the Austrian Academy of Sciences (FWF), the Association EURATOM-OEAW and the management of ÖAD (Österreichischer Austauschdienst).

10. Bibliography

[1] R. Hoekstra, D. Bodewits, S. Knoop, R. Morgenstern, L. Mendez, L. F. Errea, C. Illecas, A. Macias, B. Pons, A. Riera, F. Aumayr, and HP. Winter, Atomic and Plasma-Material Interaction Data for Fusion **In press**(2006).

[2] V. Izmodenov, Y. Malama, G. Gloeckler, and J. Geiss, Astronomy & Astrophysics **414** L29 (2004).

[3] D. Bodewits, R. Hoekstra, B. Seredyuk, R. W. McCullough, G. H. Jones, and A. G. G. M. Tielens, The Astrophysical Journal **642** 593 (2006).

[4] L. Guillemot, P. Roncin, M. N. Gaboriaud, H. Laurent, and M. Barat, J. Phys. B: At. Mol. Phys **23** 4293 (1990).

[5] R. A. Mapleton, Theory of Charge Exchange, New York, 1972.

[6] J. P. M. Beijers, R. Hoekstra, and R. Morgenstern, J. Phys. B: At. Mol. Phys **29** 1397 (1996).

[7] S. E. Butler and A. Dalgarno, J. Astrophys. **241** 838 (1980).

[8] D. L. Cooper, P. C. Stancil, A. R. Turner, J. G. Wang, N. J. Clarke, and B. Zygelman, Int. J. Mol. Sci. **3** 220 (2002).

[9] R. Hoekstra, H. O. Folkerst, J. P. M. Beijers, R. Morgenstern, and F. J. de Heer, J. Phys. B **27** 2021 (1994).

[10] E. Wolfrum, F. Aumayr, D. Wutte, HP. Winter, E. Hintz, D. Rusbuldt, and R. P. Schorn, Review of Scientific Instruments **64** 2285 (1993).

[11] K. D. Zastrow, M. O'Mullane, M. Brix, C. Giroud, A. G. Meigs, M. Proschek, and H. P. Summers, Plasma Physics and Controlled Fusion **45** 1747 (2003).

[12] I. O. Bespamyatnov, W. L. Rowan, R. S. Granetz, and D. F. Beals, Review of Scientific Instruments **77**(2006).

[13] H. D. Falter, M. Proschek, S. Menhart, F. Aumayr, HP. Winter, D. Ciric, A. Dines, D. Godden, and T. T. C. Jones, Fusion Engineering and Design **56-7** 941 (2001).

[14] H. D. Falter, M. Proschek, S. Menhart, F. Aumayr, HP. Winter, D. Ciric, S. Cox, A. Dines, D. Godden, N. Hawkes, and T. T. C. Jones, Review of Scientific Instruments **71** 3723 (2000).

[15] B. C. Stratton, D. Long, R. Palladino, and N. C. Hawkes, Review of Scientific Instruments **70** 898 (1999).

[16] L. Q. Hu, B. N. Wan, C. D. Hu, B. H. Liu, Z. W. Wu, J. Huang, W. L. Rowan, H. Huang, K. Gentle, and H.-D. Team, Review of Scientific Instruments **75** 3496 (2004).

[17] S. Brezinsek, A. Huber, S. Jachmich, A. Pospieszczyk, B. Schweer, and G. Sergienko, Fusion Science and Technology **47** 209 (2005).

[18] L. Carraro, M. E. Puiatti, F. Sattin, P. Scarin, and M. Valisa, Review of Scientific Instruments **70** 861 (1999).

[19] H. P. Summers, H. Anderson, M. G. O'Mullane, and M. G. von Hellermann, Physica Scripta **T92** 80 (2001).
[20] M. v. Hellermann, Plasma Physics and Controlled Fusion **35** 799 (1993).
[21] EURATOM-UKAEA, www.fusion.org.uk
[22] C. M. Lisse, K. Dennerl, J. Englhauser, M. Harden, F. E. Marshall, M. J. Mumma, R. Petre, J. P. Pye, M. J. Ricketts, J. Schmitt, J. Trumper, and R. G.West, Science **274** 205 (1996).
[23] T. E. Cravens, Geophys. Res. Lett. **24** 105 (1997).
[24] P. Beiersdorfer, C. M. Lisse, R. E. Olson, G. V. Brown, and H. Chen, ApJ. **549** L147 (2001).
[25] D. Bodewits, Z. Juhasz, R. Hoekstra, and A. G. G. M. Tielens, ApJ. **606** L81 (2004).
[26] Y. S. Park, H. Cho, L. Parenteau, A. D. Bass, and L. Sanche, Journal of Chemical Physics **125**(2006).
[27] Y. V. Vasil'ev, B. J. Figard, V. G. Voinov, D. F. Barofsky, and M. L. Deinzer, Journal of the American Chemical Society **128** 5506 (2006).
[28] A. G. Carles and A. G. Malonda, International Journal of Radiation Biology **82** 211 (2006).
[29] S. Tonzani and C. H. Greene, Journal of Chemical Physics **124**(2006).
[30] M. C. Bacchus-Montabonel, M. Labuda, Y. S. Tergiman, and J. E. Sienkiewicz, Physical Review A **72**(2005).
[31] S. G. Ray, S. S. Daube, and R. Naaman, Proceedings of the National Academy of Sciences of the United States of America **102** 15 (2005).
[32] J. W. Turkstra, R. Hoekstra, S. Knoop, D. Meyer, R. Morgenstern, and R. E. Olson, Phys. Rev. Lett. **87** 123202 (2001).
[33] W. J. Hehre, L. Radom, P. v. Schleyer, and J. A. Pople, Ab Initio Molecular Orbital Theory, Wiley, Chichester, 1986.
[34] D. Hirst, A Computational Approach to Chemistry, Blackwell, Oxford, 1990.
[35] F. Jensen, Introduction to Computational Chemistry, Wiley, Chichester, 1999.
[36] R. C. Isler and E. C. Crume, Phys. Rev. Lett. **41** 1296 (1078).
[37] E. Teller, Phys. Rev. A **41** 109 (1937).
[38] J. Tharamel, V. A. Kharchenko, and A. Dalgarno, Phys. Rev. A **50** 1 (1994).
[39] D. R. Bates, Proc. Phys. Soc., Lond. **257** 22 (1960).
[40] L. D. Landau, Phys. Z. Sow. **1** 46 (1932).
[41] C. Zener, Proc. R. Soc. **137** 696 (1932).
[42] J. C. Tully and R. K. Preston, J. Chem. Phys. **43** 3259 (1971).
[43] B. Zygelman, D. L. Cooper, M. Ford, A. Dalgarno, J. Gerratt, and M. Raimondi, Phys. Rev. A. **46** 3846 (1992).
[44] M. T. Stollberg and H.-W. Lee, Phys. Rev. A **29** 2448 (1984).
[45] HP. Winter, Personal communication, TU-WIEN(1977).
[46] R. E. Olson and A. Salop, Phys. Rev. A **14** 579 (1976).
[47] A. Golczewski, C++ Program for Landau-Zener calculations, TU-WIEN, Vienna, 2006.
[48] N. Bohr and J. Lindhard, K. Dan Vidensk. Selsk. Mat. Fys. Medd. **28** 7 (1954).
[49] H. Ryufuku, K. Sasaki, and T. Watanable, Phys. Rev. A **21** 745 (1980).
[50] A. Bárány, G. Astner, H. Cederquist, H. Danared, S. Huldt, P. Hvelplund, A. Johnson, H. Knudsen, L. Liljeby, and K. G. Rensfelt, Nucl. Instr. Meth. B **9** 397 (1985).
[51] A. Niehaus, J. Phys. B: At. Mol. Phys **19** 2925 (1986).
[52] V. Ostrovsky, J. Phys. B **28** 3901 (1995).
[53] F. Sattin, Phys. Rev. A. **62** 042711 (2000).
[54] F. Sattin, Phys. Rev. A. **64** 034704 (2001).

[55] L. Lugosi and L. Sarkadi, Nuclear Instruments and Methods in Physics Research B **205** 591 (2003).
[56] S. Figueira da Silva and A. Golczewski, C++ Program for EOBM calculation, TU-WIEN, Vienna, 2007.
[57] E. Galutschek, Ph.D. Thesis, TU-WIEN(2005).
[58] E. Galutschek, R. Trassl, E. Salzborn, F. Aumayr, and HP. Winter, J. Phys. Conf. Ser. **In press**(2006).
[59] R. Geller, Electron Cyclotron Resonance Ion Sources and ECR Plasmas, Institute of Physics, Bristol, 1996.
[60] National Instruments Corporation, LabVIEW , www.ni.com.
[61] J. Bundesmann, LEIF Report 5, European Network HPRI-CT-1999-40012.
[62] SIMION, 3D version 7.0 software package, www.simion.com
[63] D. Hasselkamp, in Particle Induced Electron Emission II, edited by G. Höhler, Springer, Heidelber, 1992.
[64] C. Lemell, J. Stöckl, J. Burgdörfer, G. Betz, HP. Winter, and F. Aumayr, Physical Review Letters **81** 1965 (1998).
[65] A. Arnau, F. Aumayr, P. M. Echenique, M. Grether, W. Heiland, J. Limburg, R. Morgenstern, P. Roncin, S. Shipppers, R. Schuch, N. Stolterfoht, P. Vargas, T. J. M. Zouros, and HP. Winter, Surface Science Reports **27** 113 (1997).
[66] F. Aumayr and HP. Winter, Chapter 3 in Springer Tracks in Modern Physics **225** 79 (2007).
[67] H. Eder, M. Vana, F. Aumayr, and HP. Winter, Rev. Sci. Instrum. **68** 165 (1996).
[68] HP. Winter and F. Aumayr, J. Phys. B **32** R39 (1999).
[69] NIST, Atomic Spectra Database Levels, http://physics.nist.gov
[70] K. P. Huber and G. Herzberg, Molecular spectra and molecular structure, IV. Constants of diatomic molecules, New York, 1979.
[71] N. Shimakura, M. Kimura, and N. F. Lane, Physical Review A **47** 709 (1993).
[72] L. M. Kishinevsky, Radiation Effects **19** 23 (1973).
[73] F. B. M. Copeland and D. S. F. Crothers, Atomic Data and Nuclear Tables **65** 273 (1997).
[74] S. Sakabe and Y. Izawa, Atomic Data and Nuclear Data Tables **49** 257 (1991).
[75] C. Hayden and C. Amme, J. Chem. Phys. **42** 2011 (1965).
[76] J. A. Dillon, J. Chem. Phys. **23** 775 (1955).
[77] F. A. Hinds and R. Novick, J. Phys. B: At. Mol. Phys **11** 2201 (1978).
[78] J. B. Hasted, Physics of Atomic Collisions, Butterworths, London, 1972.
[79] E. W. McDaniel, Collision Phenomena in Ionized Gases, Wiley, 1964.
[80] C. L. Cocke, R. Dubois, T. J. Gray, E. Justiniano, and C. Can, Physical Review Letters **46** 1671 (1981).
[81] B. A. Huber, J. Phys. B: At. Mol. Phys **13** 809 (1980).
[82] J. Puerta and B. A. Huber, J. Phys. B: At. Mol. Phys **18** 4445 (1985).
[83] K. Okuno, Journal of the Physical Society of Japan **55** 1504 (1986).
[84] P. C. Cosby, R. A. Bennett, J. R. Peterson, and J. T. Moseley, J. Chem. Phys. **63** 809 (1975).
[85] Y. Kaneko, T. Iwai, S. Ohtani, K. Okuno, N. Kobayashi, S. Tsurubuchi, M. Kimura, and H. Tawara, J. Phys. B: At. Mol. Phys **14** 881 (1981).
[86] Z. Z. Latypov, N. V. Fedorenko, I. P. Flaks, and A. A. Shaporenko, Zh. Eksp. Teor. Fiz **55** 847 (1968).
[87] I. P. Flaks and E. S. Soloviev, Zh. Tekh. Fiz. **28** 599 (1958).
[88] G. R. Hertel and W. S. Koski, J. Chem. Phys. **40** 3450 (1966).
[89] E. Bolemen, H. Winter, F. J. D. Heer, R. Fortner, and A. Salop, J. Phys. B. **11** 24 (1978).

[90] V. V. Afrosimov, A. A. Basalaev, G. A. Leiko, and M. N. Panov, Zh. Eksp. Teor. Fiz **74** 1605 (1978).
[91] J. E. Bayfield and G. A. Khayrallah, Phys. Rev. A **11** 920 (1975).
[92] K. H. Berkner, R. V. Pyle, J. W. Stearns, and J. C. Warren, Phys. Rev. **166** 44 (1968).
[93] C. Harel and A. Salin, J. Phys. B: At. Mol. Phys **13** 785 (1980).
[94] M. Kimura, J. Phys. B: At. Mol. Phys **21** L19 (1988).
[95] W. Fritsch, J. Phys. B: At. Mol. Phys **27** 3461 (1994).
[96] Y. H. Chen, R. E. Johnson, R. R. Humphries, M. W. Siegel, and J. W. Boring, J. Phys. B: At. Mol. Phys **8** 1527 (1975).
[97] J. S. Cohen and J. N. Bardsley, Phys. Rev. A **18** 3 (1978).
[98] H. Sato and S. Hara, J. Phys. B: At. Mol. Phys **13** 4577 (1980).
[99] I.A.E.A, Databases on Atomic and Molecular Data for Fusion, www-amdis.iaea.org/aladdin/collision.html
[100] M. Albu, F. Aumayr, and HP. Winter, International Journal of Mass Spectrometry **233** 239 (2004).
[101] W. T. Rogers, J. W. Boring, and R. E. Johnson, J. Phys. B: At. Mol. Phys **11** 2319 (1978).
[102] H. Hanaki, T. Kusakabe, N. Nagai, and M. Sakisaka, Journal of the Physical Society of Japan **52** 424 (1982).
[103] E. Mercier, G. Chambaud, and B. lévy, J. Phys. B: At. Mol. Phys **18** 3591 (1985).
[104] M. E. Rudd, T. V. Goffe, and A. Itoh, Physical Review A **32** 2128 (1985).
[105] R. D. DuBois, Physical Review A **34** 2738 (1986).
[106] R. A. Baragiola and I. B. Nemirovsky, Nucl. Instrum. Methods **110** 511 (1973).
[107] S. Figueira da Silva, G. Kowarik, F. Aumayr, and HP. Winter, J. Phys. Conf. Ser. **In press**(2006).
[108] A. Ichimura and T. Ohyama-Yamaguchi, Physica Scripta **T80** 190 (1999).
[109] K. Ishii, K. Okuno, and N. Kobayashi, Physica Scripta **T80** 176 (1999).
[110] K. Okuno, T. Kaneyasu, K. Ishii, M. Yoshino, and N. Kobayashi, Physica Scripta **T80** 173 (1999).
[111] T. Kusakabe, Y. Miyamoto, M. Kimura, and H. Tawara, Physical Review A **73** 022706 (2006).
[112] E. Y. Kamber, O. Abu-Haija, and S. M. Ferguson, physical Review A **65** 062717 (2002).
[113] S. J. Martin, J. Stevens, and E. Pollack, Phys. Rev. A **43** 3503 (1991).
[114] R. W. McCullough, T. K. McLaughlin, T. Koizumi, and H. B. Gilbody, J. Phys. B: At. Mol. Phys **25** L193 (1992).
[115] W. R. Thompson, M. B. Shah, and H. B. Gilbody, Physica Scripta **T73** 214 (1997).
[116] M. B. Shah and H. B. Gilbody, J. Phys. B: At. Mol. Phys **11** 121 (1978).
[117] J. M. Hodgkinson, T. K. McLaughlin, R. W. McCullough, J. Geddes, and H. B. Gilbody, J. Phys. B **28** L393 (1995).
[118] T. Kusakabe, Y. Yoneda, Y. Mizumot, and K. Katsurayama, Phys. Soc. Jpn. **59** 1218 (1990).
[119] W. L. Nutt, R. W. McCullough, K. Brady, M. B. Shah, and H. B. Gilbody, J. Phys. B: At. Mol. Phys **36** L135 (1978).
[120] K. Okuno, K. Soejima, and Y. Kaneko, J. Phys. B: At. Mol. Phys **25** L105 (1992).
[121] L. F. Errea, A. Macías, L. Méndez, B. Pons, and J. Riera, J. Phys. B: At. Mol. Phys **36** L135 (2003).
[122] B. C. Saha, N. F. Lane, and M. Kimura, Physical Review A **44** R1 (1991).
[123] R. Shingal and C. D. Lin, Physical Review B **40** 1302 (1989).
[124] V. V. Afrosimov, G. A. Leiko, and M. N. Panov, Sov. Phys. Tech. Phys. **25** 313 (1980).

Lebenslauf

14 July 1977	Geboren in Brasilia, Brasilien Vater: Deusdete Gomes da Silva Mutter: Marlene Figueira
1983 – 1991	Ensino Basico 1° Grau (Volksschule) – CE 05 Gama-DF, Brasilia, Brasilien
1991 – 1994	2° Grau (Akademisches Gymnasium) – CED 03 Gama-DF, Brasilia, Brasilien
1995 – 2000	BSc in Physics Universität Brasília – UnB. Institut für Physik, Brasília, Brazil
2000 – 2003	MSc in Physics Universität Brasília – UnB. Institut für Physik, Brasília, Brazil Study of the Distribution Function of Electron in the Loss Cone in a Plasma Confinement by Magnetic Mirrors Machine (auf Portugiesich) betreut von Dr. José Leonardo Ferreira
2004 – 2007	Arbeit als wissenschaftlicher Mitarbeiter und Dissertation „ Charge-exchange processes in collisions of slow ions with atoms and molecules “, betreut von ao.Univ.Prof. Dr. F. Aumayr, am Institut für Allgemeine Physik der Technischen Universität Wien.